Physics – Uspekhi **59** (11) 1091 – 1128 (2016)

REVIEWS OF TOPICAL PROBLEMS

PACS numbers: 52.25.Os, 52.35.Mw, 52.35.Ra, 52.50.Qt, 94.20.Tt

100th ANNIVERSARY OF THE BIRTH OF V L GINZBURG

Dynamic properties of ionospheric plasma turbulence driven by high-power high-frequency radiowaves

S M Grach, E N Sergeev, E V Mishin, A V Shindin

DOI: https://doi.org/10.3367/UFNe.2016.07.037868

Contents

Abstract. A review is given of the current state-of-the-art of experimental studies and the theoretical understanding of nonlinear phenomena that occur in the ionospheric F-layer irradiated by high-power high-frequency ground-based transmitters. The main focus is on the dynamic features of high-frequency turbulence (plasma waves) and low-frequency turbulence (density irregularities of various scales) that have been studied in experiments at the Sura and HAARP heating facilities operated in temporal and frequency regimes specially designed with consideration of the characteristic properties of nonlinear processes in the perturbed ionosphere using modern radio receivers and optical instruments. Experimental results are compared with theoretical turbulence models for a magnetized collisional plasma in a high-frequency electromagnetic field, allowing the identification of the processes responsible for the observed features of artificial ionospheric turbulence.

S M Grach, A V Shindin Lobachevsky State University of Nizhny Novgorod, Faculty of Radiophysics
prosp. Gagarina 23, 603950 Nizhny Novgorod, Russian Federation
E-mail: sgrach@rf.unn.ru, shindin@rf.unn.ru
E N Sergeev Lobachevsky State University of Nizhny Novgorod, Radiophysical Research Institute,
ul. B Pecherskaya 25a, 603950 Nizhny Novgorod, Russian Federation
E-mail: esergeev@nirfi.unn.ru
E V Mishin Space Vehicles Directorate, Air Force Research Laboratory, Kirtland AFB, New Mexico 87117, USA

Received 28 June 2016
Uspekhi Fizicheskikh Nauk **186** (11) 1189 – 1228 (2016)
DOI: 10.3367/UFNr.2016.07.037868
Translated by Yu V Morozov; edited by A Radzig

Keywords: ionosphere, pump wave, magnetized plasma, artificial ionospheric turbulence, plasma waves, small-scale irregularities, artificial radio emission of the ionosphere, electron acceleration, artificial optical emission, artificial ionization layers

1. Introduction

In the period from 1945 to 1961, V L Ginzburg headed the Department of Radiowave Propagation at Gorky State University. Simultaneously, he occupied the position of the head of the Theoretical Department (from its foundation in 1956) at the Nizhny Novgorod Radiophysical Research Institute (NIRFI in *Russ. abbr.*). An important area of research conducted by the Nizhny Novgorod branch of Ginzburg's scientific school was the nonlinear interactions of high-power radio waves with near-Earth plasma: ionosphere and magnetosphere.

The impact of high-power radio waves on the near-Earth environment was first described in the 1930s with the discovery of the Luxemburg–Gorky effect, in which a powerful wave, transfers part of its amplitude modulation to a weaker wave as they propagate in the lower ionospheric layers. The physical concepts of the nature of powerful radio wave impact on the ionosphere and its influence on radio wave propagation as of the 1960s–1970s were summarized in the review by V L Ginzburg and A V Gurevich [1], and in the monograph by A V Gurevich and A B Shvartsburg [2].

The onset of systematic investigations into the interaction of high-power short-wave (SW) radio emission with the ionosphere in the USA (Platteville, CO and Arecibo, Puerto

Rico) and the USSR (NIRFI's Yastreb facility, Nizhny Novgorod region) dates to the early 1970s. The NIRFI-based studies were initiated by G G Getmantsev, Ginzburg's disciple and future Director of the Institute. The early history of artificial ionospheric disturbances was described in review [3] and collected works [4].

The very first experiments gave evidence of a number of new effects of importance for understanding the processes of interaction between powerful electromagnetic waves (pump waves, PWs) and the ionospheric plasma, and their influence on the propagation of radio waves; they also opened up prospects for the development of new methods of ionosphere diagnostics, as well as for various applications. Such new phenomena included the initiation of artificial turbulence in the plasma resonance region of the ionosphere [5–8], large-scale stratification of the ionospheric plasma [9, 10], the generation of combinative frequency signals in the superlong (VLF) wavelength range during modulation of ionospheric currents [11], and resonant scattering of radio waves from artificial periodic irregularities arising in a standing pump wave [12]. Some of them had been predicted earlier or investigated under laboratory or space plasma conditions, while others required new theoretical models to be constructed for their interpretation [13–16].

In this context, it is worthwhile to emphasize the great contribution made by representatives, now deceased, of the Moscow and Nizhny Novgorod branches of Ginzburg's scientific school: V Yu Trakhtengerts (NIRFI; Institute of Applied Physics (IAP) of the Russian Academy of Sciences (RAS), Nizhny Novgorod) and V V Vas'kov (Research Institute of Radio, Moscow; N V Pushkov Institute of Terrestrial Magnetism, Ionosphere and Radiowave Propagation (IZMIRAN) of the RAS, Troitsk, Moscow) to basic research on the interactions between high-power radio waves and the ionosphere; L M Erukhimov and N A Mityakov (NIRFI) greatly contributed to experimental studies in this field.

Today, investigations into the interaction between high-power short radio waves and the ionosphere are carried out at specialized installations (heating facilities) located in near polar regions: European Incoherent SCATter scientific association (EISCAT), Tromso, Norway, and High Frequency Active Auroral Research Program (HAARP), Alaska, USA, or in the mid latitudes: Sura, Nizhny Novgorod region, Russia. The low-latitude facility at Arecibo Observatory in Puerto Rico, USA is about to be commissioned after reconstruction. These heating facilities work at operating frequencies from 2.8 to 10 MHz. The maximum effective radiation power of the HAARP facility reached 3600 MW after the 2007 reconstruction. Before that, the EISCAT facility had had the record-breaking power of 1100 MW. The maximum radiation power of the Sura heating facility ranges 150–270 MW depending on frequency.

The present review was designed to report and discuss results of research on the properties of artificial ionospheric turbulence (AIT) in the F-region ionosphere at altitudes of 200–300 km. AIT is excited near the PW reflection point in the plasma resonance region. As is known [17], when a radio wave with an ordinary polarization (O-mode) approaches the reflection point, its frequency $\omega_0 = 2\pi f_0$ is close to the local plasma frequency ω_{pe}. In other words, it is the plasma resonance region where high-frequency (HF) plasma (electrostatic) waves can be excited. In a nonmagnetized plasma, these waves are Langmuir waves with the dispersion relation $\omega = \omega_{pe}(1 + 3k^2 d_e^2)^{1/2}$, where k is the wave number, and d_e is the Debye radius. In a magnetized plasma, including ionospheric plasma, the purely electrostatic Langmuir waves only propagating along the electromagnetic field $\mathbf{B}_0$ co-exist with quasielectrostatic high-frequency waves whose phase front for $\omega/c \ll k \ll d_e^{-1}$ propagates along the resonance cone:

$$\sin^2\theta_{res} = \frac{(\omega_0^2 - \omega_{pe}^2)(\omega_0^2 - \omega_{ce}^2)}{\omega_{pe}^2 \omega_{ce}^2}\,, \quad \theta_{res} = \angle \mathbf{k}\mathbf{B}_0\,. \qquad (1)$$

At smaller k, the quasielectrostatic mode is an extraordinary Z-mode and propagates outside the resonance cone; in the case of larger k, it is necessary to take account of thermal corrections $\propto (kd_e)^2$, and the wave exists inside the cone. For $\omega_0^2 > \omega_{UH}^2 = \omega_{pe}^2 + \omega_{ce}^2$ (ω_{UH} is the upper-hybrid frequency, ω_{ce} is the electron cyclotron frequency), the resonance cone disappears and thermal corrections need to be considered at all θ angles. Strictly at upper-hybrid resonance, where $\omega_0^2 = \omega_{UH}^2$, the angle $\theta_{res} = \pi/2$ and the wave number of the quasielectrostatic mode is $k \approx (\omega_0/cd_e)^{1/2}(\omega_{ce}/\omega_{pe})$ [17].

For the transverse wave propagation, the dispersion equation for plasma (quasielectrostatic) modes has additional solutions — Bernstein waves, the frequencies of which are close to the harmonics of electron cyclotron frequency $\omega \approx s\omega_{ce}$, where $s \geqslant 2$ is the harmonic number, in both short-wave ($k^2 d_e^2 (\omega_{ce}/\omega_{pe})^2 \gg 1$) and long-wave ($k^2 d_e^2 (\omega_{ce}/\omega_{pe})^2 \ll 1$) limits.

When a pump wave exceeds the threshold power, various parametric instabilities (PIs) develop in the plasma, giving rise to weakly decaying HF plasma quasielectrostatic waves (Langmuir, upper-hybrid, Bernstein, Z-mode) and low-frequency disturbances (ion-acoustic and lower-hybrid waves, drift oscillations, irregularities in plasma density extended along $\mathbf{B}_0$ over tens of kilometers with transverse scales of a few centimeters to tens of kilometers). In the ionosphere, PI can be due to both ponderomotive (HF-pressure of the electric field) [18–21] and thermal (Joule heating) [15, 16] nonlinearities. Conditions for the development of ponderomotive instabilities are most favorable near the PW reflection point (see Section 2), and for thermal instabilities in the upper-hybrid PW resonance region (Section 3).

HF plasma waves accelerate electrons up to a few dozen electron-volts, which leads to additional ionization of the ionospheric plasma due to collisions of energetic electrons with neutral particles [24]. Also, such collisions result in the strengthening of optical airglow of the ionosphere [5], sometimes called artificial aurora. Scattering of high-frequency probing radio waves having frequencies close to f_0 into upper-hybrid ones on small-scale irregularities (also called striations) extended along the geomagnetic field $\mathbf{B}_0$ ($l_\perp < \lambda_0 = c/f_0$, λ_0 is the pump wavelength in a vacuum, c is the speed of light, the subscript $\perp$ indicates $\mathbf{B}_0$ direction) causes anomalous absorption of the probing waves [5, 10]: meter and decimeter irregularities maintain aspect angle scattering of high-frequency and very high-frequency radio waves and their propagation outside direct visibility [7, 8, 10, 25, 26].

AIT excitation pushes plasma out of the region where it undergoes heating by plasma waves [27]. Competition between plasma expulsion from the region of its heating and plasma density increase under the effect of additional

ionization is investigated by multifrequency Doppler probing [27–30] and measuring characteristics of the signals from artificial Earth satellites (AESs) that allow the total electron content on the trajectory of their propagation to be determined. Investigations into PW-induced variations of the total electron content at the HAARP and Sura radio facilities began in 2007 [31–34].

A meaningful AIT manifestation consists in the generation of high-frequency stimulated electromagnetic emission (SEE) of the ionosphere revealed in EISCAT experiments by Thidé, Kopka, and Stubbe in 1981 [35]. SEE is apparent as a low-intensity noise component (from -50 to -90 dB) in the spectrum of a PW signal reflected from the ionosphere. The SEE spectrum consists of several components having frequencies above or below f_0 and detuned from the PW frequency, $|\Delta f| = |f - f_0|$, by a few kHz to ~ 200 kHz. The SEE spectrum, the intensity of artificial irregularities, and optical airglow strongly depend on the ratio of PW frequency f_0 to the electron gyroharmonic frequency sf_{ce} and on the duration of the pumping. Specifically, most SEE spectral components are suppressed as $f_0 \to sf_{ce}$ ($s \geqslant 3$) [36] (under the experimental conditions, f_{ce} varies from 0.9 to 1.45 MHz, depending on the altitude at which the PW interacts with the ionospheric plasma and the geographic location of the heating facility).

PW intensity is of paramount importance for effects of interaction with the ionospheric plasma. Not surprisingly, experiments with superpowerful radio waves resulted in the discovery of phenomena unobservable at a lower power. For example, the use of superpowerful radio waves demonstrated the formation of artificial layers of 'freshly ionized' plasma descending 50–70 km from the PW reflection point [37, 38]. Studies with satellites and UHF incoherent scatter radar using high-power PWs made it possible to detect outgoing ionospheric ions that give rise to density ducts at altitudes of 500–850 km [39–41]. In addition, unusually strong effects induced by X-polarized waves with near-critical frequencies were observed [42–44].

Ionospheric processes proceeding under the influence of a high-power high-frequency radio wave may have very different characteristic times. The authors of Refs [25, 45–47] distinguish four stages in the development of stimulated turbulence. At the initial stage, associated with the development of ponderomotive parametric instability (PPI), plasma waves (PlWs), mostly Langmuir waves, and ion-acoustic disturbances are the first to be excited. After the PW turns on near its reflection point, characteristic time τ_1 of PPI development is 0.1–10 ms in the case of a 'cold' start (in an undisturbed ('unprepared') ionosphere; see Section 2).

With roughly the same characteristic times, PlWs rise following PW switch-on in the presence of pre-formed magnetically oriented small-scale irregularities (striations), the distribution function of PW-accelerated electrons is formed, and PlWs relax (decay) after PW turns-off. The intermediate stage with $\tau_2 \sim 0.1-1$ s also seems to be associated with PPI but at lower altitudes (see Section 2). Thermal parametric effects (thermal parametric and resonant instabilities, TPIs and RIs, respectively), as well as striations and plasma (first of all upper-hybrid) waves, require more time ($\tau_3 \sim 1-10$ s) to manifest themselves in the case of a 'cold' start (see Section 3). Striation relaxation time τ_{rel} varies depending on $l_\perp$, from fractions of a second to tens of seconds [see formulas (21) and (22) in Section 3.2]. The fourth stage (formation of mid-scale irregularities with $l_\perp \sim 0.1-10$ km) lasts even longer, from tens of seconds to minutes, and relaxation of these irregularities may take tens of minutes. [1] Characteristic times of optical airglow generation (radiation lifetimes τ_r of corresponding excited atomic and ion levels) in the ionospheric plasma vary from 10^{-6} to 100 s [48].

Such a relationship between characteristic times τ_1, τ_2, τ_3, and τ_{rel} provided a basis for the development of special diagnostic schedules of the HF pumping of the ionosphere. The idea of using complicated impact regimes for the study of AIT properties was forwarded by L M Erukhimov et al. [49]. The following diagnostic schedules are currently in use:

(1) Impact by pulses of length $\tau_p = 10-500$ ms ($\tau_1 < \tau_2 \lesssim \tau_p < \tau_3$) with a large duty cycle (a small average power). Such a regime allows the properties of Langmuir turbulence to be investigated at the initial (PPI) stage preceding striations' formation, and competition between Langmuir and upper-hybrid (arising at the TPI stage) turbulences to be investigated upon transition to the quasicontinuous regime.

(2) Alternation of long-duration ($\tau_p \gg \tau_3$) quasicontinuous pumping with short pauses ($\tau_B = 20-40$ ms, $\tau_1 \ll \tau_B \ll \tau_3, \tau_{rel}$) and short pulses ($\tau_p = 20-50$ ms, $\tau_1 \ll \tau_p \ll \tau_3$) with large repetition periods ($T_p = 1-3$ s, $\tau_p \ll T_p \lesssim \tau_{rel}$). The quasicontinuous regime makes it possible to follow up SEE development and thereby observe the formation of HF plasma waves (upper-hybrid and Bernstein waves) responsible for SEE generation at the stage of development and in the presence of 'pre-formed' striations, because the striations do not really relax during a short pause τ_B. The short pause can be exploited to study SEE relaxation and, therefore, the dynamics of the HF plasma wave spectrum after PW turn-off, e.g., to measure decrements of their linear decay. The pulsed regime permits striations' relaxation to be studied after PW switch-off and the scale of irregularities responsible for the generation of specific SEE components, to be evaluated, because the mean effective PW power is insufficient to maintain the stationary intensity of striations. Moreover, the behavior of PlW decay decrements at the striation relaxation stage can be investigated in the pulsed regime. A comparison of the measured values with the results of physical models for SEE component generation is used to elucidate (identify) mechanisms behind the formation of HF plasma wave spectra and characteristics of striations' spatial spectra.

(3) Probing the ionosphere with short diagnostic pulses ($\tau_p = 20-200$ μs, $\tau_p \ll \tau_{prop}$) emitted by a heating facility during pauses in PW irradiation, including short pauses interrupting quasicontinuous impacts (τ_{prop} is the PW propagation time up to the reflection point). The wide enough spectrum of probing pulses makes it possible to utilize them as probing waves for multifrequency Doppler probing of the ionosphere with a short step of 1 kHz in a broad frequency range and to explore large-scale plasma density variations (modification of the electron concentration profile) from measurements of reflected signal phases. Measurements of SEE generated by such pulses allow the evaluation of energy transfer over the HF turbulence spectrum and energy spectra themselves in the frequency range directly adjacent to the PW frequency.

(4) HF pumping of the ionosphere at two frequencies, with one part of the transmission antenna of a heating facility emitting PWs responsible for AIT formation in the alternating regime, and the other emitting at a shifted frequency in the

[1] In the physics of the ionosphere, large-scale inhomogeneities are set equal to hundreds of kilometers.

pulsed (diagnostic) regime. Such a schedule allows the altitudinal structure of a perturbed ionospheric region to be elucidated, taking advantage of the fact that radio waves with different frequencies are reflected at different altitudes.

(5) Fast (a few seconds) sweeping of the PW frequency f_0 around electron gyroharmonic frequencies sf_{ce} ($s = 2-7$) in a range of a few dozen kHz. This allows the evaluation of the contribution of various nonlinear processes to the formation of HF turbulence (plasma waves), depending on the f_0-to-multiple of gyroresonance sf_{ce} ratio at constant striation properties and stable ionospheric conditions, and determining with a high degree of accuracy the f_0/sf_{ce} ratio in the region of interaction between the PW and ionospheric plasma.

Successful realization of the above regimes for experimental AIT studies and identification of PW–ionospheric plasma interaction mechanisms in the plasma resonance region require registration of HF radio signals (SEE, probing waves reflected from the ionosphere) in a broad frequency band up to 500 kHz with a high temporal resolution (below 1 ms). This allows, in particular, exploring the SEE spectrum dynamics within the entire range of its existence (> 200 kHz), receiving probing signals and SEE over the entire frequency range during the fast sweeping of PW frequencies, and utilizing individual spectral components of short probing pulses as probing waves for measuring phases and amplitudes of reflected signals. The idea to apply such radio receivers in ionosphere modification experiments was forwarded by Prof. Bo Thidé. The first (rather bulky) receiver for the purpose ('John Silver') designed at the Swedish Institute of Space Physics, Uppsala division, was used in experiments at the Sura and EISCAT facilities in the early 1990s.

Receiving equipment of the second generation (HP3587S work station) was much more efficiently employed in experiments in the late 1990s [50–55]. At present, such equipment, providing a considerably greater capability to carry out experimental studies, is successfully used by many research groups [38, 42, 56–58]. To recall, earlier investigations of AIT dynamic characteristics conducted in the 1980s–1990s included recording radio signals (reflected probing waves and SEE) at fixed frequencies or by spectral analyzers with a rather long registration time of a single spectrum. Either spectral or dynamic AIT characteristics failed to be elucidated by these methods.

Results of experimental and theoretical studies of AIT and its manifestations in the F-region ionosphere at an altitude of 200–300 km obtained before the 90th birthday of V L Ginzburg are summarized in numerous review articles [3, 5, 10, 23, 25, 36, 45–47, 59–67]. Some of these reviews were presented in the form of reports at a Scientific Session of the Physical Sciences Division of the Russian Academy of Sciences [3] and a Joint Meeting of the Editorial Board of the journal *Izvestiya Vuzov. Radiofizika* (*Radiophysics and Quantum Electronics*) and the Scientific Council of the Institute of Applied Physics, RAS [47] dedicated to V L Ginzburg's 90th birthday. Others were published in special issues of the journals *Radio Science* **9** (11)) (1974), **51** (7) (2016); *Izvestiya Vuzov. Radiofizika* **18** (9) (1975), **2**0 (12) (1977), **42** (7, 8) (1999), **48** (7) (2005), **50** (8) (2007); the *Journal of Atmospheric and Terrestrial Physics* **44** (12) (1982) and **47** (12) (1985); the *Journal of Atmospheric and Solar-Terrestrial Physics* **59** (18) (1997) and **60** (12) (1998). Nevertheless, many aspects of AIT physics related in the first place to AIT dynamics, the diagnostic potential of AIT observation, and studies of AIT with limiting powers remain unclear. The considerable progress achieved in the last decade is largely due to enhanced irradiation power (HAARP facility) and the markedly improved diagnostic efficiency of modern radio receivers and optical instruments.

The present review mainly focuses on AIT dynamic characteristics, including those obtained by the authors at a maximum pumping power with the use of the diagnostic setups described in preceding paragraphs, in the first place by SEE measurements. The limited scope of the review does not permit comprehensively highlighting certain aspects of the problem. Suffice it to say that we do not touch investigations of the pumped volume structure using satellites, investigations of mid-scale irregularities, and we only briefly discuss the results of optical airglow studies, the magnetic zenith effect, etc. At the same time, some sections contain a concise analysis of theoretical AIT models and a description of the well-known properties of AIT.

2. Ponderomotive parametric instability: initial and intermediate stages of the pumping

2.1 Theoretical notion

Ponderomotive parametric instability represents the fastest process developing near the point of reflection of high-power radio waves with ordinary polarization within the few first milliseconds after switching on the pump beam. PPI develops as the plasma is pushed out from the regions with an enhanced electric field $\mathbf{E}$ under the action of the ponderomotive (striction) force $\mathbf{F}_p \approx e^2\nabla|E|^2/(4m_e\omega_0^2) \approx \nabla|\mathbf{E}_0\mathbf{E}_1|/(2m_e\omega_0^2)$ [68] arising from the beating of the PW ($\mathbf{E}_0$) and PlW ($\mathbf{E}_1$) fields: $\mathbf{E} = \mathbf{E}_0 + \mathbf{E}_1$).

Fundamentals of the PPI theory for the ionosphere were elaborated in Refs [6, 19–21, 23]. Two kinds of striations can be excited near the PW reflection level h_r, where $\omega_0 \approx \omega_{pe}$ ($\omega_0 = 2\pi f_0$, $\omega_{pe} = 4\pi e^2 N_e/m_e$ is the electron plasma frequency, N_e is the plasma electron number density, e and m_e are the electron charge and mass) in the isothermal ionosphere ($T_e \gtrsim T_i$ where T_e and T_i are the electron and ion temperatures, respectively). Kind 1 involves induced scattering on ions, giving rise to PlWs with frequencies $\omega \leqslant \omega_0$ and low-frequency disturbances like ion-acoustic oscillations with the frequency $\Omega = \omega_0 - \omega$, where $\Omega/2\pi$ is on the order of several kHz. Kind 2 represents (aperiodic) oscillating two-stream instability (OTSI) accompanied by excitation of PlWs having frequency $\omega = \omega_0$. The threshold field and maximum (Ω-dependent) growth rate γ of induced scattering are given at a low suprathreshold level by the expressions

$$E_{th}^2 = \frac{16\pi\nu N_e T_e}{|\mathbf{a}_0\mathbf{a}_1|^2\omega_0 F_m}\,, \quad \gamma = \nu\left(\frac{E_0^2}{E_{th}^2} - 1\right), \tag{2}$$

where $\mathbf{a}_0$, $\mathbf{a}_1$ are the PW and PlW polarization vectors, ν is the linear damping rate of PlW intensity damping, the coefficient $F_m \sim 1$ is determined by the electron-to-ion temperature ratio, and E_0 is the PW electric field strength amplitude. Damping rate ν depends on the frequency ν_e of electron–electron collisions, and on Landau damping on thermal electrons (γ_L) and photoelectrons (γ_{ph}): $\nu = \nu_e + 2\gamma_L + 2\gamma_{ph}$. The OTSI threshold and growth rate are also defined by formula (2) with the substitution of $(1 + T_i/T_e)$ for F_m.

Regular inhomogeneity of ionospheric plasma weakly affects E_{th}, since the criterion $(kL)^{-1} \ll \nu/\omega_0$ ($L = N_e\,(\mathrm{d}N_e/\mathrm{d}z)^{-1}$ is

the characteristic irregularity scale, and z is the distance from the PW reflection point) [18] is satisfied under ionospheric conditions. At the same time, the PW field swelling effect in an inhomogeneous medium, such as the ionosphere, becomes essential: the PPI threshold in terms of PW power is minimum and the growth rate maximum in the first standing wave (Airy function) maxima near the PW reflection point. Because $\omega_0 = \omega_{pe}$ near the ordinary wave reflection point, then for

$$\omega_0^2 - \omega_{pe}^2 \ll \omega_0 \omega_{ce} \sin^2 \frac{\alpha}{2} |\cos \alpha| \quad (\alpha = \angle \mathbf{k}_0 \mathbf{B}_0) \tag{3}$$

the PW is polarized practically along the geomagnetic field ($\mathbf{E}_0 = E_0 \mathbf{a}_0 \parallel \mathbf{B}_0$) [17], and the resonance cone (1) in which the plasma (Langmuir) waves can exist is forced in the magnetic field direction: $|\theta| < |\theta_{res}|$ [see formula (1)]; here, one-dimensional turbulence is excited: PlW and ion-acoustic perturbation wave vectors are parallel to the magnetic field $\mathbf{B}_0$. In this case, the induced scattering growth rate is greatest at

$$\Omega_m = \beta_m k_m V_{T_i}, \; k_m \approx \left[\frac{2(\omega_0^2 - \omega_{pe}^2)}{3V_{T_e}^2} \right]^{1/2} \approx \frac{(z/3L_0)^{1/2}}{d_e}. \tag{4}$$

Here, $V_{T_{e,i}} = (T_{e,i}/m_{e,i})^{1/2}$ are the thermal velocities of electrons and ions, $z = h_r - h$ is the distance from the PW refection point, $d_e = V_{T_e}/\omega_{pe}$ is the Debye length, and coefficient $\beta_m \sim 1$ depends on the ratio T_e/T_i. The growth of PlWs with $\omega = \omega_0 - \Omega$ results in their cascade transfer down the spectrum in terms of frequency (and in k magnitude) and the appearance of narrow ($\delta\omega/\Omega \ll 1$) spectral peaks (satellites) [20–22, 69, 70] spaced at frequencies by $\approx 2\Omega_m$. Transfer from the sth satellite to the $(s+1)$th one results in a $\Delta k \sim (m_e/m_i)^{1/2} d_e^{-1}$ decrease in the wave number, with $\mathbf{k}_s \uparrow\downarrow \mathbf{k}_{s+1}$.

In the case of a high-power PW, the region of PPI excitation extends down from the PW reflection point to altitudes h_L, where the Landau damping of Langmuir waves on thermal electrons ($\gamma_L \gg \nu_e$) becomes significant, and the instability threshold sharply increases. For lower altitudes $h_L < h < h_r$, where $\omega_0 > \omega_{pe}$, the resonance cone (1) 'opens'. Moreover, the PPI excitation conditions are strongly influenced by the tilting of a magnetic field about the vertical in the ionosphere. For example, at Arecibo, when the PW is vertically incident on the ionosphere, the angle $\alpha_I \approx 47°$ (α_I is the angle between the vertical and magnetic field direction). In this case, inequality (3) is satisfied practically in the entire plasma resonance region ($h > h_L$) and $\mathbf{E}_0 \parallel \mathbf{B}$. At the Boulder ($\alpha_I \approx 22°$), Sura ($\alpha_I \approx 18.5°$), HAARP ($\alpha_I \approx 14°$), and EISCAT ($\alpha_I \approx 12°$) heating facilities, a descent from the reflection point is associated with the fulfillment of the reverse inequality with respect to Eqn (3), while PW polarization becomes almost circular with $\mathbf{E}_0 \perp \mathbf{B}_0$.[2] As a result, excitation of plasma waves with a broad angular spectrum up to $\theta = \pi/2$ becomes possible in the PPI process.

A decrease of PW intensity as it penetrates into the depths of the plasma due to the absorption of energy by plasma waves during the induced scattering is much slower in terms of the height than the increase in intensity due to field swelling [22]. Thus, plasma turbulence during PPI development occupies the entire volume where the instability threshold is exceeded after the PW switch-on. The largest PW energy loss must occur near the reflection point in the first standing wave (Airy function) maxima.

If the PW power is high enough, the PlW energy density W_s in the sth satellite during energy transfer into the small k region can exceed the threshold of modulation instability: $W_s/N_e T_e > 3k^2 d_e^2$ that leads to the trapping of PlWs in small-scale structures — cavitons, to the transfer PlWs over the spectrum into the large k region and to Langmuir collapse (strong Langmuir turbulence). Cavitons in a magnetic field are elongated in the transverse direction [75]. Their characteristic longitudinal size (along $\mathbf{B}_0$) in the ionosphere must be 1–10 m [76]. According to Ref. [75], the symmetric shape of the cavern is restored during collapse, and the magnetic field stops influencing the collapse for $\delta N_e > \omega_{ce}^2/\omega_{pe}^2$ (δN_e is the relative plasma density disturbance in the cavern).

Such an PPI development scenario has been examined by many authors, both in the weak turbulence approximation (WTA), when the linear dispersion equation for plasma waves holds and nonlinearity is only responsible for their interaction [77], and in the strong turbulence approximation (STA) when nonlinearity markedly changes the waves' dispersion properties [75, 78]. Consideration in the STA is given in the framework of Zakharov's model [78] making use of the equation for the slowly changing amplitude of electrostatic waves in the presence of the pump field and density perturbations, and the equation for density perturbations (ion-acoustic waves).

A large number of articles on the theory and numerical simulation of Langmuir turbulence in the framework of the STA in application to ionospheric experiments (see, for instance, paper [67] and references cited therein) have been published since the 1990s. Specifically, the scope of WTA applicability was determined [79, 80], the isothermal plasma theory elaborated [81], nonunidimensionality of PlW spectra and spatial nonuniformity of the medium taken into account, and magnetic field effects more adequately considered [82]. In addition, PlW spectra and the spectra of electromagnetic radiation from the SEE Langmuir turbulence generation region were calculated [83, 84], a scheme of full-scale modeling of strong turbulence was developed taking account of the marked difference between characteristic temporal and spatial parameters of electromagnetic and plasma waves and low-frequency perturbations [73, 84], and WTA conclusion about maximum PW energy losses near the reflection point was confirmed. The most detailed comparison of experimental findings with results of numerical simulation in the framework of the STA can be found in Refs [67, 74]. True, some experimental data cannot yet be interpreted in the framework of the STA.

2.2 Experimental results

In experiment, PPI manifests itself as the ponderomotive self-action (PSA) effect of a pump wave (a rapid, in several millisecond, decrease in the PW reflected signal amplitude due to the extraction of energy by plasma waves) and the generation of electromagnetic waves, i.e., the narrow continuum (NC) component of SEE, with the main portion of energy in the region of negative frequency shifts from $f_0 - 40$ kHz $\lesssim \Delta f = f_{SEE} - f_0 < 0$ [52, 85–87]. The appearance of intense Langmuir waves near the high-power radio wave reflection level is also detected by incoherent scattering

[2] The O-wave polarization in the vicinity of the reflection point was calculated more rigorously under the conditions of ionospheric modification experiments in Refs [71–74].

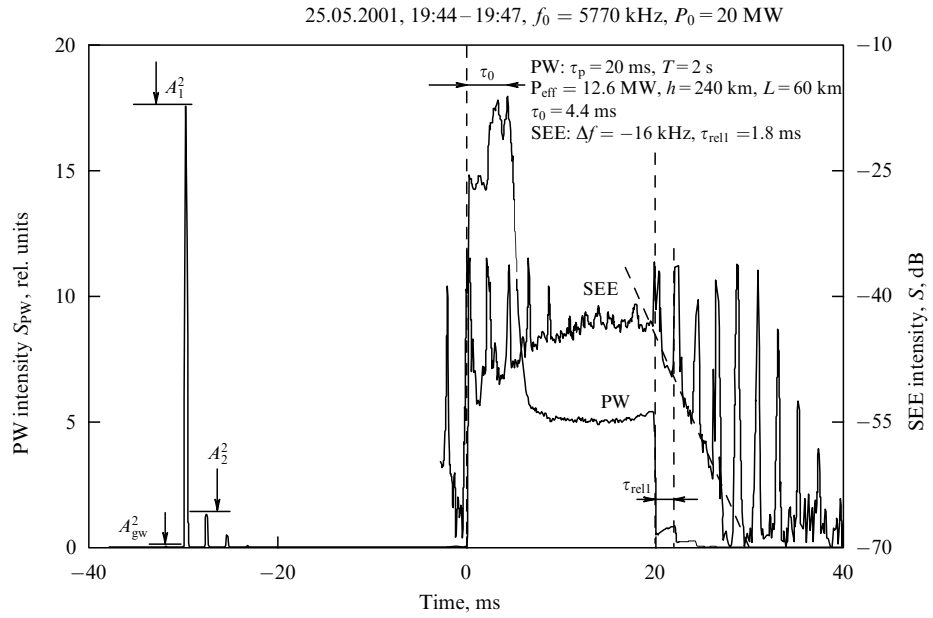

Figure 1. Oscillograms of PW and SEE signals for the shift $\Delta f = -16$ kHz after averaging over 100 PW pulses with duration τ_p and repetition period T. Here: A_{gw} — ground wave amplitude; L — characteristic spatial scale of the F-layer, $P_{eff} = P_0 \exp(-\Gamma)$, where P_0 — emitted power, Γ — linear absorption determined from the ratio of first-to-second reflections, A_1 and A_2. Sura radio facility, Msc, summertime (UTC + 4 h) [88].

radars. This section does not contain figures illustrating results of radar experiments; the interested reader is referred to reviews [3, 64, 67].

It is most convenient to study PPI and the transition to further stages of AIT development by irradiating the ionosphere with sufficiently short (100–500 ms) pulses with a large duty cycle (a low mean power) [see Introduction, schedule (1)]. An example of the PSA effect, oscillograms of SEE at $\Delta f = -16$ Hz and short diagnostic pulses used to measure regular (linear) absorption at a low effective emitted PW power $P_0 = 20$ MW are presented in Fig. 1.

Periodic sharp peaks in Fig. 1 and the figures that follow result from the response of receiving equipment to the edges of the PW signal multiply reflected from the ionosphere. Reducing P_0 in the course of experiment till the PSA disappears and calculating the PW electric field in the first maximum of the standing wave with regard for linear absorption and the real electron concentration profile make it possible to determine the threshold PPI field E_{th}. Then, the SEE relaxation time τ_{rel1} after PW switch-off (Fig. 1) can be invoked to determine PlW damping rate ν, assuming $\nu = \tau_{rel1}^{-1}$.

Measurements made in Ref. [88] under various ionospheric conditions show that the threshold field of the PSA effect varies between 250 and 750 mV m^{-1}; after the PW turns off, SEE relaxes with characteristic damping rates $\nu \sim 400$–2200 s^{-1}. The dependence of E_{th} on f_0 and ν practically coincides with theoretical one following from formula (2): $E_{th} \sim (f_0 \nu)^{0.5}$. In the evening hours, the threshold fields and damping rates are determined by the frequency ν_e of electron collisions, whereas in the daytime the values of E_{th} and ν significantly increase, which can be naturally attributed to collisionless decay of plasma waves on photoelectrons, γ_{ph} [88].

A typical SEE spectrogram at the initial stage of the ionosphere pumping and the time course of intensity E_r^2 of the PW signal reflected from the ionosphere are presented in Fig. 2 ($f_0 = 6778$ kHz $\sim 5 f_{ce}$, $P_{eff} = 180$ MW; Sura facility) [51, 52]. Figure 3 shows the sequence of SEE spectra at

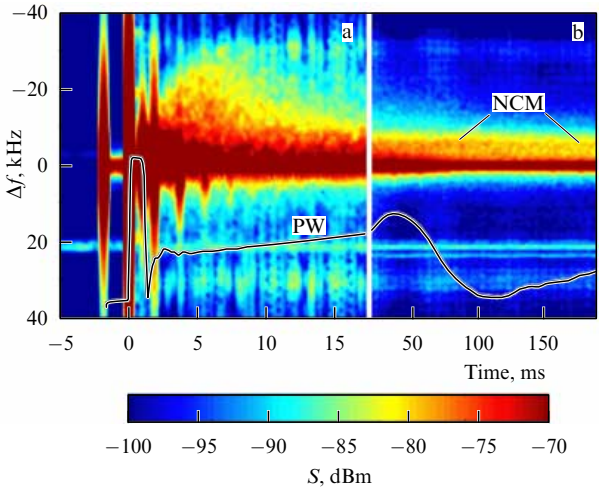

Figure 2. (Color online). An SEE spectrogram obtained by Fourier analysis for the first 20 ms (a) and 200 ms (b ionosphere irradiations by a PW with frequency resolution $\delta f = 1.25$ kHz and with 50 μs between subsequent spectra. (Sura facility, 26.09.1998, $f_0 = 6778$ kHz $\approx 5 f_{ce}$.) SEE intensity S is averaged over 12 PW pulses. Periodic (roughly 2-ms period) peaks of signal amplitude are connected with the wide wings of a PW pulse edge spectrum upon PW switch-on and switch-off, and in the case of multiple reflection from the ionosphere. The bottom curve labelled PW depicts the temporal evolution of the reflected pump wave (10 dB per scale division). NCM — narrow continuum maximum [52].

different times after PW switch-on. The behavior of the reflected PW signal and SEE oscillograms at different shifts Δf upon a vertical pumping for the currently available maximum powers $P_{eff} \sim 1.7$–1.8 GW at $f_0 = 5.45$ MHz (HAARP facility) are illustrated in Fig. 4 [89]. During a certain time τ_0 after the arrival of the reflected PW signal, the E_r^2 quantity (and, consequently the intensity of the PW after arrival of its leading edge into the region where the PW interacts with the ionosphere) remains unaltered; it must correspond to the linear PPI stage ($E_0 = \text{const}$, and

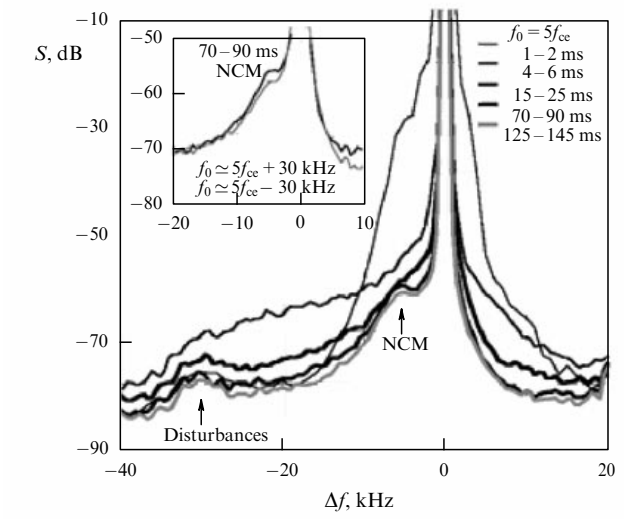

Figure 3. Spectral dynamics of the NC feature of SEE after PW switch-on.

$E_1 \propto e^{\gamma t}$). As the PW power grows, the duration of the linear PPI stage decreases from $\tau_0 \sim 4-5$ ms at $P_{\text{eff}} \sim 12$ MW to $\tau_0 \sim 0.1-0.2$ ms at $P_{\text{eff}} \sim 1.7$ GW, and PW suppression during the PSA evolvement increases from 12 to 35 dB. At such a suppression of the reflected signal, the standing PW structure must degrade for time $t \gtrsim \tau_0$, as correctly noted in Refs [19, 22].

Unfortunately, the authors of studies on numerical simulation in the framework of the STA used the dependence of a PW electric field on altitude h in the form of a standing wave, which complicates interpretation of the observed effects. To recall, PW suppression at the PSA stage at low latitudes (Arecibo Observatory) is much smaller than at middle and high latitudes (Sura, HAARP, EISCAT), in all probability due to the smaller degree of field swelling $\propto (\sin \alpha_I)^{-2/3}$ in the vicinity of the PW reflection point.

The development of PSA parallels broadening of the SEE spectrum up to the maximum width for time $t \sim \tau_{\max \text{NC}} \sim 4-6$ ms (see Figs 2–4). The SEE spectrum contains one feature at the negative frequency shifts, $\Delta f < 0$, without prominent peaks (narrow continuum, NC). This component is also referred to as NC_p or FNC (ponderomotive [85] or fast narrow continuum [36]). The spectral intensity of NC_p decreases as $|\Delta f|$ grows and the total width of the NC_p spectrum can reach 80 kHz (at HAARP facility power) [52, 85, 87, 89]. Broadening of the SEE spectrum at the PSA stage is accompanied by a lowering of SEE intensity for small

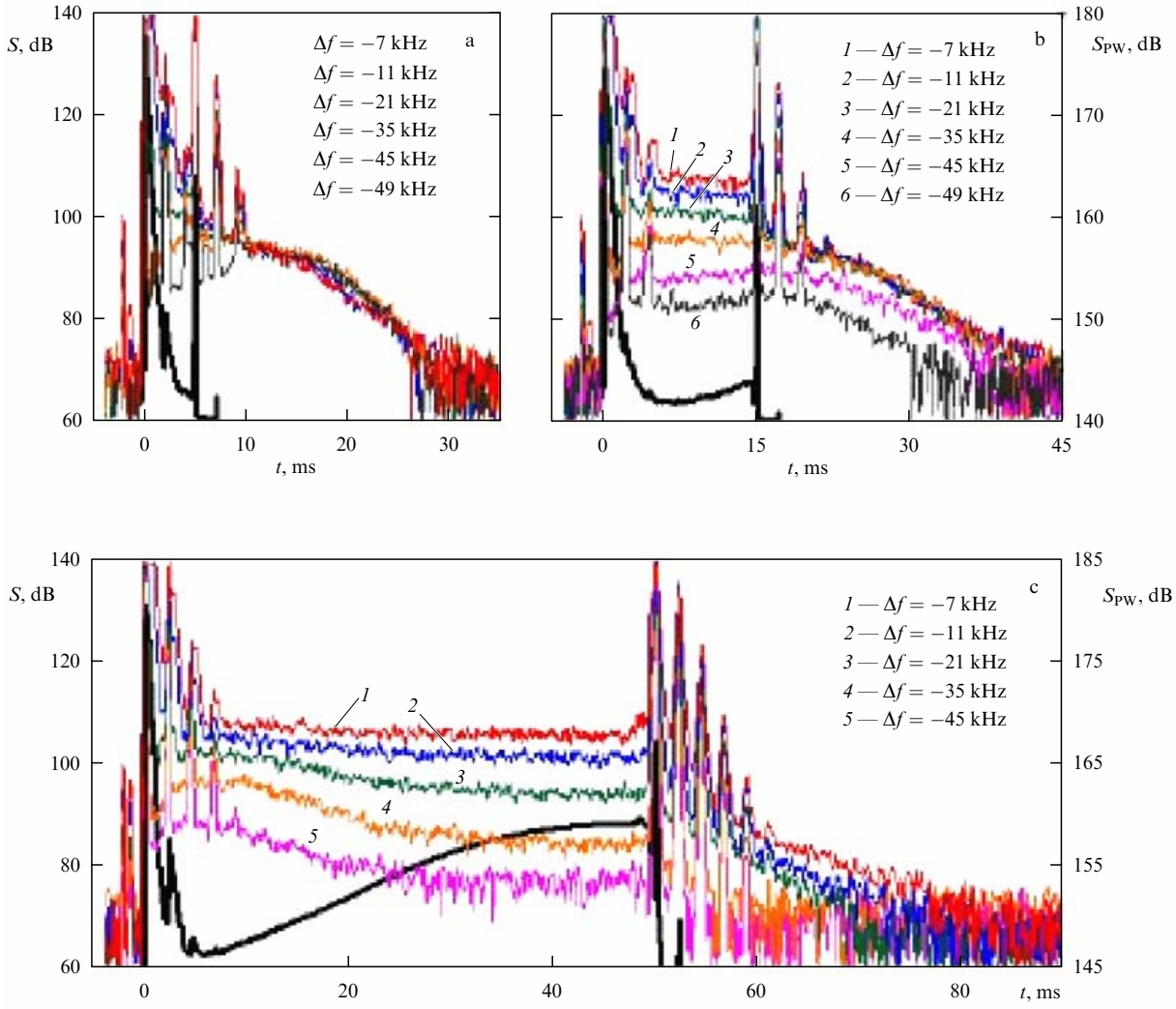

Figure 4. (Color online). PW (bold lines) and SEE oscillograms at various frequency shifts for PW pulse lengths $\tau_\text{p} = 5$ (a), 10 (b), and 50 ms (c). Averaging over 40 PW pulses. HAARP facility, 30.03.2011, 15:00–15:13 AST (UTS – 8 h), and $f_0 = 5420$ kHz [89].

$|\Delta f| < 10$ kHz (see Fig. 3). Next, for $t > \tau_{\max NC}$, the intensity of the reflected signal begins to grow, while the width and intensity of the SEE spectrum decreases (overshoot effect; see Fig. 2). Moreover, the reflected PW signal undergoes quasi-periodic damping oscillations (manifested as spikes) with increasing period $T \sim 0.05-0.5$ s (see Fig. 2). When the PW pulse duration is $t > 15$ ms, the NC spectrum begins to exhibit a readily distinguishable SEE spectral maximum (ponderomotive narrow continuum maximum, NCM) at the shifts Δf ranging from -4 to -6 kHz. This component is well apparent in the SEE spectrum in the case of long-term pumping before the evolvement of intense upper-hybrid SEE features and anomalous PW absorption.

Observations of Langmuir waves with the help of incoherent scattering radars [67, 90, 91] showed that the spectral component of a continuum type plasma line at the same shifts from f_0 as those of NC_p occurs at altitudes somewhat lower than the PW reflection point (at distances not greater than several hundred meters) within the first 10–15 ms after the PW switch-on. Simultaneously, the so-called free mode with frequency $f > f_0$ appears in the PW spectrum. In the framework of contemporary models, such modes are associated with the strong turbulence regimes. At a later time (in 20–30 ms), the plasma line is dominated by the spectra reminiscent of equidistant satellite sequences, registered far from the PW reflection point.

Such spectra are related to a cascade transfer of plasma wave energy into the low-frequency region in the WTA. However, the number of satellites appears to be smaller than predicted by the WTA, as shown by Hanssen et al. [79]. Radar observations of the plasma line allow us to distinguish plasma (Langmuir) waves with a fixed wavelength $\lambda = \lambda_{rad}/2$ propagating along the radar beam, whereas SEE has an integral nature: its generation at a given frequency f is a result of the contributions from the entire spatial spectrum of plasma waves at all altitudes where PPI develops. Therefore, the shape of the NC_p spectrum is not indicative of the strong turbulence regime. Moreover, NC_p is observed near thresholds of plasma turbulence generation, where the WTA must be valid, while any evidence of free mode-associated SEE generation is absent.

It can be concluded based on the numerous experimental data largely obtained with the Sura heating facility that neither PSA of the pump wave nor the properties of SEE features [(NC (NC_p) and NCM] generated at initial and intermediate stages of the pumping depend on the relationship between PW frequency f_0 and electron gyroharmonic frequencies sf_{ce}, at least for $s = 4, 5$ [52, 58, 92, 93], meaning that these features are related to the generation of Langmuir waves propagating along or at a small angle to geomagnetic field $\mathbf{B}_0$ (see Section 4).

Figure 4 demonstrates that SEE relaxation after PW turnoff is a two-step process: the rapid relaxation of radiation for small $|\Delta f|$ and its time delay or slowdown at the low-frequency edge of the SEE spectrum are followed by equalization of characteristic times of SEE intensity decrease for different $|\Delta f|$ at the level of $\tau_d \sim 2-4$ ms $\lesssim \nu_e^{-1}$. As the pump pulse length grows from 5 to 50 ms, an overshoot effect comes into play, and the SEE spectrum slope increases, the first relaxation stage becomes less pronounced and shifted to the smaller $|\Delta f|$ region. It is natural to interpret such a behavior along with the broadening and flattening of the spectrum after PW switch-on as a transfer of PlW energy responsible for its generation into the low-frequency region, as is typical of the WTA. For the case of induced scattering by ions, the solution of WTA equations for plasma wave spectrum dynamics reduces to considering a simple wave in the ω-space of a medium with dissipation [77, 89, 94]. It describes the main features of PlW spectrum dynamics. It appears that the dependence of SEE relaxation on pulse duration can be attributed to the variable shape of the PlW spectra at the moment of PW switch-off.

The cause behind restoration of the intensity of the reflected PW signal, its quasiperiodic oscillations, the overshoot effect for the NC_p, and the emergence of the NCM against its background may be the descent of the PPI generation region in the course of time. Swelling of the PW electric field leads to the most rapid development of PPI close to the reflection altitude h_r. Breakdown of the standing wave under the PSA effect must create a smooth height dependence of the PW electric field amplitude, and Langmuir turbulence must fill up the entire altitude interval, including standing wave minima. Moreover, Langmuir waves will propagate down from the reflection point, acquiring in this case an additional energy from the pump wave as they. This, together with the reduction of plasma background density and the resulting decrease in ω_{pe}, leads to the broadening of the PlW frequency spectrum and, therefore, of the NC_p feature in the SEE spectrum.

The wide enough spectrum of the NC_p component ($\sim 30-80$ kHz) suggests that SEE is generated at least several hundred meters below h_r; otherwise, SEE would not be able to leave the ionosphere. Energy extraction from the pump wave at these altitudes results in a decrease in its amplitude near the reflection point where the field undergoes maximum swelling and, therefore, in a decrease in the energy flux of downward Langmuir waves, PPI excitation efficiency, and PW energy extraction at lower altitudes in association with a certain increase in intensity of the reflected PW signal. Such space-time oscillations in the course of PPI excitation may correspond to observed quasiperiodic PW signal oscillations.

The appearance of an NCM in the SEE spectrum can be interpreted as an occurrence of cascade transfer associated with the development of PPI. According to formula (4), the frequency shift $|\Delta f_{NCM}|$ must increase with rising the PW intensity and time t after PW switch-on; in either case, the PPI excitation region expands downward. Such a picture was observed in experiment [52]. Also worthy of note are the closeness of characteristic times of the onset of quasiperiodic oscillations of the PW signal and NCM generation in experiments [52, 95] and the time of appearance of cascade type spectra in the plasma line of experiment [91]. Moreover, the distance (altitude) to the region of plasma line generation decreases at approximately the same rate in experiment [96], which the authors interpret as a result of plasma wave propagation down from the reflection point. The interpretation suggesting expansion of the generation region is a qualitative one and requires further theoretical consideration of the spacetime dynamics of PPI excitation region in the ionosphere.

To conclude this section, it is worthwhile to note that signals were recorded in experiments [89] at three receiving sites arrayed along the geomagnetic meridian 11, 83, and 113 km south of the HAARP location. Maximum SEE (NC feature) intensity in the case of vertical impact was observed just below the disturbed ionospheric region and markedly decreased at remote sites. Irradiation in the direction of the

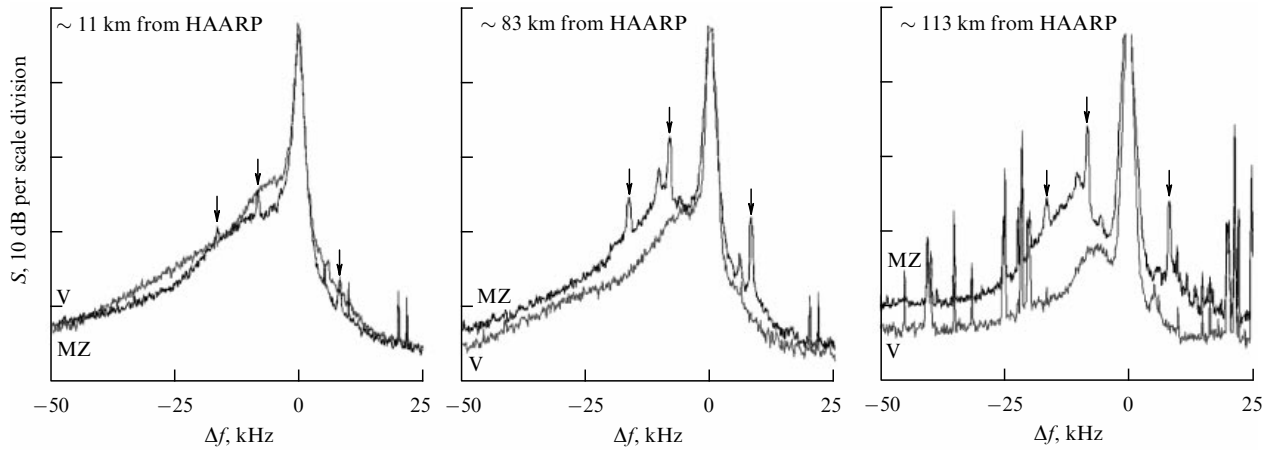

Figure 5. SEE spectra in the case of vertical pumping (V) and the sloping directional pattern of HAARP facility toward the magnetic zenith (MZ) for different observation points 20–50 ms after pumping onset [89].

magnetic zenith (along the magnetic field $\mathbf{B}_0$, with the directional pattern of HAARP tilted at an angle of 14° to the south with respect to the vertical) resulted 20 ms after impact onset in the emergence of narrow equidistant maxima in SEE spectra, associated with ±8 and ±16 kHz detunings more pronounced at the remote sites.

Examples of SEE spectra observed after 20–50 ms at the three observation points are presented in Fig. 5. Narrow spectral peaks were formed at detunings close to the lower-hybrid frequency $f_{\rm LH} \approx \sqrt{f_{\rm ce} f_{\rm ci}}$. The process of their generation awaits further detailed investigation, but it can be tentatively assumed that the most likely cause behind their appearance is the PPI development of the type resembling the splitting of the PW into upper-hybrid (UH) and lower-hybrid (LH) waves. Moreover, recent experiments at the HAARP facility revealed PPI manifestations in the form of PW decay with the participation of potential ion-cyclotron waves [97] and PW decay into electromagnetic and ion-acoustic waves [56, 57, 98] (see Section 4).

3. Thermal parametric (upper-hybrid) turbulence

3.1 Physical concepts

PW switch-on gives rise within the next $\tau \sim 0.5-5$ s to the development of thermal parametric instability (TPI) in the F-region of ionosphere, attributable to ohmic heating of the plasma in the total PW and PlW field [16, 99]. TPI excites Z-mode and/or upper-hybrid HF plasma waves, as well as small-scale ($l_\perp < \lambda_0 = c/f_0$) irregularities of plasma density markedly extended along the geomagnetic field, i.e., upper-hybrid turbulence. Thermal nonlinearity becomes more pronounced than the ponderomotive one when

$$\kappa_\parallel^2 l_{\rm e}^2 \ll 1\,, \quad \kappa_\perp^2 \rho_{\rm e}^2 \ll 1\,, \quad \tau \gg \nu_{\rm e}^{-1}\,, \tag{5}$$

where $\kappa_\parallel^{-1}$, $\kappa_\perp^{-1}$ are the characteristic longitudinal (along geomagnetic field $\mathbf{B}_0$) and transverse LF perturbation scales, and $l_{\rm e} = V_{T_{\rm e}}/\nu_{\rm e}$ and $\rho_{\rm e} = V_{T_{\rm e}}/\omega_{\rm ce}$ are the mean free path and gyroradius of thermal electrons, respectively. Beating of the PW and PlW during TPI excitation creates an inhomogeneous source of electron heating $Q \propto \nu_{\rm e}(\mathbf{E}_0\mathbf{E}_1)$. Thermal diffusion promotes plasma displacement from heated regions and the generation of small-scale irregularities (striations) of plasma density, which are strongly extended along a magnetic field. Plasma waves, in turn, arise as a result of PW scattering on the striations. Matching conditions must be fulfilled in the process of TPI formation:

$$\omega_0 = \omega\,, \quad \mathbf{k}_0 = \mathbf{k} \pm \boldsymbol{\kappa}\,. \tag{6}$$

Thus, instability is aperiodic. The very apparent extension of irregularities along the geomagnetic field $\mathbf{B}_0$ ($|\kappa_\parallel| \ll |\kappa_\perp|$) is due to the sharply anisotropic character of transfer processes in the magnetoactive plasma (ionosphere): diffusion and thermal conductivity across the magnetic field for $\nu_{\rm e}, \nu_{\rm i} \ll \omega_{\rm ce}, \omega_{\rm ci}$ prove to be strongly suppressed [2, 100]. Because $|\mathbf{k}_0| \ll \mathbf{k}$ and $|\kappa_\parallel| \ll |\kappa_\perp|$, the plasma wave being generated must be almost orthogonal to $\mathbf{B}_0$, i.e., TPI develops close to the PW upper-hybrid resonance (UHR) level where

$$\omega_0^2 = \omega_{\rm pe}^2 + \omega_{\rm ce}^2 = \omega_{\rm UH}^2\,. \tag{7}$$

The threshold TPI field in a homogeneous plasma is significantly lower than the PPI threshold and is given by the expression [16]

$$\frac{E_{\rm th}^2}{8\pi N_{\rm e} T_{\rm e}} = \frac{1}{|\mathbf{a}_0\mathbf{a}_1|^2}\,\frac{\delta\nu_{\rm e}}{\omega_0}\,(1 + \kappa_\parallel^2 L_{\rm T\parallel}^2 + \kappa_\perp^2 L_{\rm T\perp}^2)\,, \tag{8}$$

where $\delta\nu_{\rm e}$ is the characteristic time of establishing the electron temperature in the plasma, $\delta \ll 1$ is the fraction of energy lost by an electron in a single collision with a heavy particle (ion or neutral); $L_{\rm T\parallel} = l_{\rm e}/\sqrt{\delta}$ and $L_{\rm T\perp} = \rho_{\rm e}/\sqrt{\delta}$ are the characteristic lengths of the longitudinal and transverse thermal conductivities of electrons. In other words, the TPI threshold in a homogeneous plasma is much lower than the PPI threshold.

The threshold TPI field in a regularly inhomogeneous plasma (ionosphere) can be evaluated from simple energy considerations, because it is determined by the input-to-lost energy ratio. Indeed, the size of the energy release (plasma heating) region will be determined in this case by the length $l_{\rm mc}$ of the interaction region between the PW, PlW (Z-mode), and striations (matching conditions): $l_{\rm mc} = (1/\pi)|\partial\Delta k(z_{\rm mc})/\partial z|^{-1/2} \simeq |\partial[k_z(z_{\rm mc})]/\partial z|^{-1/2}$ near point $z_{\rm mc}$ where conditions (6) ($\mathbf{k}_0 \parallel z \parallel \nabla N$, $\Delta k = k_0 - k_z = 0$ at $z = z_{\rm mc}$)

are fulfilled. This energy will be distributed along the thermal conductivity length $L_T = L_{T\parallel}(1+\kappa^2 L_{T\perp}^2)^{-1/2} \gg l_{mc}$. Moreover, the PlW lifetime in the interaction (matching) region is now determined by the time of group propagation $l_{mc}/V_{gz} \ll \nu^{-1}$ through the matching region rather than by PlW decay time ν^{-1}. Therefore, the overall decrease of interaction efficiency will be characterized by the factor $\beta = [l_{mc}/(V_{gz}/\nu)]\,(l_{mc}/L_T) \ll 1$. Taking advantage of the explicit relations

$$\left|\frac{\partial k_z}{\partial z}\right| = \left[\frac{\partial \varepsilon}{\partial k_z}\right]^{-1} \frac{\partial \varepsilon}{\partial z}\,,$$

$$|V_{gz}| = \left|\frac{\partial \omega}{\partial k_z}\right|_{\varepsilon=0} = \left|\frac{\partial \varepsilon}{\partial k_z}\right| \left|\frac{\partial \varepsilon}{\partial \omega}\right|^{-1},$$

$$\left|\frac{\partial \varepsilon}{\partial z}\right| = \frac{1}{L}\,, \qquad \frac{\partial \varepsilon}{\partial \omega} \approx \frac{2}{\omega}$$

(where $\varepsilon(\omega, k)$ is the scalar dielectric constant) and multiplying the right-hand side of formula (8) by β^{-1}, we arrive at the TPI threshold in an inhomogeneous plasma:

$$\frac{E_{th}^2}{4\pi N_e T_e} \sim \frac{1}{|\mathbf{a}_0 \mathbf{a}_1|^2} \frac{L_{T\parallel}}{L} (1 + \kappa_\perp^2 L_{T\perp}^2)^{1/2}\,. \tag{9}$$

This estimate is confirmed by a more strict calculation reported in paper [101] based on the equations for ambipolar diffusion and electron thermal conductivity:

$$\frac{\partial n}{\partial t} - \nabla \hat{D}_a \nabla n - k_T \frac{N_e}{T_{e0}} \nabla \hat{D}_a \nabla T_e = 0\,, \tag{10}$$

$$\frac{\partial T_e}{\partial t} - \nabla \hat{D}_T \nabla T_e + \delta \nu_e T_e = Q\,, \tag{11}$$

and the transfer equations for plasma wave amplitudes (Z-mode) in the geometrical optics approximation. N_e and T_{e0} entering Eqns (10) and (11) are the initial electron concentrations and temperature, $n \ll N_e$ and $T_e \ll T_{e0}$ are striation-associated perturbations of electron density and temperature, the tensors of ambipolar diffusion $\hat{D}_a$ and thermal conductivity $\hat{\chi}_e = N\hat{D}_T$ were taken in the elementary approximation, $k_T \sim 1$ is the thermodiffusion ratio, and δ is the fraction of energy lost by an electron in a single collision with a heavy particle [2]:

$$D_{a\parallel} = 2l_i^2 \nu_{in}\,, \quad D_{a\perp} = 2\rho_e^2 \nu_e\,, \quad D_{T\parallel} = l_e^2 \nu_e\,, \quad D_{T\perp} = \rho_e^2 \nu_e\,. \tag{12}$$

The dependence of the instability growth rate on $\kappa_\perp^2 L_{T\perp}^2$ at different $E^2/E_{th,min}^2$ is shown in Fig. 6. The minimum instability threshold occurs in the region of large enough scales $\kappa_\perp^2 L_{T\perp}^2 \ll 1$. At certain optimal values of $(\kappa_\perp^2 L_{T\perp}^2)_{opt}$, depending on E^2/E_{th}^2, the increment $\gamma_{max} \gg \delta\nu_e$ reaches a maximum. At sufficiently high values of the maximum increment ($\gamma_{max} \gg \delta\nu_e$) and for $(\kappa_\perp^2 L_{T\perp}^2)_{opt} \gg 1$, the following expressions hold:

$$\gamma_{max} \approx 0.6\delta\nu_e \left(\frac{E_0}{E_{th,min}}\right)^4 \text{ at } (\kappa_\perp^2 L_{T\perp}^2)_{opt}$$

$$\approx 0.75 \left(\frac{E_0}{E_{th,min}}\right)^4. \tag{13}$$

Such a behavior of the instability threshold and increment is determined, depending on $\kappa_\perp L_{T\perp}$, by the balance between the enhanced displacement of the plasma from heated regions owing to thermal diffusion [the third term on the left-hand side of equation (10)] and the increased striation dissipation as a result of transverse ambipolar diffusion and thermal conductivity [the second terms on the left-hand sides of Eqns (10), (11)] upon a rise in $\kappa_\perp$ (decrease in the striation transverse scale).

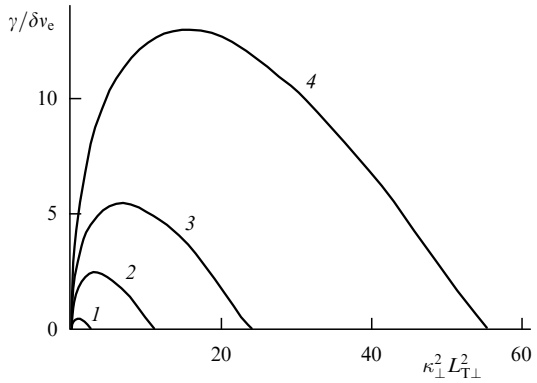

Figure 6. The plots of TPI growth rate vs $\kappa_\perp^2 L_{T\perp}^2$ at $E^2/E_{th,min}^2$ values equaling 2 (curve *1*), 3.5 (curve *2*), 5 (curve *3*), and 7.5 (curve *4*) [62].

It is worthwhile to note that the set of equations of two-liquid hydrodynamics describing particle transfer in partly ionized plasma in a magnetic field [2, 100] can be reduced to a single equation for the concentration n, i.e., to the ambipolar diffusion equation (10), only in certain special cases [102, 103], e.g., for a plasma with a high enough degree of ionization:

$$m_e \nu_{ei} > m_i \nu_{in} \tag{14}$$

(ν_{ei}, ν_{in} are the frequencies of electron collisions with ions and ions with neutral particles) or for perturbations of the concentration greatly extended along the magnetic field:

$$\frac{l_\parallel}{l_\perp} > \frac{l_e}{\rho_e}\,. \tag{15}$$

At the same time, according to paper [104], point perturbations of the plasma density spread in the unipolar manner. Additional mathematical difficulties are encountered in the consideration of irregularities having transverse scales $l_\perp < \rho_i$ ($\rho_i = V_{Ti}/\omega_{ci}$ is the cyclotron rotation radius of ions). The equations describing the evolution of density and electron temperature perturbations were devised in Ref. [105] for this limiting case and have a much more complicated form than equations (10) and (11). An important role in irregularity dynamics is played by the nonpotentiality of the low-frequency electric fields being excited and various LF nonlinearities [105–108].

Under typical ionospheric conditions, the characteristic time for settling the electron temperature, $(\delta\nu_e)^{-1}$, is roughly 30 s, and the characteristic length of transverse thermal conductivity is $L_{T\perp} = \rho_e/\sqrt{\delta} \sim 2.5$ m.

It follows from expressions (8), (9) that the threshold field is defined (with all other things being equal) by the scalar product of the PW and PlW polarization vectors $|\mathbf{a}_0 \mathbf{a}_1|$. Because $\mathbf{a}_1 \parallel \mathbf{k}$, $\kappa \approx k$ and $\boldsymbol{\kappa} \perp \mathbf{B}_0$, efficient interaction among PW, PlW, and striations occurs only when the PW electric field has a large enough component orthogonal to the magnetic field, $\mathbf{E}_0 \perp \mathbf{B}_0$, i.e., the quasilongitudinal approx-

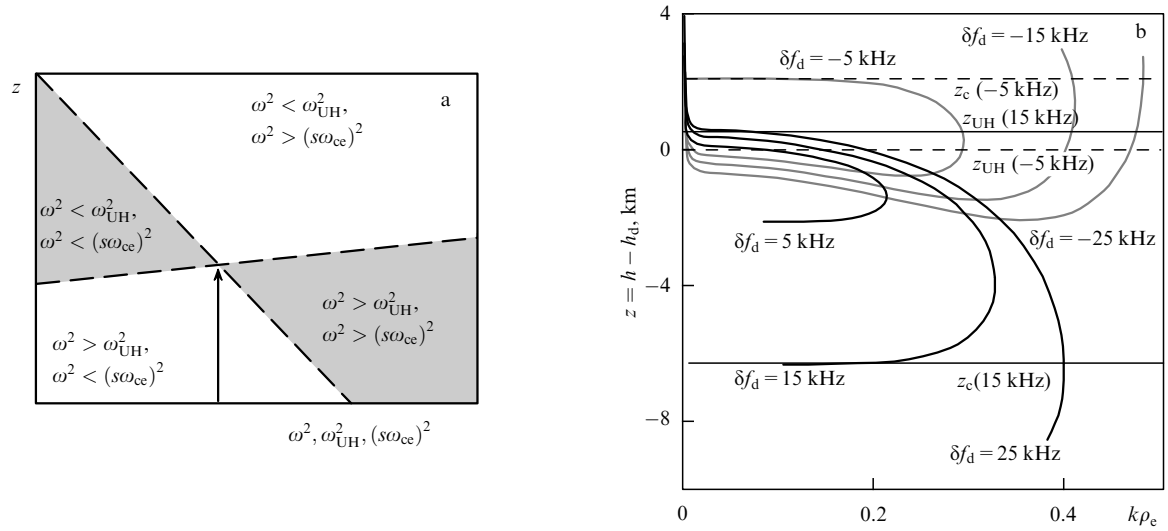

Figure 7. (a) Schematic illustration of the existence domains (shaded) of plasma waves propagating across the magnetic field in the ionosphere below the F-layer maximum in accordance with dispersion equation (18). The vertical arrow corresponds to $\omega = \omega_d$, with the transverse plasma waves being nonexistent. (b) Dependences of the transverse plasma wavenumber on altitude z in the vicinity of double resonance $z = 0$ at different PlW offsets from the double resonance frequency, $\delta f_d = f - f_d$ [58]. Horizontal lines denote altitudes at which frequencies of plasma waves with $\delta f_d = -5$ kHz (dashed lines) and $\delta f_d = 15$ kHz (light solid lines) coincide with the upper-hybrid frequency (z_{UH}) and the fourth electron gyroharmonic (z_c).

imation [inverse inequality for formula (3)] needs to be fulfilled in the UHR region (7) for the PW [17]:

$$\omega_0 \sin^2 \alpha > 2\,|\omega_{ce} \cos \alpha|, \quad \alpha = \angle \mathbf{k}_0 \mathbf{B}_0\,. \tag{16}$$

For quasitransverse PW propagation in the UHR region one has $\mathbf{E}_0 \parallel \mathbf{B}_0$, $|\mathbf{a}_0 \mathbf{a}_1| \to 0$, and the interaction between pump and plasma waves becomes much weaker and dependent mostly on PPI-related effects. Such a situation takes place in Arecibo experiments.

Moreover, the efficiency of TPI development is markedly lowered near gyroharmonics at $\omega_0 \approx s\omega_{ce}$, because the existence of transverse (with $\mathbf{k} \perp \mathbf{B}_0$) plasma waves in the double resonance region of the ionosphere,

$$\omega^2 = \omega_d^2 = \omega_{UH}^2 = s^2 \omega_{ce}^2\,, \tag{17}$$

is forbidden [109–111]. This fact is easy to illustrate by an approximate dispersion equation for transverse plasma waves (disregarding frequency corrections to the upper-hybrid waves arising because they are not purely electrostatic ($\propto \omega^2/c^2k^2$) and thermal electron movements ($\propto k^2 V_{Te}^2/\omega^2$)):

$$\left[\omega^2 - \omega_{UH}^2(z)\right]\left[\omega_l^2 - s^2\omega_{ce}^2(z)\right] = c(s)\,\omega_{ce}^2 \omega_{pe}^2 (k\rho_e)^{2(s-1)}\,, \tag{18}$$

where $c(s)$ is the coefficient of order unity, depending on the harmonic number s. It can be seen that solutions of equation (18) for $k^2 > 0$ corresponding to propagating waves exist only on condition that the expressions in brackets on the left-hand side of equation (18) have the same signs (for $\omega > \omega_{UH}$, ω_{ce} or $\omega < \omega_{UH}$, ω_{ce}, i.e., between upper-hybrid and multiple cyclotron resonances, see shaded regions in Fig. 7a). The existence of transverse PlWs is impossible when the frequency coincides with the double resonance frequency at a certain altitude h_d, since the left-hand side of expression (18) is negative at all heights, and TPI is not excited at $\omega_0 = \omega_d(h_d)$.

It follows from the dependence $k(z = h - h_d)$ at $\mathbf{k} \perp \mathbf{B}_0$ and different $\delta\omega = 2\pi\delta f = \omega - \omega_d$, with due regard for the thermal motion (the dielectric permittivity tensor being calculated in the kinetic approximation) and electromagnetic corrections $\propto \omega^2/c^2k^2$ (Fig. 7b), that transverse propagation at $\omega = \omega_d$ is not totally forbidden, bearing in mind that transition to the dependence $k(z)$ corresponding to the Z-mode takes place for $k \to 0$, $\omega < \omega_{UH}$. Nevertheless, as $\omega \to \omega_d$, the existence domain of PlWs with large enough $k_\perp$ propagating transversely or almost transversely to the magnetic field, decreases both in real space and in the wave vector space. At $\omega \approx \omega_d$, forbidden zones appear on the $\{\omega; k_\perp\}$ plane in which plasma waves cannot exist, because their phase incursions during propagation along the z-axis between the turning points given by relation $k_\parallel = 0$ (intersections of the curves shown in Fig. 7b and the vertical lines corresponding to $k_\perp = \text{const}$) prove smaller than π [110, 111]. The presence of such zones in the double resonance region of the ionosphere, along with enhancement of cyclotron damping [93], is one of the causes of marked weakening of the interaction between high-power radio waves and the ionospheric plasma, including TPI excitation at $\omega_0 \approx s\omega_{ce}$. In the case of a certain PW frequency ω_0 deviation from $s\omega_{ce}$, a weak regular nonuniformity of the magnetic field (Fig. 7b) results in the appearance of a maximum in the $k(z)$ dependence and, as a consequence, in a significant increase in synchronism length l_{mc}, because in the case $|\partial\varepsilon/\partial z| = 1/L \to 0$. This, in turn, leads to a considerable (10-fold) decrease in the TPI threshold, in comparison with the far-from resonance case [109, 112].

Because $l_{mc} \ll (V_{gz}/\nu)$, L_T, z_L ($z_L = h_r - h_L$ specifies the size of the domain where the PlWs exist), interaction among the PW, striations, and PlW is concentrated in the narrow vicinity of the matching point z_{mc}, while a smoothly inhomogeneous medium is characterized by the unambiguous dependence of z_{mc} on the value of wave vector $\boldsymbol{\kappa}$ (of $|\boldsymbol{\kappa}|$ at $\mathbf{B}_0 \parallel z$) and PW frequency ω_0. This dependence is defined by the dispersion relation for plasma waves, $\omega = \omega(\mathbf{k}, N_e, \mathbf{B}_0)$, when the conditions (6) are fulfilled. In this case the source of heating is $Q(z) \propto \delta(z - z_{mc}(\boldsymbol{\kappa}, \omega_0))$ ($\delta(z)$ is the Dirac delta-function).

At the stage of developed TPI, simultaneously with the growth of striation amplitudes, Δn (for $\delta n = \Delta n/N_e > \nu_e/\omega_0$), and plasma waves, electron heating by plasma waves, $Q_1 \propto \nu_e |\mathbf{E}_1\,\mathbf{E}_1'|$, becomes more efficient than heating from

PW–PlW interaction, Q. The involvement of source Q_1 further intensifies the density perturbation and energy transfer from PW into PlW. The process acquires the character of explosive instability ($\Delta n \propto (t-t^*)^{-1}$, t^* is the characteristic time). The authors of Refs [15, 61] called such instability 'resonant instability'. The presence of initial LF perturbations (δn_0) in the plasma results, by force of the aforementioned circumstances, in the lowering of the TPI threshold:

$$\frac{E_{\mathrm{th},1}^2}{E_{\mathrm{th}}^2} = \frac{-1+\sqrt{1+\omega_0^2\,\delta n_0^2/2\nu_\mathrm{e}^2}}{\omega_0^2\,\delta n_0^2/4\nu_\mathrm{e}^2}\,. \tag{19}$$

Here, E_{th}^2 is the minimum threshold field (as $\kappa_\perp \to 0$) defined by expression (8). Evidently, at small initial density perturbations $\delta n_0 \ll \nu_\mathrm{e}/\omega_0$, the TPI threshold (18) coincides with (8). For $\delta n_0 \gg \nu_\mathrm{e}/\omega_0$, the threshold is totally determined by initial perturbations and coincides with the resonant instability threshold.

At a high enough striation intensity, $\omega^4 \delta n^2 \gg \omega_{\mathrm{ce}}^4$, it is also necessary to take account of multiple scattering of plasma waves on striations, which is responsible for the smearing of their energy over the large phase volume of spatial scales. In the end, the spectral density of PlW energy turns out to be uniformly distributed within the $[0, (k_{\perp\max})]$ interval, where $k_{\perp\max}$ is the maximally possible value of the transverse plasma wavenumber found from the PlW dispersion equation [62, 109]. Therefore, while the plasma waves with the wave vectors almost orthogonal to the magnetic field ($\mathbf{k} \perp \mathbf{B}_0$) are excited at the initial stage of TPI development, the PlW angular spectrum markedly expands at the developed TPI stage. Moreover, plasma waves become so intense that they begin to be directly involved in pumping energy through the frequency spectrum, as they are in the case of PPI [113, 114].

Saturation of the TPI in the ionospheric plasma is due to spatial decay (anomalous absorption, AA) of the pump wave as it is scattered into the PlW on the striations with the spatial intensity spectrum $n_{\boldsymbol{\kappa}}^2$:

$$W_0(z) = W_0(z_\mathrm{L})\,\exp\left\{-\,\Gamma\big(z(\boldsymbol{\kappa})\big)\right\},$$
$$\Gamma\big(z(\kappa)\big) \approx \int_{\kappa(z)}^{\infty} \frac{\pi\omega_0 L}{2V_0}\; n_{\boldsymbol{\kappa}}^2\,\mathrm{d}\boldsymbol{\kappa}. \tag{20}$$

Here, V_0 is the group velocity of the PW, $\Gamma(z)$ is the 'current' AA (an analog of optical depth in a medium containing striations), and W_0 is the PW energy density. In a plasma of lower density N_e, the matching conditions (6) are fulfilled at greater $k_\perp$ and κ values. Integration in formula (20) is performed from $\kappa(z)$ to the maximally possible κ, and the minimum value of $\kappa_{\min} \approx \omega_0/c$ is determined by the PW dispersion equation in the approach from below to the boundary between quasi-longitudinal and quasitransverse propagations (16). The overall anomalous attenuation of a PW propagating through the turbulence zone up to the reflection point and back is $2\Gamma(\kappa_{\min})$.

A more detailed description of the TPI theory at the saturation stage, constructed in the weak turbulence approximation, can be found in Ref. [62] (see also papers [115–117]), where the shape of the spatial striation spectrum, the dependence of striation intensity on the PW power, and PlW spectral density as a function of altitude h were calculated. This theory allows many experimental data to be interpreted. At the same time, the problem of applicability of such an approach must be addressed based on the complete set of nonlinear equations describing thermal stratification of the plasma in a magnetic field. Specifically, the influence of large enough irregularity amplitudes, $\delta n > k^2 d_\mathrm{e}^2$, on PlW dispersion properties must be taken into account. Also, excitation of thermal modulation instability of upper-hybrid waves and their trapping by the striations should be considered. In this case, trapping of upper-hybrid waves into isolated deep striations with pre-determined parameters is, as a rule, given most attention, taking into account wave leakage across irregularity borders in the course of its transformation into the Z-mode and linkage between adjacent striations via the Z-mode. The temperature dependence of transport coefficients [diffusion and thermal conductivity; see formula (12)], i.e., effects of low-frequency nonlinearities, may have a noticeable influence on the striation shape and amplitude (when the latter is large enough). These issues are considered in many publications (see papers [118, 119] and references cited therein).

Because the high energy density of plasma waves is responsible for the formation of their wide frequency spectrum through the influence of ponderomotive nonlinearity, the latter must be included in consideration when constructing the theory of thermal parametric turbulence. The description of upper-hybrid wave turbulence arising in the TPI process at high enough pumping intensities implies consideration of the formation of Langmuir condensate, oscillating two-stream instability, and collapse associated with ponderomotive nonlinearity. In high-power heating facilities, the PPI threshold for the PW field can be exceeded in the UHR region. In this case, plasma waves in the UHR region must arise from the PPI, and striations from heating by plasma waves (source Q_1). Moreover, the striations must result from thermal self-focusing of Langmuir waves (the same source Q_1) formed in the course of PPI development [14].

Processes of modulation instability, soliton formation, and collapse in the case of upper-hybrid waves were considered in Refs [120–123].The theory of ponderomotive parametric instabilities of upper-hybrid oscillations trapped in the PSI is developed in Refs [119, 124, 125]. It is worthwhile to note without going into details of these publications that they disregard regular inhomogeneity of the medium and nonunidimensionality of the process proceeding across the magnetic field (either one-dimensional or cylindrical symmetric structures are considered), nor do they take into account the possibility of 'oblique' (not orthogonal to the magnetic field) waves; the exception is work [122] illustrating the possibility of the appearance of multisoliton structures for thermal nonlinearity). All these factors needed to interpret experimental results continue to attract the attention of researchers and await further analysis.

3.2 Brief summary of experimental results

Under experimental conditions, striations manifest themselves via anomalous absorption of pump waves and probing radio waves with close frequencies $|f - f_0| < f_0\,(L_\mathrm{T}|\cos\alpha|/L)$ and via aspect angle scattering of short and ultrashort radio waves. Furthermore, a geophysical rocket was launched in 1992 at the Arecibo Observatory, intended to pass through the perturbed ionospheric region. During this rocket flight, the unique till present striation measurements *in situ* were performed [126, 127].

Anomalous absorption is a result of PW scattering on the striations into upper-hybrid waves and the Z-mode; it

develops together with the striations and is accompanied by restoration and quasiperiodic oscillations of the reflected PW signal. Once the Bragg–Wulff condition is fulfilled ($\mathbf{k}_1 - \mathbf{k}_s = \pm\boldsymbol{\kappa}$, $\boldsymbol{\kappa} \perp \mathbf{B}_0$, $\kappa = 2k_1 \sin(\theta_s/2)$, $\theta_s = \angle \mathbf{k}_1\mathbf{k}_s$), the aspect scattering maintains wave propagation between the corresponding points located at the intersection of Earth's surface and cone surfaces housing wave vectors of incident ($\mathbf{k}_1$) and scattered ($\mathbf{k}_s$) ($k_1 = k_s$) waves, the axis of which is directed along the magnetic field $\mathbf{B}_0$, and the apex lies in the center of the scattering region [3, 10, 25]. The intersection of the elements of these cones with Earth's surface determines conjugate aspect contours. A signal from a transmitter located at one of the contours can be received at any point of another contour if the striation spatial spectrum comprises a component with a spatial frequency $\kappa = 2k_1 \sin(\theta_s/2)$. A backscattering contour resides between the conjugate contours, for which $\theta_s = \pi\kappa = 2k_1$. Intensity of the scattered signal is proportional to striation spectral density $n^2_{\boldsymbol{\kappa}}$.

The striation spectral and dynamic properties are described in much detail in Refs [7, 8, 10, 25, 26, 45–47, 128]. In what follows, only certain main characteristics of upper-hybrid turbulence are mentioned. The threshold striation generation field is $\mathbf{E}_{th} \sim 40$ mV m^{-1} or smaller than both TPI theoretical values of ~ 100 mV m^{-1} (9) and the PPI threshold. This appears to be due to the presence of initial priming irregularities in the ionosphere or to PW focusing on mid-scale irregularities and, as a consequence, to PW electric field strengthening. The switch-on of the PW induces a smooth growth of the striations followed in 1–7 s by an 'explosive' stage with a characteristic time of < 1 s, and thereafter by the smooth achievement (over a few seconds) of the steady-state level. The horizontal size of the disturbed ionospheric region depends on threshold field $\mathbf{E}_{th}$, the power of the heating transmitter, and the transmitter antenna pattern. The diameter of the perturbed region at the stable regime varies between 50 and 200 km. The vertical size Δh of the striation region is determined by the thermal conductivity length $L_T = L_{T\parallel}(1 + \kappa^2 L^2_{T\perp})^{-1/2}$ and may be as high as ~ 15 km for $l_\perp = 2\pi/\kappa = 1.5-3$ m. It increases to 20–30 km for $l_\perp = 10-25$ m. At $l_\perp = 40-90$ m, the striation region extends for more than 50 km down from the PW reflection point.

As striations develop (within a few seconds after PW turn-on), practically the whole PW energy flux is absorbed in the PW UHR region due to AA. It puts an end to excitation of the PSA effect and quasiperiodic oscillations of the reflected PW signal (see Section 6 for details). Such a situation takes place at subauroral and mid-latitude facilities but not in Arecibo, where AA is virtually absent and the source of electron heating (and, therefore, of experimentally observed striations) [126, 127] might be attributed to Langmuir waves generated with the development of PPI. Striation generation as a result of thermal self-focusing of Langmuir waves was obtained in experiment [129], which revealed rapid development (for ~ 0.2 s) of anomalous absorption of probing waves having a UHR height coincident with the PW reflection altitude.

The formation and relaxation of striation spectra have been studied in a number of theoretical articles [62, 107, 130]. Calculations qualitatively adequately describe characteristic properties of the striations. At the same time, the long-term exploration of the disturbed ionospheric region making use of aspect scattering demonstrated that striations' properties undergo appreciable changes depending on the time of day, geophysical conditions, and geometry of the experiment; only a single *in situ* striation measurement with the help of a geophysical rocket is available. It was proposed to retrieve the shape and intensity of the striation spectrum (parameters of the empirical model) from the results of measurements and modeling of the generation of the SEE broad continuum (BC) component regardless of simultaneously obtained aspect scattering data [30, 114, 131] (see Section 4).

To simulate SEE generation, it is convenient to rely on the empirical model of the striation spectrum, based on results of numerous experiments on aspect scattering of HF and VHF radio waves and/or rocket experiment data. According to this model, the spectral density $n^2_{\boldsymbol{\kappa}_\perp}(t, z)$ of the striation intensity can be presented in the form [30, 45, 127]

$$n^2_{\boldsymbol{\kappa}_\perp} = \Delta n^2(P_{eff})\, \Phi_\perp(\kappa_\perp)\, \Phi_\parallel(\kappa_\perp, z)\, T_3(t, \kappa_\perp, P_{eff})\, T_{rel}(t, \kappa_\perp), \tag{21}$$

where $\Delta n^2(P_{eff})$ is the integral striation intensity for long heating of the ionosphere by continuous PW, depending on PW power: $\Delta n^2 \propto (P_{eff})^\beta$, where exponent β varies in the experiment over the range $\beta \sim 0.3-1$ with the mean value of $\overline{\beta} = 0.5$. Function $\Phi_\perp(\kappa_\perp)$ describes the shape of the two-dimensional ($\perp \mathbf{B}_0$) spatial striation spectrum in the stationary state in the center of the disturbed ionospheric region (at the PW UHR altitude). According to papers [7, 45], the shape of the stationary striation spectrum can be regarded as power-law one with a sharp cutoff at a certain maximum value $\kappa_{max} = 2\pi/l_{\perp min}$ ($l_{\perp min} \sim 0.5-1$ m), so $\Phi_\perp(\kappa_\perp) \propto \kappa_\perp^{-p}$ and exponent p can vary from 1 to 4 (most frequently, $p \sim 3$). A sharp drop in striation spectral intensity at $\kappa \sim l_{\perp min}$ was observed in aspect scattering experiments at the Platteville facility [7]. Results of the rocket experiment [126, 127] show that function $\Phi_\perp(\kappa_\perp)$ in the expression for the striation spectrum was approximated in the following way:

$$\Phi_\perp(\kappa_\perp) = \frac{l_0^2}{(2\pi)^{0.5}} \sin \frac{1.5 \arctan (\kappa_\perp l_0)^{-2}}{[1 + (\kappa_\perp l_0)^4]^{0.75}}\,.$$

For $\kappa < 2\pi/l_0$ ($\kappa > 2\pi/l_0$), the spectrum is close to the power-law one with $p = 0$ ($p = 5$). Function

$$\Phi_\parallel(\kappa_\perp, z) = \exp\left\{-2z^2 \frac{1 + 2\kappa^2 L^2_{T\perp}}{L^2_{T\parallel}}\right\}$$

takes account of the variation of the striation intensity with altitude h (the distance from the center of region $z = h - h_{UH}$, and h_{UH} is the altitude of the PW UHR). Function $T_3(t, \kappa, P_{eff})$ describes the development of striations of different scales after PW switch-on and takes the form $T_3(t, \kappa, P_{eff}) = (1 - \exp\{-t/\tau_3(\kappa, P_{eff})\})^2$, where $\tau_3 = (100/P)(\kappa^*/\kappa)^{0.4}$ is the characteristic formation time of striations on different scales, $\kappa^* = 2\pi/10$ m^{-1} is the normalization scale, and t is the elapsed time from the PW switch-on. Function $T_{rel}(t, \kappa)$ describes relaxation (diffuse spreading) of irregularities after PW switch-off:

$$T_{rel}(t, \kappa_\perp) = \begin{cases} 1, & 0 < t < t_0\,, \\ \exp\left\{\dfrac{-2(t - t_0)}{\tau_{rel}}\right\}, & t_0 < t < t_0 + \tau_{rel}\,, \\ \exp\left\{\dfrac{-2 - 2(t - (t_0 + \tau_{rel}))}{(\eta\tau_{rel})}\right\}, & t > t_0 + \tau_{rel}\,. \end{cases} \tag{22}$$

Here, t_0 is the PW switch-off time, τ_{rel} is the characteristic relaxation time of a striation with transverse scale

$l_\perp = 2\pi/\kappa_\perp$. According to paper [45], $\kappa_\perp = \kappa^* = 2\pi/l_\perp^*$ is associated with a change in the character of striations' relaxation: transverse ambipolar diffusion with $\tau_{\rm rel} = \tau^*(\kappa^*/\kappa_\perp)^2$ prevails for $\kappa_\perp > \kappa^*$, and the longitudinal one with $\tau_{\rm rel} = \tau^*(\kappa^*/\kappa_\perp)^{0.5}$ at larger scales $\kappa_\perp < \kappa^*$. The quantity $l_\perp^*$ changes from daytime to nighttime, depending on various geophysical conditions. In daytime, $l_\perp^* \sim 6-10$ m; at nighttime, $l_\perp^* \sim 3$ m. The typical relaxation time of a striation with $l_\perp \sim l_\perp^*$ is $\tau^* = 10$ s in the daytime, and increases two-fold at night. Relaxation slows down after time $\sim \tau_{\rm rel}$ [45] in accordance with the last expression in formula (22), where moderation factor $\eta = 5(\kappa^*/\kappa)^{0.5}$. A detailed description of the empirical striation model is included in the present review because it helps to estimate the scales of striations responsible for generating various spectral components of SEE and certain peculiarities of its dynamics (see Section 4.3).

Measurement of Doppler spectra of signals undergoing aspect scattering in the Sura experiments showed that (1) the spectrum consists of the central narrowband (~ 0.2 Hz) portion and the broadband part (~ 1 Hz) that relaxes much faster after PW switch-off, (2) parameters of the scattered signal undergo quasiperiodic changes with a period of 2–5 min, (3) spectra of scattered signals undergo steady splitting ($\Delta f \sim 0.2-0.8$ Hz) that can be interpreted as the relative motion of irregularities with a speed of ~ 3 m s^{-1}, and (4) signal intensity and spectrum width are minimum at $f_0 \approx sf_{\rm ce}$; the values of these parameters for $f_0 > sf_{\rm ce}$ exceed the respective values for $f_0 < sf_{\rm ce}$ [45, 132, 133]. To recall, aspect scattering of probing (scattered) signals in the VHF (meter-long) range can be observed only at rather low latitudes and large enough tilt of magnetic field lines about the vertical due to their practically rectilinear propagation (absence of refraction). At tilt angles $\alpha_I < 16^\circ$, the conjugate cones (at least one of them) do not cross Earth's surface if scattering on striations occurs at an altitude of about 250 km. Wave refraction in the HF range is responsible for the bending of probing and scattered wave propagation paths, such that they enter the scattering region and fall onto Earth's surface, respectively, at rather small angles.

4. Stimulated electromagnetic emission of the ionosphere

Stimulated electromagnetic emission of the ionosphere was revealed with the EISCAT facility in 1981 [35]. Thereafter, it was thoroughly explored at all heating facilities. SEE constitutes a weak noise component [$-(50-90)$ dB] in the spectrum of a PW signal reflected from the ionosphere. It exhibits a complicated structure and occupies a waveband as wide as hundreds of kilohertz. The main spectral components of SEE are generated as a result of conversion of PW-induced plasma (quasielectrostatic) modes into electromagnetic ones. A similar phenomenon, the so-called diagnostic SEE (DSEE) stimulated by short electromagnetic pulses of low average power, injected into ionosphere for sounding the pumped region, was observed at the Zimenki heating facility spaced 30 km apart Nizhny Novgorod [134, 135].

4.1 Spectral structure of stimulated electromagnetic emission

The traditional classification of prominent SEE features regularly present in the spectrum distinguishes: the narrow continuum (NC) in the range of negative frequency shifts from the PW frequency, $\Delta f_{\rm NC} \approx (-40)-0$ kHz (at the maximum powers of the HAARP facility, $\Delta f_{\rm NC}$ can reach -80 kHz); the broadband continuum (BC) in the range of negative frequency shifts $\Delta f_{\rm BC} \sim (-15)-(-100)$ kHz; the downshifted maximum (DM) with a sharp peak at frequency shifts $\Delta f \approx (-7)-(-20)$ kHz and its satellites (2DM, sometimes 3DM and 4DM) at multiple frequency shifts; the upshifted maximum (UM) with $\Delta f \approx +(6-18)$ kHz almost symmetric to DM with respect to f_0; the broad upshifted maximum (BUM) with $\Delta f \approx +(12-200)$ kHz for $f_0 \gtrsim sf_{\rm ce}$, and the broad upshifted structure (BUS) at positive frequency shifts $\Delta f \approx +(12-70)$ kHz at pumping frequencies much higher (by 150–400 kHz) than $sf_{\rm ce}$ [36, 111, 136–138].

At the initial stage, the SEE spectrum contains only the NC component associated with the development of PPI (NC_p or FNC). The NCM appears at the intermediate stage (see Section 2.2, Figs 1–4) against the background of the NC component. Long enough continuous pumping of ionosphere induces the development of striations and AA together with growing the so-called upper-hybrid components of SEE, viz. the DM, its satellites, and the BC; the slightly faster developing UM, and the slower developing BUM. Simultaneously, NC_p and NCM intensities decrease and become inapparent against the background of the DM and BC. The 'thermal' narrowband component, NC_t, also related to the excitation of upper-hybrid waves and the striations predominate at the shifts $\Delta f \approx (-7)-0$ kHz. The development of AA, striations, and SEE upper-hybrid components in the multiple electron gyroresonance region at $f_0 \approx sf_{\rm ce}$ [see paragraph (1) below] is suppressed or markedly slowed down; therefore, the NCM component can be seen in the stationary spectrum.

The overall picture of the f_0-dependence of SEE spectra based on results of systematic measurements at the Sura heating radio facility in 1996–2000 over the entire range of operating frequencies of this facility for the PW–ionosphere interactions altitudes ($\sim 230-250$ km) is presented in Fig. 8 [47, 138]. Examples of stationary SEE spectra taken in the aforementioned regions at different harmonic numbers, $3 < s \leqslant 7$, are given in Fig. 9 [137] (see also Fig. 10 [139]).

In what follows, the main properties of stationary SEE spectra associated with long-term ionosphere pumping and revealed by analyzing their f_0-dependences [36, 50, 111, 136–138] are listed.

(1) The dependence of the SEE spectra shape on the quantity $f_0 - sf_{\rm ce}$ persists at least for $s = 3-7$ at different gyroharmonics numbers s. A change in f_0 between successive harmonics $sf_{\rm ce}$ and $(s+1)f_{\rm ce}$ makes it possible to distinguish five pumping frequency ranges with different SEE spectra: (I) a resonance region, $f_0 \approx sf_{\rm ce}$, where BC and BUS components are absent, while the DM and BUM have a low intensity; (II) the region above the harmonic, $f_0 - sf_{\rm ce} \lesssim 150$ kHz, where the SEE spectrum contains intense DM (frequently 2DM and 3DM) and BUM components; (III) a strong emission region, $f_0 - sf_{\rm ce} \lesssim 400$ kHz, where the SEE spectrum contains high-intensity DM, BC, and BUS components; (IV) a weak emission region, $sf_{\rm ce} + 400$ kHz $\lesssim f_0 \lesssim (s+1)f_{\rm ce} - (50-100)$ kHz, where the BUS disappear, while DM and BC component intensities are significantly decreased; (V) the region under the harmonic, $(s+1)f_{\rm ce} - (50-100)$kH $\lesssim f_0 \lesssim (s+1)f_{\rm ce}$, where the intensities of the DM, its satellites, and/or the BC components increase again.

(2) The DM is the most intense SEE component at all f_0 with the exception of the narrow vicinity of gyroharmonics

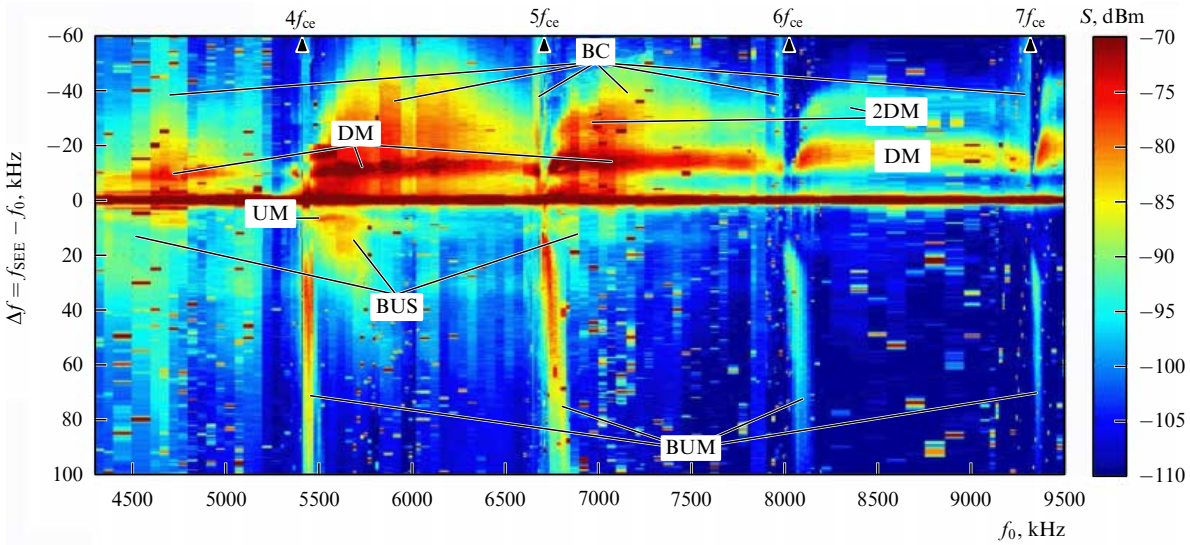

Figure 8. (Color online.) The dependence of an SEE spectrum shape on the PW frequency (4.3 MHz $\leqslant f_0 \leqslant$ 9.5 MHz) deduced from the data from the Sura experiment [47, 138].

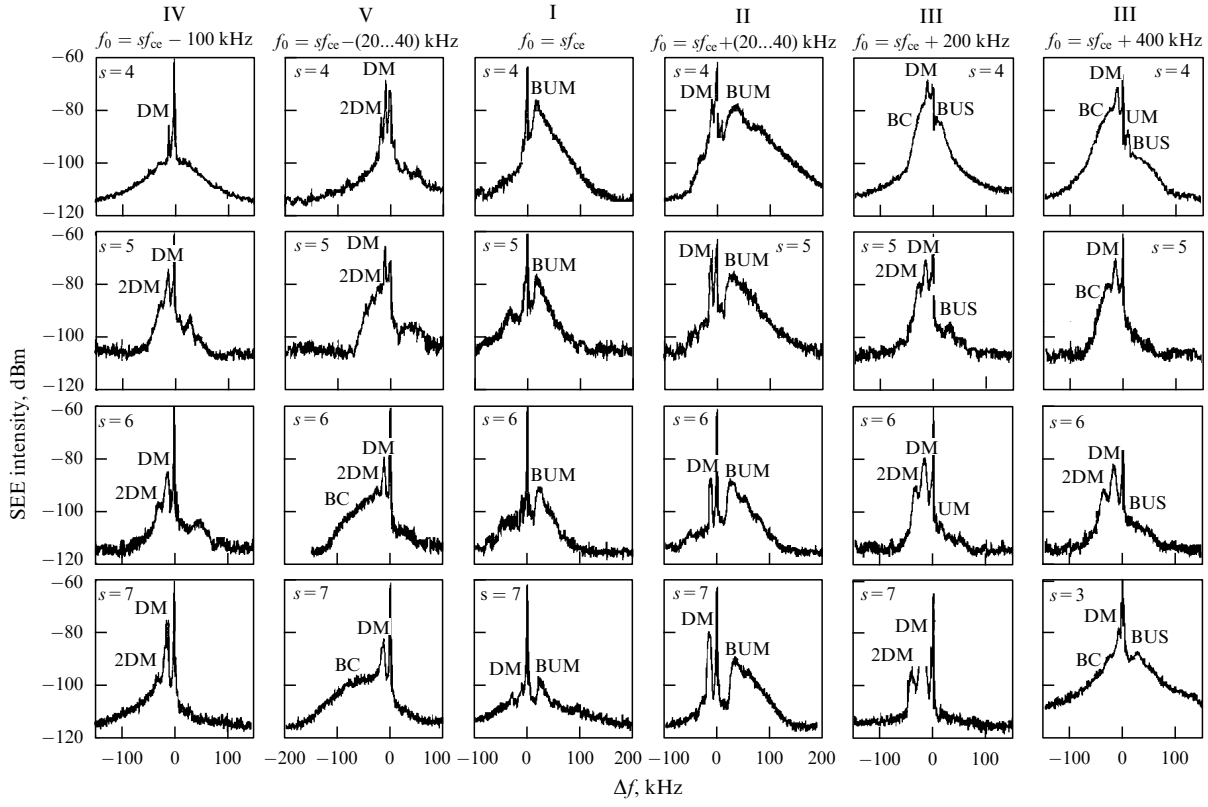

Figure 9. SEE spectra for characteristic PW frequency offsets from electron gyroharmonics $\delta f_c = f_0 - sf_{ce}$ (columns): $\delta f_c \sim -100$ kHz (IV, weak emission), $\delta f_c \sim -(20-40)$ kHz (V, under harmonic), $\delta f_c \simeq 0, f_0 \approx sf_{ce}$ (I, resonance region), $\delta f_c \sim (20-40)$ kHz (II, above harmonic), $\delta f_c \sim 200$ kHz, $\delta f_c \sim 400$ kHz (III, strong emission) for $s = 4-7$ (rows). Bottom right panel shows the spectrum for $f_0 = 4400$ kHz ($s = 3$, region III) [137].

(region I). DM peak frequency shift $|\Delta f_{DM}|$ (like $|\Delta f_{UM}|$) grows linearly with f_0 except resonance regions (I), where the DM approaches the PW. DM intensity in the resonance region falls practically to the noise level in the PW frequency band Δf_{res} that decreases with harmonic number s: the values of Δf_{res} for $s = 4, 5, 6, 7$ in the quiet ionosphere are 6–10, 2–5, 1–2, and 0.2 kHz, respectively [111]. Notice that such Δf_{res} values are close to those obtained in Refs [110, 111] for the width of the bands forbidden for the existence of plasma waves with $\mathbf{k} \perp \mathbf{B}_0$ in the double resonance region of the ionosphere below the F-layer maximum. The shift of the right (high-frequency) flank of the DM remains practically constant ($|\Delta f_{hfDM}| \approx 7-8$ kHz) over the entire f_0 range. This value is close to the lower-hybrid frequency in the F-region of ionosphere, $f_{LH} \approx \sqrt{f_{ce} f_{ci}}$, where f_{ci} is the ion cyclotron frequency, and hf denotes the high-frequency flank.

(3) Intensities of all SEE spectral components are highest for $4f_{ce} < f_0 < 5f_{ce}$. A strong overshoot effect after PW switch-on is responsible for a marked decrease in stationary SEE intensity in the $3f_{ce} < f_0 < 4f_{ce}$ range.

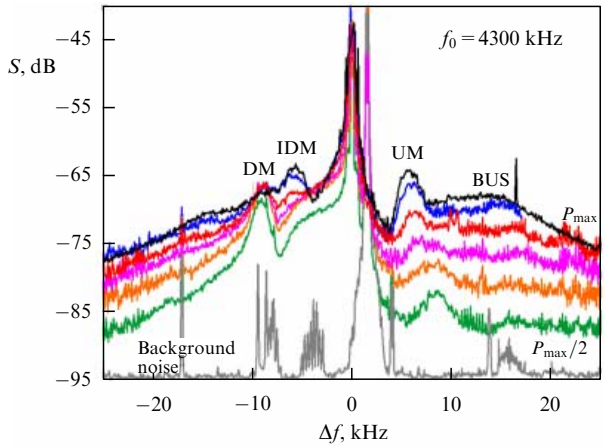

Figure 10. (Color online.) SEE spectra at PW powers $P_{\rm eff}$ doubled from $P_{\max}/32$ to $P_{\max}$, illustrating the emergence of the IDM in the SEE spectrum. Evidently, the IDM dominate the spectrum for $P_{\rm eff} > P_{\max}/4$, $f_0 = 4300$ kHz. Sura facility, 09.08.2008 [139].

(4) The relative contribution of the DM and its satellites (cascade spectrum) to the stationary SEE spectrum increases with the growth of f_0, compared with the continuous BC component in the interharmonic range (regions II–IV). The cascade spectrum prevails fort $s > 5$. In contrast, the BC predominates over the family of DM satellites at higher harmonics, $s > 4$, in the narrow (V) region under the harmonic.

(5) The BUM component is quite apparent in the spectrum for $f_0 \gtrsim sf_{\rm ce}$ (regions I and II). The highest BUM intensity is recorded at the PW frequency directly above the gyroharmonic. The BUM peak position in the spectrum is roughly constant, $\Delta f_{\rm BUM} \sim 15-20$ kHz, for $\delta f_{\rm c} = f_0 - sf_{\rm ce} \lesssim 30$ kHz. The BUM peak moves away from f_0 for $\delta f_{\rm c} \gtrsim 30$ kHz upon f_0 receding from $sf_{\rm ce}$, in accordance with the empirical formula

$$\Delta f_{\rm BUM} \approx f_0 - \left(sf_{\rm ce}(z_{\rm d}) + \delta f\right), \quad \delta f \sim 15-20 \text{ kHz}. \quad (23)$$

Such a dependence of $\Delta f_{\rm BUM}$ on $\delta f_{\rm c}$, as well as the different behavior of the BUM with time after PW switch-on at different $\delta f_{\rm c}$, suggests that the BUM has a two-component structure [140].

The generation of upper-hybrid SEE components is readily explained in terms of a three-step model based on the double transformation of electromagnetic waves (into upper-hybrid waves or the Z-mode and back) on striations with an intermediate stage at which the broadband spectrum of secondary upper-hybrid waves (and Z-mode) is formed at the frequencies shifted relative to the PW under the effect of various ponderomotive nonlinear processes [30, 58, 113, 114, 141–144]. In this scenario, the striations and PlWs play a dual role of the source of PlW ($W_0 n_{\varkappa}^2$) and SEE ($W_\omega n_{\varkappa}^2$) generations and the depressor suppressing the PW and SEE ($\Gamma_{\rm pump}$ and $\Gamma_{\rm SEE}$) in relationships (24)–(26). The spectral intensity S_ω of SEE at the exit $h_{\min}$ from the ionosphere can be presented in the general form as

$$S_\omega(t) \propto \int_{\rm source} W_\omega(h')\, n^2_{\varkappa(h',\omega)}(t) \exp\left\{-\Gamma_{\rm SEE}(h',t)\right\} {\rm d}h', \quad (24)$$

$$W_\omega(h,t) \propto \mathcal{G}(\omega)\, W_0 n^2_{\varkappa(h,\omega_0)}(t) \exp\left\{-\Gamma_{\rm pump}(h,t)\right\}, \quad (25)$$

$$\Gamma_{\rm SEE,\,pump}(h,t) \propto \int_{\rm path} n^2_{\varkappa(h'')}(t)\, {\rm d}h''. \quad (26)$$

Here, W_ω is the spectral energy density of upper-hybrid waves and/or Z-mode, $\Gamma_{\rm SEE}$ is the anomalous absorption of SEE as it propagates downward from the source $h' = h_{\rm m}$ to $h_{\min}$, $\Gamma_{\rm pump}$ is the anomalous attenuation of the PW during its upward propagation from $h_{\min}$ to h' due to SEE and PW scatterings into upper-hybrid waves (Z-mode) on striations, $\mathcal{G}(\omega)$ characterizes the shape of the upper-hybrid wave frequency spectrum formed in ponderomotive processes, and W_0 is the PW energy density at the entry into the perturbed region at $h = h_{\min}$. Integration in formula (24) is over the height interval occupied by the SEE source at a given frequency ω: $h_{\min} < h < h_{\max}$. The $\kappa(h,\omega)$ and $\kappa(h,\omega_0)$ dependences are defined by fulfillment of matching conditions similar to expressions (6) for SEE (and PWs), upper-hybrid waves, and the striations. Then, the $\kappa(h_{\rm mc},\omega)$ dependence accounts for the difference in scales of striations on which the PW is scattered into upper-hybrid waves, and upper-hybrid waves into SEE.

The nonlinear processes responsible for the formation of the PlW frequency spectrum are different for different SEE features. For the BC feature, this is induced scattering from ions [113, 114], and for the DM and its satellites this is three-wave cascade interaction between upper-hybrid and lower-hybrid waves [58, 141]. Formation of upper-hybrid wave spectra for the positive frequency shifts, e.g., the BUS, in the strong emission region is interpreted in terms of conversion of upper-hybrid waves and induced ion-acoustic oscillations with the generation of upper-hybrid waves with a higher frequency [144].

For the BUM, formula (23) suggests an important role of four-wave processes in generating upper-hybrid waves, which were considered in a number of publications [145–147]. Specifically, the decay of two PW quanta into an upper-hybrid wave quantum with $\omega_{\rm UH} > \omega_0 > s\omega_{\rm ce}$ and an electron Bernstein wave quantum with $\omega_{\rm B} \approx s\omega_{\rm ce} < \omega_0$, $2\omega_0 = \omega_{\rm UH} + \omega_{\rm B}$ is considered. The process just as well involves induced low-frequency plasma oscillations with frequencies close to the lower-hybrid frequency [147]. However, the consideration does not include the striations, although a number of experimental evidences are currently available in favor of the validity of the double transformation model for BUM generation (see Section 4.3). As a result, characteristic times of the above four-wave process reported in paper [147] turn out to be much shorter than the observed times of BUM development even in the 'prepared' ionosphere.

An alternative mechanism of upper-hybrid wave generation with $f > f_0$ frequencies, associated with cyclotron instability of electrons accelerated by upper-hybrid waves, was proposed in Ref. [148]. It was shown that, at such PW frequencies, a noticeable transverse anisotropy of the distribution function of accelerated electrons emerges, and its relaxation may give rise to an unstable distribution function with a maximum in transverse velocities (the so-called 'ring distribution'). Such cyclotron instability is invoked, in particular, to interpret 'zebra patterns' in sporadic solar radio bursts [149] and radiowave emission of the ionospheric plasma ('auroral roar emission') associated with the invasion of energetic particle fluxes [150] generated near multiple

electron gyroharmonics. To recall, both mechanisms (four-wave interaction and cyclotron instability) suggest the generation of upper-hybrid waves with $f > f_0 > sf_{ce}$ frequencies. At fixed values of electron number density N_e (and altitude h_{mc}), the matching conditions (6) for SEE generation at higher frequencies ω are, in turn, fulfilled for striations with smaller transverse scales $l_\perp$ [62, 112, 113] (see also Fig. 7); in other words, BUM generation involves striations of smaller scales than DM and BC generations.

The dependence $S_\omega(t)$ of SEE spectral intensity on time in expression (24) is determined by both 'slow time' τ_3 of evolution of the striation spatial spectrum $n^2_\kappa(t)$ [see formula (21)], $\tau_3 \sim 0.5-60$ s, and the fast dynamics of plasma (upper-hybrid) waves and the Z-mode, $\tau_1 \sim 1-10$ ms, $\tau_1 \ll \tau_3$. In the case of a 'cold start', when the PW is incident onto the 'unprepared' ionosphere, the time of AIT evolution is determined according to formula (24) by the development of striations, and PlW energy density $W_\omega(h')$ at each 'slow' time moment can be regarded as stationary and dependent on striation intensity $n^2_\kappa(t)$. Because $\tau_1 \ll \tau_3$, the formation of the spectrum shape $W_\omega \propto \mathcal{G}(\omega)$ and establishment of such a quasistationary state are only possible if $W_\omega(\omega_0)$ slightly exceeds the ponderomotive pumping threshold. When PW is incident onto the ionosphere with a pre-formed striation that did not have time to relax after the preceding switch-off of the quasicontinuously sent PW of duration $\gg \tau_3$ or immediately after its switch-off (bearing in mind the temporal scale $\gtrsim \tau_{rel1}$ comparable to plasma wave decay time), the SEE dynamics must follow the PlW dynamics $W_\omega(h', t)$. All this permits the use of SEE measurements for the elucidation of mechanisms of its generation, PlW damping rates, and diagnostics of AIT parameters (see Section 4.3).

For a rather long time, the approach to SEE interpretation similar to that based on the double transformation mechanism has been explored for the case of strong small-scale irregularities, when upper-hybrid modes happen to be trapped [119, 125, 151, 152]. The authors of Refs [119, 125, 151] considered parametric instabilities of trapped upper-hybrid modes with respect to exciting lower-hybrid waves and the upper-hybrid (UH′) mode at a shifted frequency. It is important to take into account the influence of the trapped modes on SEE properties for a detailed interpretation of experimental data. However, the currently available models need to be further elaborated to address this issue.

Besides the above components regularly present in the SEE spectrum, the downshifted peak (DP) feature with $\Delta f_{DP} \approx -(1-3)$ kHz is registered at PW frequencies $f_0 \approx sf_{ce}$ ($s = 3, 4, 5$). DP intensity decreases with the growing number s. The broad downshifted maximum (BDM) can be obtained at $\Delta f \sim -(15-30)$ kHz shifts with a peak at $\Delta f_{BDM} \sim -(20-25)$ kHz. At $s = 3$, the BDM is more intense and is positioned symmetrically to the BUM in the SEE spectrum with respect to the PW [153, 154].

The most comprehensive description of the spectrum structure of SEE and properties of its components can be found in a review by T B Leyser [36], and in Refs [137, 138, 140, 155].

Recent progress in the development of radio-receiving equipment and enhancement of pumping power (after bringing the HAARP facility to full capacity) have made it possible to discover new SEE spectral features. In the first place, it is the intermediate downshifted maximum (IDM) at $\Delta f_{IDM} \sim -(4-6)$ kHz shifts, located in the SEE spectrum between the PW and DM. Investigations of the IDM properties at the Sura and HAARP heating facilities [139] revealed that its amplitude is higher than that of the DM at PW powers $P_{eff} > 30$ MW in the PW frequency range $f_0 \gtrsim sf_{ce} + 50$ kHz ($s = 2, 3$). At $f_0 \sim 4f_{ce} + 200$ kHz, the IDM is hardly visible in the SEE spectrum, being too small in comparison with NC_t [139].

Secondly, 2011 and 2014 HAARP experiments revealed broad downshifted emission (BDE) (Figs 11, 12) [95]. Figure 12 depicts the well apparent BDM feature for $f_0 > 3f_{ce}$. The BDE is present in the SEE spectrum only at night at a

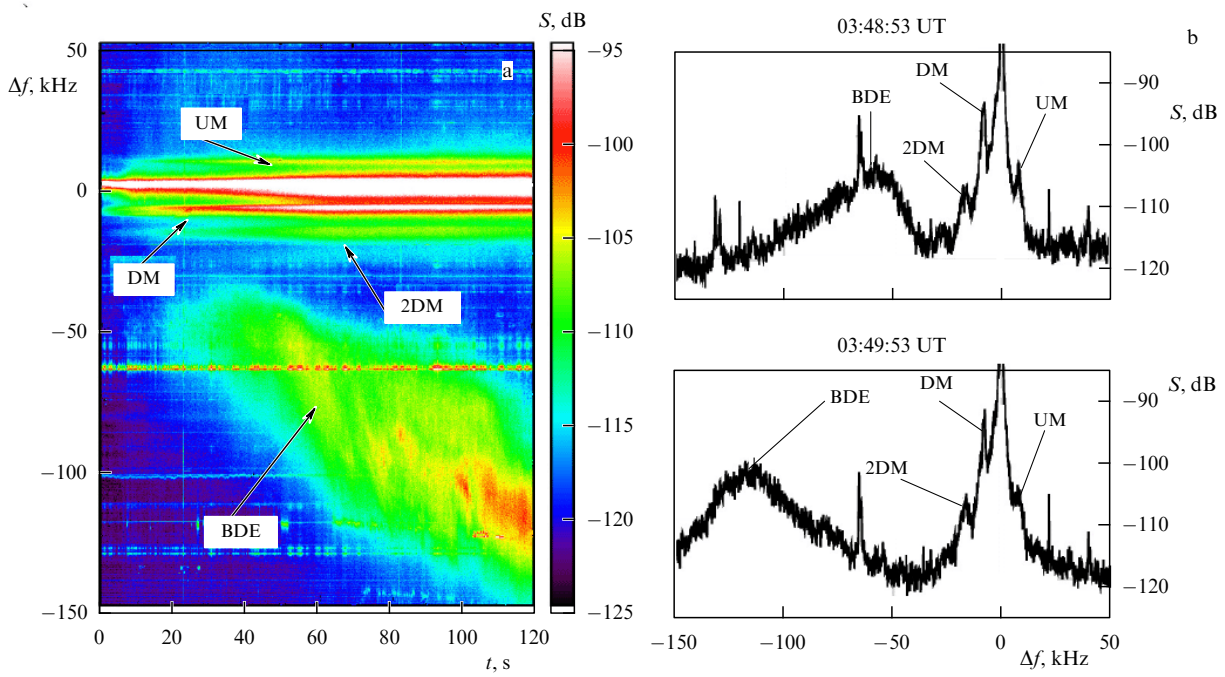

Figure 11. (Color online.) Spectrogram (a) and individual SEE spectra (b) for continuous pumping demonstrating the emergence of the BDE feature. HAARP facility, 27.03.2011, $f_0 = 5700$ kHz. The spectra correspond to the 53rd and 113th s of the spectrogram [95].

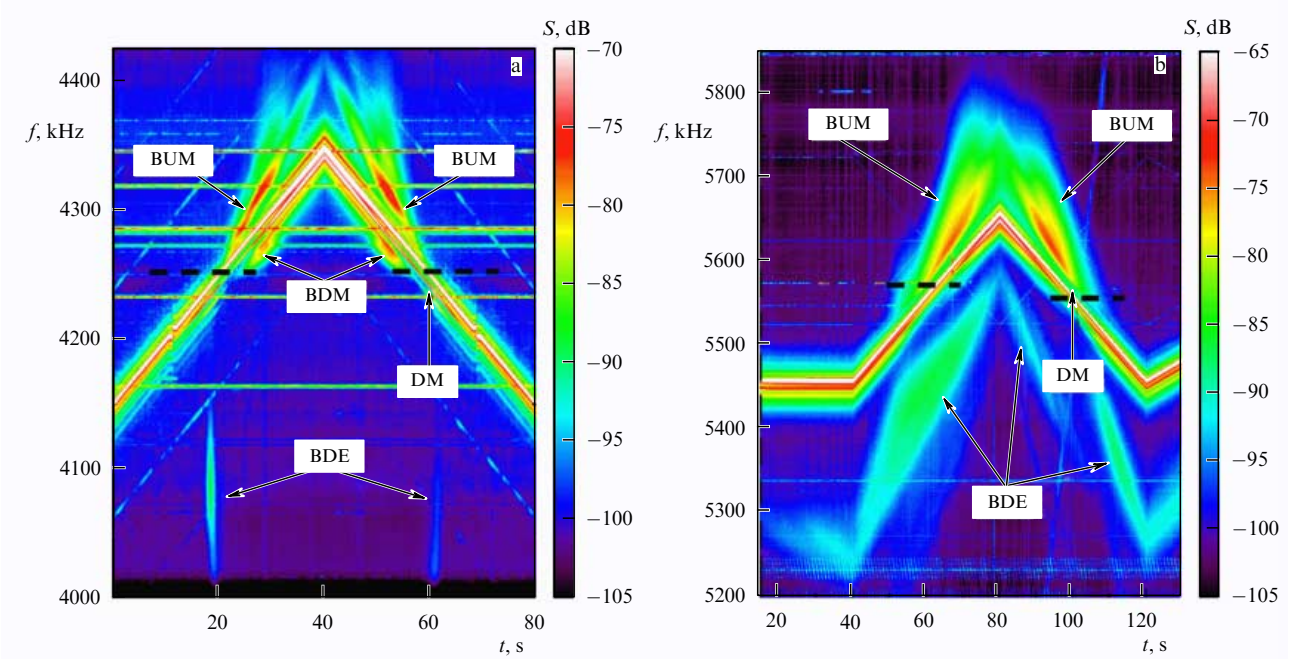

Figure 12. (Color online.) SEE spectrograms obtained by sweeping f_0 in the vicinity of the 3rd (a) and 4th (b) f_{ce} harmonics. The BDE feature of SEE is shown. The BDM feature can be singled out for $f_0 > 3f_{ce}$. Horizontal dashed lines correspond to $f_0 = f_d$. HAARP facility, June 2014 [95].

maximum PW radiation power after long enough heating of the plasma (sometimes a few minutes) and only at maximum intensities of such typical SEE components as the NC and DM. BDE is generated in the PW frequency range in the vicinity of the fourth harmonic of electron cyclotron frequency $4f_{ce} - 100$ kHz $< f_0 < 4f_{ce} + 100$ kHz. The BDE intensity and the width of its spectrum for $f_0 > 4f_{ce}$ are always essentially smaller than those for frequencies $f_0 < 4f_{ce}$, and the BDE occupies the frequency range $\Delta f = -(40-220)$ kHz in the SEE spectrum. The position of BDE intensity maximum in the SEE spectrum displaces closely to the PW frequency when it increases. At $f_0 \sim 3f_{ce}$, BDE is observed in the narrow frequency band of the BH: $3f_{ce} - (15-25)$ kHz $< f_0 < 3f_{ce} - (0-5)$ kHz.

Thirdly, at the maximum power of the HAARP facility and $f_0 = 2.85$ kHz $\approx 2f_{ce}$, the SEE spectrum contains in the region of the frequency shifts, $-0.80 < \Delta f < 0.35$ kHz, a sequence of equidistant peaks separated from each other by an ion cyclotron frequency f_{ci} [97], which confirms excitation of ion Bernstein modes in the course of ionospheric modification.

Finally, the HAARP [56, 57, 98] and EISCAT [156] experiments revealed narrow spectral SEE peaks with $\Delta f \approx \pm(8-12)$ Hz detunings and their weak satellites with $\Delta f \approx \pm(24-26)$ Hz appearing upon pumping into the magnetic zenith (along the magnetic field), as well as peaks at $\Delta f \approx \pm(23-30)$ Hz associated with vertical PW emission (the shift magnitude $|\Delta f|$ increased with the growth of f_0), and peaks with $\Delta f \approx \pm f_{ci}$ detunings. The appearance of the narrowband peaks is interpreted as stimulated Brillouin scattering (SBS) of the PW by ion-acoustic waves for the case of fulfilled matching conditions

$$\mathbf{k}_s = \mathbf{k}_0 \pm \mathbf{k}_a\,, \quad \omega_s = \omega_0 \pm \omega_a\,. \tag{27}$$

Here, the subscript 's' stands for the scattered electromagnetic wave, and 'a' for ion-acoustic waves whose frequencies for $k_0 V_a \ll \omega_{ci}$ equal $\omega_{a1} = k_a V_s |\cos\alpha|$ (slow magneto-acoustic wave, with $V_a = (2T_e/m_i)^{1/2}$ being its velocity) and $\omega_{a2} = \omega_{ci}$ (the cyclotron-acoustic wave). The discovery of SBS was anticipated in the very first ionosphere modification experiments, but scattered signals were reliably recorded only in recent years. It is worthwhile to note that the occurrence of SBS does not require the artificial turbulence in the disturbed ionospheric region to exist, because plasma waves and density irregularities do not play any role in the scattering mechanism. According to Ref. [98], the development of upper-hybrid turbulence (appearance of the DM in the SEE spectrum) leads to suppressing SBS signals. At the same time, there are no reports in the literature suggesting the existence of the SBS for a pump wave with X-polarization.

4.2 Behavior of stimulated electromagnetic emission in the vicinity of multiple electron gyroresonances

It follows from Figs 8, 9 that SEE spectra greatly depend on the ratio of PW frequency f_0 to electron gyroharmonic frequency sf_{ce}. The SEE spectrum is altered most significantly when f_0 changes are relatively small (sometimes hundreds of hertz) upon transition from region (V) beneath the harmonic through resonance region (I), where $f_0 \approx sf_{ce}$, into region (II) above the harmonic (Figs 13, 14). The electron cyclotron frequency is $f_{ce} \sim 1.3-1.4$ MHz at auroral (HAARP and EISCAT) and middle (Sura) latitudes; it decreases with altitude h at $\mathrm{d}f_{ce}/\mathrm{d}h \sim -(0.60-0.65)$ kHz km^{-1}. Vertical movements and horizontal displacement of large-scale irregularities of electron density through the disturbed ionospheric region, e.g., passage of acoustic-gravity waves, can considerably alter both altitude h_d and frequency f_d of double resonance: $f_d = f_{UH}(h_d) = nf_{ce}(h_d)$ in the course of experiment and thereby affect the observed dependences of SEE spectra on the f_0 to sf_{ce} ratio in the resonance region. Therefore, the total measuring time must be rather short:

$$\Delta t < \frac{\Delta f_{res}}{s}\left|\frac{\mathrm{d}f_{ce}}{\mathrm{d}h}\right| v\,.$$

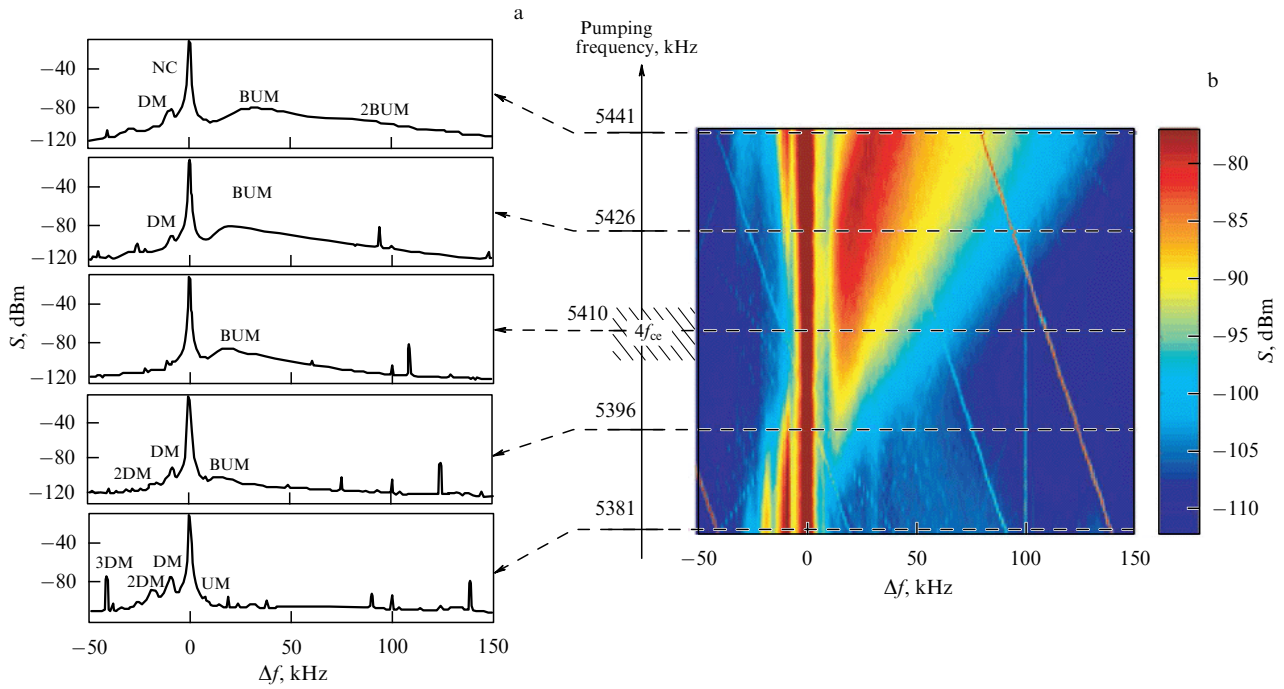

Figure 13. (Color online.) (a) Individual SEE spectra for five different values of f_0 shown in figure (b) by dashed lines. (b) SEE spectrogram obtained by sweeping the PW frequency f_0 in the vicinity of the fourth gyroharmonic. Sura facility, September 1998 [50].

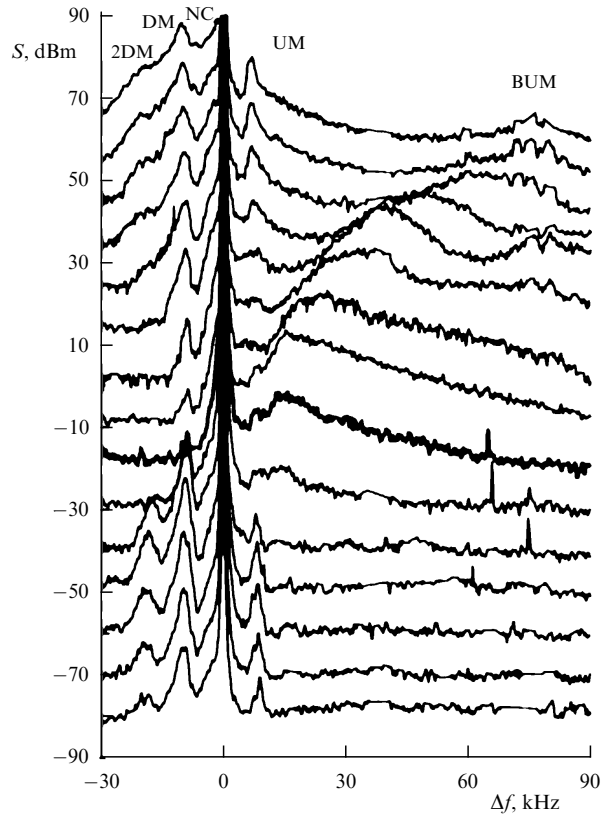

Figure 14. Sample of SEE spectra obtained by sweeping the PW frequency f_0 through the fourth electron gyroharmonic $4f_{ce}$, shown with a frequency step of 10 kHz, 5360 kHz $\leqslant f_0 \leqslant$ 5500 kHz. For clarity, every next spectrum is upshifted by 10 dB along the axis of ordinates. The bold line marks the spectrum at $f_0 = 5420$ kHz $\approx f_{0\overline{\mathrm{DM}}}$. Sura facility, May 2004 [92].

Here, v is the characteristic velocity of the vertical displacement of the ionosphere (the altitude of a certain fixed density of the ionospheric plasma). Based on the estimates of $\Delta f_{\mathrm{res}} \sim 2$ and 6 kHz for $n = 5$ and 4 harmonic numbers, reported in Ref. [111] (see Section 4.1), it can be argued that the measuring time in the region of the most pronounced changes in SEE properties at $f_0 \sim f_{\mathrm{d}}$ for displacement velocities $v \sim 2-5$ m s^{-1} (under unperturbed ionospheric conditions) cannot be longer than $t \sim 5-15$ min.

To reduce to a minimum the influence of variations of ionospheric conditions on evaluating the $f_0 - sf_{ce}$ dependence of SEE spectra, a technique of fast sweeping (stepping) of the PW frequency in the gyroharmonic range during the quasistationary state time was elaborated. Detailed results of experiments carried out by this method at the Sura heating facility for $s = 4, 5$ are discussed in Refs [50, 58, 92]. A series of HAARP experiments for $s = 2, 3, 4$ is reported in Refs [143, 157]. The full range of f_0 variations around sf_{ce} spanned $\Delta f_0 = 60-80$ kHz with a step of 1 kHz and pumping duration at a fixed frequency lasted 0.2 s $\gg \tau_1$. This means that the SEE spectrum had enough time to evolve to the stationary one after each frequency step. Moreover, the sweeping was preceded by long-term ($\sim$ 1 min) pumping at a fixed frequency for creating the striations. It can be then assumed that the striation intensity and the spatial spectrum changed but insignificantly during the entire sweeping time. The spectrograms and individual SEE spectra obtained in the Sura experiments of 1998 and 2004 are presented in Figs 13, 14, demonstrating their rather abrupt changes during the passage through gyroharmonics.

Such dependence of the shape of the SEE spectra on the f_0/sf_{ce} ratio can be used to determine this ratio with a high degree of accuracy. Figure 15 demonstrates f_0 dependences of integral intensities of some spectral components of SEE (DM, 2DM, NC, UM, and BUM) obtained by sweeping the f_0 near the fourth gyroharmonic.

It follows from Figs 14, 15 that the DM component has its lowest intensity at the PW frequency $f_0 = f_{0\overline{\mathrm{DM}}}$ and is virtually absent in the SEE spectrum. At the minimum PW sweeping frequency $f_0 \approx f_{0\overline{\mathrm{DM}}} - 40$ kHz, the SEE spectrum

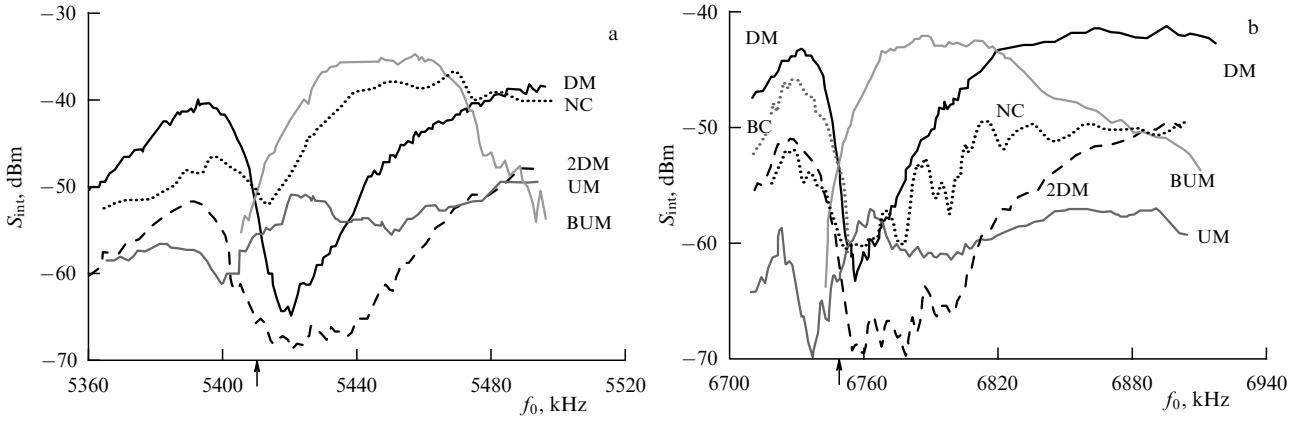

Figure 15. Dependence of the integral intensity of SEE spectral components on the PW frequency in sweeping the f_0 in the $4f_{ce}$ region (a, 19.05.2004) and the $5f_{ce}$ region (b, 15.09. 2004). Sura facility. Arrows indicate PW frequency values $f_0 = f_{0,\min} = 4f_{ce}(h_d)$ (a) and $f_0 = f_{0,\min} = 5f_{ce}(h_d)$ (b) [92].

exhibits an intense DM component with a peak at $\Delta f_{DM} = f_{DM} - f_0 \approx -9$ kHz, as well as a 2DM component with a peak at $\Delta f_{2DM} \approx -17.5$ kHz, UM component with a peak at $\Delta f_{UM} \approx 7.5-8$ kHz, and NC component at the frequency shifts $-6.5 \lesssim \Delta f \lesssim -2.0$ kHz with a maximum intensity at the frequencies close to f_0. The intensity of these features increases as f_0 grows and approaches $f_{0\overline{DM}}$ and, in conformity with formula (17), $4f_{ce}$. It reaches maximum values first for the UM and then (almost simultaneously) for the 2DM, DM, and NC (transition from the weak emission region (IV) into the region under the harmonic). As f_0 grows further, the intensity of all these components decreases to their minimum values. For components with $\Delta f < 0$ (DM, 2DM, and NC), the fall begins from the left (low-frequency) part of the spectrum, while its right (high-frequency) part remains virtually unaltered. As a result, the positions of DM and 2DM peaks become closer to f_0 by 0.5–1 kHz. The minimum intensity is first reached for the UM component at $f_0 = f_{0\overline{UM}} = f_{\overline{UM}} - \Delta f_{\overline{UM}}$. Then, at $f_0 = f_{0,\min}$, the integral intensity minimum of all components is reached. Further, at $f_0 = f_{0\overline{NC}} = f_{\overline{NC}} + 2$ kHz, the integral intensity minimum of the NC component is observed. Finally, the minimum intensity of the DM component occurs at $f_0 = f_{0\overline{DM}} = f_{\overline{DM}} - \Delta f_{DM}$, with this component being practically indistinguishable in the spectrum.

SEE frequencies in the ranges of UM and DM peaks and at the HF edge of the component NC in the course of their maximum suppression ($f_{\overline{UM}}$, $f_{\overline{DM}}$, and $f_{\overline{NC}}$) become practically equal to the frequency at which the integral intensity minimum of SEE, $f_0 = f_{0,\min}$, is passed. It can be conjectured that it is this frequency that comes into the double resonance, i.e., coincides simultaneously with the sth harmonic of the electron cyclotron frequency and the upper-hybrid frequency in the region of interaction between the pump wave and the ionospheric plasma:

$$f_d = 4f_{ce}(h_d) \approx f_{\overline{UM}} \approx f_{0,\min} \approx f_{\overline{NC}} \approx f_{\overline{DM}}\,. \qquad (28)$$

The PW frequency range near $f_{0\overline{DM}}$, within which DM intensity is nothing more than by 1 dB exceeds the noise level in the radio receiving equipment, spans 6–7 kHz, in agreement with the measured value [111] during long-term continuous pumping under unperturbed ionospheric conditions. The frequency range in which the 2DM component is suppressed appears to be wider ($\sim$ 30 kHz) and markedly shifted toward the high-frequency region with respect to $f_{0\overline{DM}}$.

With a rise in f_0, the BUM component begins to be noticeable for $f_0 \gtrsim f_{0\overline{UM}}$ frequencies, almost immediately after passing the UM intensity minimum. This frequency proves to be lower than the PW frequency at a DM minimum, i.e., for $f_0 < f_{0\overline{DM}}$. At the same time, because $\Delta f_{UM} < \Delta f_{BUM}$, the frequencies of BUM itself are always higher, in accordance with formula (28), than the double resonance frequency: $f_{BUM} = f_0 + \Delta f_{BUM} > f_d$.

The changes in the SEE spectrum described in the preceding paragraphs occur at virtually insignificant (only by 10–20 kHz) changes in f_0. Such a behavior of the SEE spectrum as f_0 passes through $4f_{ce}$ is analogous to that observed in other experiments carried out under unperturbed ionospheric conditions at $s = 4$ and $s = 5$ [50, 58, 92]. A HAARP experiment with $s = 3$ also revealed successive suppression of UM and DM components. Naturally, different f_d and h_d values were registered in different experiments and under different ionospheric conditions.

Taken together, the experimentally found f_d value, formula (28), and consideration of the existing geomagnetic field models make it possible to accurately determine the double resonance altitude h_d and concentration of the ionospheric plasma in the region of its interaction with the pump wave. For example, in the experiments referred to in Fig. 15, the values of $f_d \approx sf_{ce}(h_d) \approx f_{UH}(h_d)$ ranged 5410–5412 kHz for $s = 4$, and 6747–6750 kHz for $s = 5$, meaning that $f_{ce}(h_d)$ is 1352.5–1353.0 and 1349.4 –1350.0 kHz, respectively. In the International Geomagnetic Reference Field (IGRF) model, such f_{ce} values to be recorded by the Sura heating facility must occur at altitudes of 217–218 and 220–221 km above Earth's surface. Electron number density N_e at such altitudes is easy to calculate using expressions for upper-hybrid and plasma frequencies:

$$\begin{aligned} &s = 4, \quad f_{pe}(h_d) = \left(f_d^2 - f_{ce}^2(h_d)\right)^{1/2} \approx 5238-5240 \text{ kHz!}\,,\\ &\qquad N_e = \pi f_{pe}^2 \frac{m_e}{e^2} \approx (3.405-3.407)\times 10^5 \text{ cm}^{-3}\,,\\ &s = 5, \quad f_{pe}(h_d) \approx 6611-6613 \text{ kHz}\,,\\ &\qquad N_e \approx (5.423-5.427)\times 10^5 \text{ cm}^{-3}\,. \end{aligned} \qquad (29)$$

It can be concluded that such experiments allow the evaluation of the electron cyclotron frequency, induction of the geomagnetic field, and plasma frequency at altitude h_d to

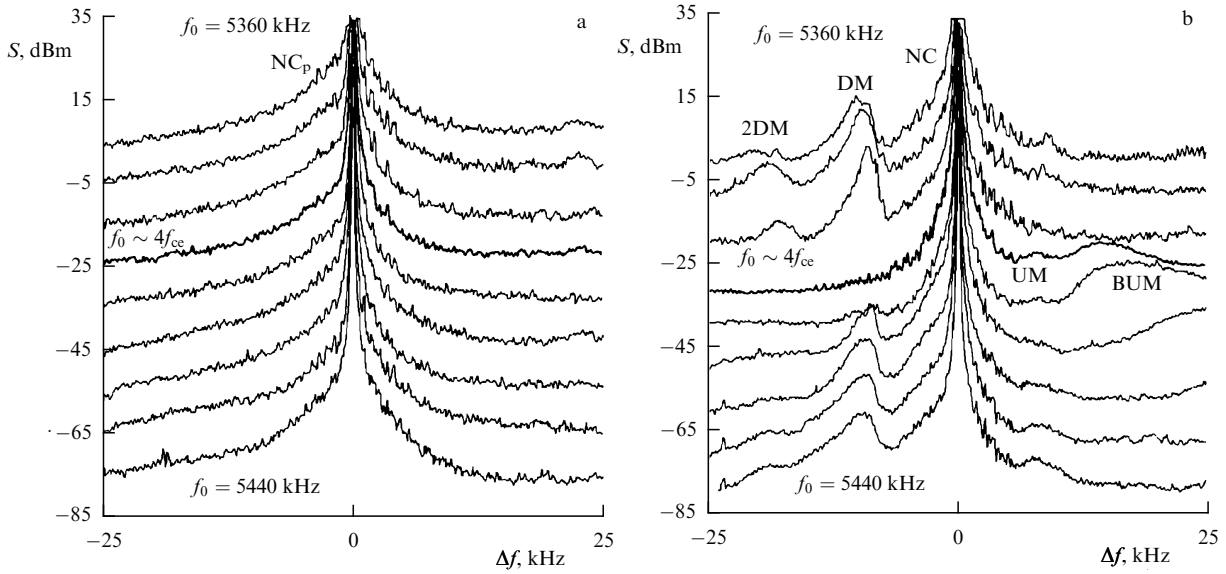

Figure 16. SEE spectra obtained by pumping the ionosphere at frequencies $f_0 \sim 4f_{ce}$ ($5360 \leqslant f_0 \leqslant 5440$ kHz) during formation of Langmuir (a) and upper-hybrid (b) plasma turbulences. The spectra are presented with a 10-dB shift and a PW frequency step of 10 kHz. Sura facility, 21.03.2004 [92].

within 0.05%, and electron concentration with an accuracy of order 0.1%. The accuracy of measuring of the double resonance altitude can be as high as 0.5–1 km or much higher than the accuracy of the most sophisticated modern ionozonds.

Figure 16 illustrates SEE spectra obtained by irradiation of the ionosphere with short pulses ($\tau = 30$ ms $\ll \tau_3$) having the repetition period $T = 1$ s (Fig. 16a), and by prolonged (1 min) continuous pumping at the frequency $f_0 \sim 4f_{ce}$ (Fig. 16b). Pulsed pumping by itself, in the absence of durable pumping, does not lead to the generation and maintenance of upper-hybrid plasma turbulence associated with a striation excitation because of the small pulse length and average pump power [85, 87] (see Sections 2, 3). The SEE spectrum only contains the narrow-band component NC_p related to excitation of plasma turbulence as a result of PPI development near the PW reflection level where it is polarized along the magnetic field $\mathbf{B}_0$. The proximity of f_0 to sf_{ce} must not affect the properties of such waves and, therefore, SEE spectra (NC_p components). The absence of such a dependence is quite apparent in Fig. 16a, while Fig. 16b demonstrates the dependence of SEE spectra on the f_0-to-$4f_{ce}$ ratio that is typical of regions (V) (upper spectra) and (I), (II), and (III) (lower spectra) and emerges in the case of prolonged impact.

To study separately the influence of striations and ponderomotive interaction between upper-hybrid waves on SEE spectra, additional heating was employed to create irregularities by a pump wave with a frequency far from multiple gyroresonance in the PW UHR region, where $f_0 \approx f_{UH} = (f_{pe}^2 + f_{ce}^2)^{1/2}$, and SEE was generated by a pulsed diagnostic wave of small average power. The longitudinal (along the magnetic field) size of striations was sufficiently large: $l_\parallel \sim 5-30$ km. At small angles of the geomagnetic field with respect to the vertical ($\alpha_I = 12°$, 14°, and 18.5° for the EISCAT, HAARP, and Sura facilities, respectively), this size roughly corresponds to the altitudinal size of the disturbed ionospheric region and is commensurate with the thickness of an ionospheric layer. In this case, diagnostic SEE results from upper-hybrid wave excitation due to the scattering of a diagnostic wave with frequency f_{DW} from the striations near the level of its upper-hybrid resonance, where $f_{DW} \approx f_{UH}$ (see paper [58, 92] for more details). The altitude of the diagnostic wave UHR region (and wave frequency f_{DW}) can be significantly different from the PW UHR altitude (and f_0 frequency). It makes possible the exploration of upper-hybrid turbulence near multiple cyclotron resonance with the aid of diagnostic SEE at frequencies $f_{DW} \sim sf_{ce}$ [30].

The family of diagnostic SEE spectra at different diagnostic wave frequencies in the vicinity of $f_{DW} \approx 4f_{ce}$, $4f_{ce} \approx 5385$– 5390 kHz, is presented in Fig. 17. Clearly, the dependence of diagnostic SEE spectra on the f_{DW}-to-$4f_{ce}$ ratio in the presence of the striations created by external pumping resembles the behavior of SEE spectra as a function of f_0 during the f_0 sweeping through $4f_{ce}$.

A detailed description of the behavior of different SEE spectral components upon a fast sweeping of the PW frequency f_0 in the vicinity of multiple cyclotron resonances sf_{ce} and a thorough analysis of nonlinear processes responsible for the formation of SEE spectra in regions (V), (I), and (II) (see Refs [50, 58, 92]) are beyond the scope of the present review. Only a few inferences based on results of such analysis are cited below.

(1) Formation of intense striations in the case of prolonged pumping of the ionosphere is due to the fact of generation of stimulated electromagnetic emission in the PW UHR region and markedly affects SEE intensity. The shape of the spectrum of upper-hybrid SEE components and their practically total suppression upon passing the PW frequency f_0 through gyroharmonics sf_{ce} are, in turn, determined by dispersion properties and the character of interaction between HF plasma modes, as well as by the proximity of their frequencies to the gyroharmonics. The dependence of the shape of the SEE spectrum on the f_0/sf_{ce} ratio disappears in short-pulse irradiation in which striations have no time to form and SEE is determined by the ponderomotive interaction between PW and Langmuir waves propagating almost parallel to the geomagnetic field.

(2) Suppression of different SEE spectral components upon the passage of the PW frequency f_0 through the

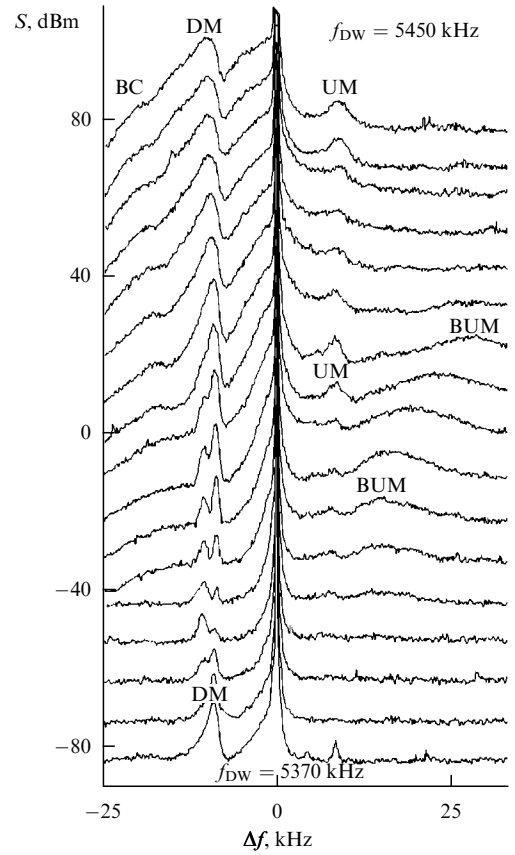

Figure 17. Diagnostic SEE spectra obtained by probing the ionospheric plasma with diagnostic pulses with the carrier frequencies $5370 \leqslant f_{DW} \leqslant 5450$ kHz near $4f_{ce}$ and additional heating at the frequency $f_0 = 5620$ kHz. The spectra are presented with a 10-dB shift and a diagnostic wave frequency step of 5 kHz. Sura facility, 26.05.2004 [92].

gyroharmonic occurs at one and the same frequency of these components coincident with the PW frequency $f_{0,\min}$ at which the integral intensity of all SEE components is minimal, and with the double resonance frequency. Due to this, the existing geomagnetic field models can be used to determine with a high accuracy magnetic induction, plasma concentration, and double resonance altitude h_d.

(3) The most likely mechanism behind the generation of upper-hybrid components of SEE in the region of gyroharmonics (NC_t, DM, 2DM, UM) is the double transformation of electromagnetic waves (into plasma waves and back) on striations with an intermediate stage at which the PlW spectrum forms due to the processes of interaction among HF plasma waves, e.g., induced scattering or decay interaction with the involvement of lower-hybrid waves. At the same time, an important role in the formation of the spectrum of plasma waves responsible for DM component generation is played, at $f_0 \approx f_{0,\min} \approx f_d$, by a direct PW decay into upper- and lower-hybrid waves.

(4) As f_0 increases, the BUM component generation becomes apparent at frequencies higher than the frequency at which UM component undergoes suppression: $f_0 \gtrsim f_{0\,\overline{UM}} \approx f_d - \Delta f_{UM}$, almost immediately after the passage through the UM intensity minimum. At the same time, because always $\Delta f_{0\,UM} < \Delta f_{BUM}$, the frequencies of the BUM itself become higher than the double resonance frequency: $f_{BUM} = f_0 + \Delta f_{BUM} > f_d$. The most probable mechanism of the BUM component generation is the transformation (scattering) of upper-hybrid waves having frequencies higher than f_d on striations. Generation of this component at high enough values of $f_0 - sf_{ce}$ ($f_{BUM} - f_0 \approx f_0 - (sf_{ce}(h_d) + \Delta f)$, $\Delta f \sim 15-20$ kHz takes place much below the double resonance altitude h_d.

4.3 Research on plasma turbulence dynamics with the use of diagnostic SEE

4.3.1 Influence of striations' dynamics on SEE dynamics. The very first experiments in which diagnostic SEE dynamics [134] and SEE itself (rather its BC component) [158] were investigated demonstrated that the characteristic times of SEE evolution are similar to the times of development of aspect scattering, anomalous absorption, and, consequently, striations. This observation motivated elaboration of the diagnostic schedule with alternation of prolonged pumping and short pulses (20–30 ms) having a large repetition period (1–3 s) for the evaluation of the influence of striations with various scales and different relaxation times $\tau_{rel}(\kappa)$ [see formula (22)] on SEE generation. Furthermore, this observation facilitated construction of the theoretical BC model in the framework of the double transformation scheme [113, 134]. Formation of the spectrum W_ω of plasma waves for BC generation is a result of their induced scattering from thermal ions, which enables derivation of the simple analytical expression for W_ω [113] and simulation of SEE dynamics in the framework of the double transformation scheme [formulas (24)–(26)] with the help of the empirical model (21) [30, 114, 131].

Figure 18 presents a typical example of BC temporal evolution for five different frequency shifts $\Delta f = f - f_0$ (bold lines with a noise track). The time of the BC amplitude growth is 1–1.5 s, and the overshoot effect is very apparent: roughly 1.5–2 s after PW switch-on ($t = 0$), the BC amplitude begins to diminish; it increases again after PW transfer from the continuous pumping regime to the diagnostic pulse regime at $t = t_0$, reaches a maximum for ~ 5–15 s, and thereafter relaxes. Numerous experiments [25, 35, 36, 45, 158, 159] have shown that typical BC growth times and times of the first overshoot vary from 0.5 to 40 s, depending on the PW power, ionospheric conditions, and time of day.

The results of modeling the BC component [formulas (21), (22), (24)–(26)] are given in Fig. 18 by thin smooth lines [114]. The quantity $L = |\partial\varepsilon/\partial z|^{-1}$ obtained from the analysis of ionograms recorded during experiments and the real value of pump power P_{eff} were used for the purpose. To correlate the observed and theoretical values of SEE intensity, they were assumed to be equal at $t = t_0 = 60$ s and $\Delta f = -55$ kHz. The region of excellent agreement between experimental and simulated values in the 3D parameter space $\{\Delta n_0^2, p, \alpha_{is}\}$ [Δn_0^2 is the integral striation intensity, p is the striation 2D spatial spectrum index (see function $\Phi_\perp$ ($\kappa_\perp$) in formula (21) and the accompanying text), and α_{is} is the coefficient determining the induced scattering rate] appears to be rather narrow (around 10% for each parameter). Greater changes result in marked deterioration of the quantitative agreement in different panels of Fig. 18 (in terms of frequency and time) and the appearance of certain unobservable qualitative features.

The indisputable agreement between model calculations and results of measurements makes it possible to interpret the main features of the SEE BC component behavior: characteristic growth times, the SEE energy flux on Earth's surface, the BC stationary spectrum, overshoot effects and their characteristics in the course of continuous pumping (at the

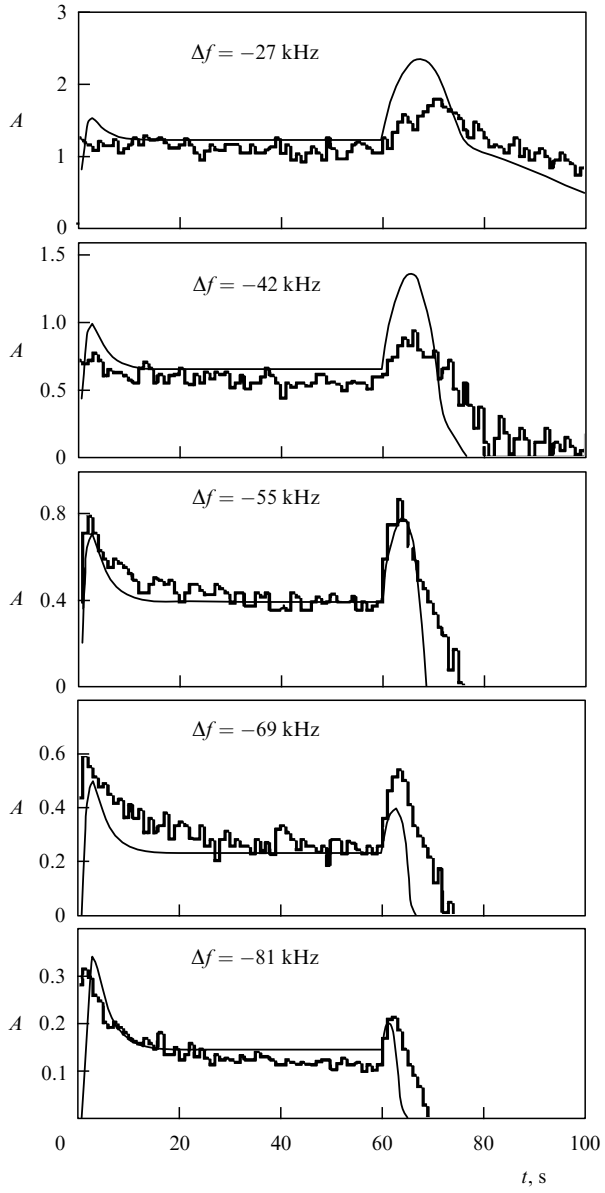

Figure 18. Dynamics of the SEE amplitude for different frequency shifts Δf. Bold lines with a noise track show results of Sura measurements ($f_0 = 5828$ kHz, 23.04.91). Thin smooth lines denote results of numerical simulation. PW transition to the pulsed regime ($\tau_p = 20$ ms, $T = 1$ s) takes place at $t_0 = 60$ s [114].

striation formation stage) and after switching from continuous to diagnostic pulse pumping (at the striation relaxation stage), and characteristic times of SEE relaxation from pulse to pulse in the diagnostic schedule after reaching the intensity maximum. In other words, the combination of numerical simulation and SEE measurements makes it possible to diagnose the properties of the thermal parametric turbulence area that forms in the F-region ionosphere under the influence of a pump wave, viz. striation scales $l_\perp$ responsible for SEE generation and anomalous absorption at different stages of the ionospheric pumping, striation spatial spectrum index p and width, Δn^2 intensity, etc. Variation of parameters of the empirical model permits us to describe the majority of the observed peculiarities of striation-related SEE dynamics. References [30, 54, 114, 131, 142, 160] report the results of detailed experimental studies of slow SEE dynamics in alternating and two-frequency pumping at various PW frequencies (including those close to gyroharmonics) and powers, times of day for different SEE features at the negative frequency shifts, and their comparison with the results of respective simulations.

Unfortunately, it proved impossible to derive a simple analytical expression for the spectrum W_ω of plasma waves and perform full-scale simulation for any SEE feature but the BC. As far as the DM, BUM, and other features are concerned, especially at $f_0 \sim sf_{ce}$, one has to confine oneself to a qualitative analysis or employ a rather crude empirical model of SEE dynamics [53, 131, 142] that obeys the following expression at the diagnostic probing stage $t > t_0$:

$$S(t) = S_s \exp\left(-\frac{t-t_0}{\tau_s}\right) \exp\left(-S_D \exp\frac{t-t_0}{\tau_D}\right),$$
$$S_D = \ln\frac{S_s}{S_{st}}. \qquad (30)$$

Here, S, S_s, S_D, and S_{st} characterize emission intensity, emission source intensity, emission depressor intensity, and stationary intensity, respectively, and τ_s and τ_D stand for the relaxation times of the striations, playing the role of the source and the depressor, respectively: $\tau_s > \tau_D$. The authors of Ref. [54] estimated τ_s and τ_D values from the behavior of DM and BUM features at $f_0 \sim 5f_{ce}$ and compared them with the striation relaxation time. It was shown that DM generation is related to striations having the lateral size $7 \lesssim l_\perp \lesssim 30$ m, and BUM generation to a smaller-scale striation: $l_\perp \lesssim 3-5$ m. The $z_{mc}(\omega, \kappa)$ dependence can be invoked to estimate the altitude and extension of the SEE source region.

A qualitative comparison of spectral characteristics and dynamics of the DM, BC, and 'new' IDM components (see Fig. 10) at the diagnostic probing stage revealed that IDM generation involves the smaller-scale striations ($l_\perp < 6$ m); this means that it occurs at a lower altitude than BC and DM generations. Moreover, the formation of the spectrum of plasma waves responsible for IDM generation must be mediated through a mechanism other than that underlying DM generation, because $|\Delta f_{IDM}| < f_{LH} \leqslant |\Delta f_{DM}|$. The IDM, unlike the BC, looks as a distinguished narrow spectral peak. It was therefore hypothesized in Ref. [139] that the IDM is generated as a consequence of double PW transformation on the striations, with the SEE proper resulting from the scattering of upper-hybrid waves (UH_{IDM}) by the small-scale part of the striation spectrum near the lower border of AIT existence. Upper-hybrid IDM waves, in turn, appear in the PlW spectrum as a result of induced upper-hybrid wave scattering by thermal ions at the PW frequency or by drift oscillations of the walls of small-scale striations. The latter mechanism was considered in the context of interpretation of SEE modeling under conditions of laboratory experiments [161].

Notice two peculiarities of BUM spectrum dynamics in the case of a 'cold start' (Fig. 19). First, the BUM component develops much more slowly than the DM or BC, which suggests, together with its faster relaxation after transition to the diagnostic pulse pumping, a contribution of the smaller-scale part of the striation spectrum to BUM generation, because these irregularities grow more slowly upon TPI excitation (Fig. 6) and relax faster due to diffuse spreading [see formula (22)]. Second, the BUM peak position in the SEE spectrum approaches the PW in the course of time (19) [155, 162]. This fact, as well as the shift of the frequency peak δf in empirical formula (23), can be interpreted as a rise in the

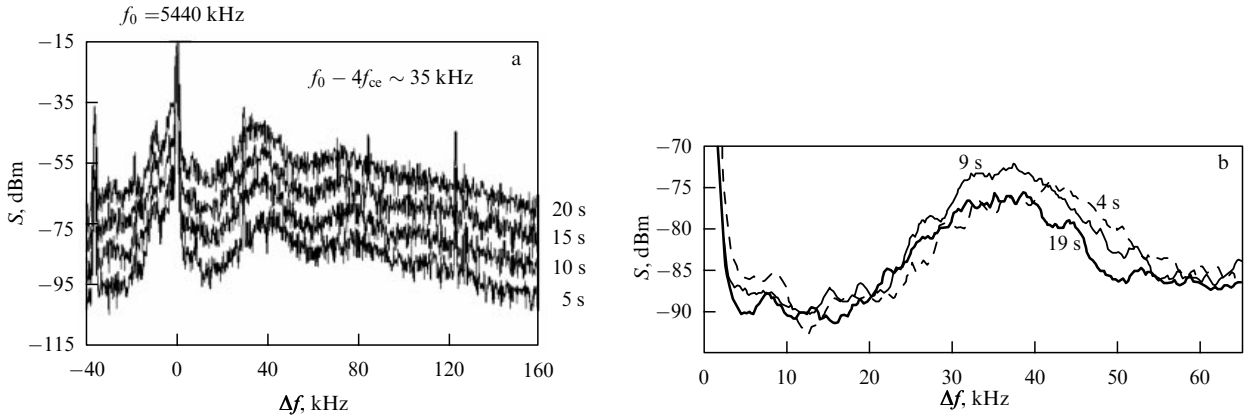

Figure 19. (a) The family of SEE spectra for $f_0 = 5440$ kHz $> 4f_{ce}$ (Sura facility, 21.05.03); the right ordinate axis marks spectrum registration time after PW switch-on; registration time of a single spectrum is 4 s. (b) A fragment of the same family of SEE spectra after the current averaging over time, illustrating BUM temporal evolution. The BUM peak is seen to be shifted toward the pump wave with a subsequent decrease in its intensity (overshoot) [155].

multiple electron cyclotron frequency by δf with respect to $sf_{ce}(z_d)$ at the double resonance altitude z_d or, in other words, as a downward shift of the BUM component generation region relative the double resonance level [58, 92]. Such a shift for the fourth and fifth gyroharmonics in the IGRF geomagnetic field model amounts to $\Delta h \sim \delta f |(\partial f_{ce}/\partial z)|^{-1} \sim 6-7$ km.

This fact is consistent with the gradual, ≈ 10-km downward, shift of the regions of optical airglow generation and elevated electron temperature formation with the simultaneous shift of the BUM peak toward the pump frequency, discovered in an EISCAT experiment [162]. Such a BUM shift for PW irradiation into the magnetic zenith was later observed in association with the generation of the descending layer of stimulated ionization in the ionosphere [38] (see also Section 5.3). However, these experiments at the Sura facility (see Figs 15, 19) were carried out using much lower PW powers than in Refs [162] and [38], and the PW was emitted vertically upward. The generation of descending layers at $f_0 \sim 4f_{ce}$ in the case of vertical incidence of a PW onto the ionosphere was not observed even at the maximally possible powers of the HAARP transmitter, although this experiment revealed the approach of the BUM peak to f_0 in the first 10 s of heating [38].

More detailed peculiarities of BUM dynamics on characteristic scales of $\sim \tau_3$, τ_{rel} are discussed in Refs [36, 45, 50, 155].

After PW transfer into the diagnostic pulse schedule, the process of relaxation of the striations, AA, and upper-hybrid components in the SEE spectrum generated by these pulses must lead to the restoration of the PPI-related components (NC_p and NCM), PSA effects, and quasiperiodic oscillations of the reflected PW signal. Such a behavior observed in experiments [55, 87] is illustrated in Figs 20–22. They clearly show that PW transfer to the pulse regime is followed by a decrease in the AA, UM component intensity, and DM component overshoot (see Figs 20, 21), in conjunction with the restorations of PSA effects, especially noticeable for later pulses, spikes (Fig. 22), and a delay in the onset of BUM generation with time (Fig. 20).

The last effect, explored more thoroughly in [54] (Fig. 23), indicates that a certain 'agent', most likely 'supersmall-scale irregularities' [163], involved in the process of BUM generation rapidly (for $t \lesssim 2-3$ s) relaxes after continuous pumping is switched off to the level at which the BUM component turns out to be lower than the noise level. However, BUM intensity begins to grow exponentially for $\sim 20-30$ s after a certain delay time τ_{del} under the effect of a PW pulse, with τ_{del} growing in the course of time after transfer to the pulsed pumping regime. To recall, in the case of a cold start and moderate PW power, a BUM develops for a few seconds (see Fig. 19), i.e., more slowly.

4.3.2 Fast dynamics of plasma waves associated with PW turn-on and turn-off. Data on SEE development in the presence of a 'prepared' striations in plasma contain important information on the nature of AIT and SEE relaxation after PW turn-off. SEE being a product of PlW (Langmuir, upper-hybrid, Z-mode, Bernstein) conversion into electromagnetic waves, the results of such measurements reflect the formation processes of the HF turbulence spectrum and allow PlW characteristics to be determined at the stages of turbulence development and relaxation. Examples of SEE relaxation at the initial and intermediate stages of AIT development were given in Section 2.2 (Fig. 4).

To study fast ($t \sim \tau_1 \ll \tau_3$) dynamics in the alternating regime (see Introduction, diagnostic schedule 2), a quasicontinuous signal with short pauses (20–50 ms) and a repetition period of 0.2–1 s is utilized instead of continuous pumping. Under such a schedule, the initial generation of artificial ionospheric turbulence (plasma waves and irregularities) occurs practically in the same manner as in the case of continuous pumping, since small-scale irregularities of plasma density have no time to relax appreciably during a pause and SEE intensity takes very little time (much less than the pulse length) to restore to the stationary level after a short pause. At the same time, SEE practically disappears during the pause, which allows the determination of characteristic times of its relaxation and, therefore, damping rates of plasma waves and/or Z-modes responsible for its generation.

An example of SEE spectrum restoration after a short pause and its relaxation during the pause is given in Fig. 24 at $f_0 \sim 5f_{ce}$. Figure 25 presents an example of SEE dynamics for the shift $\Delta f = -12$ kHz from the PW frequency $f_0 = 4380$ kHz (black line), where PW switch-off is followed by SEE relaxation with time τ_0. The same figure demonstrates diagnostic SEE dynamics (gray line) with relaxation time τ_d for the case of ionospheric heating at frequency $f_{01} = 5650$ kHz and diagnostic pulse probing at frequency $f_{DW} = f_0$.

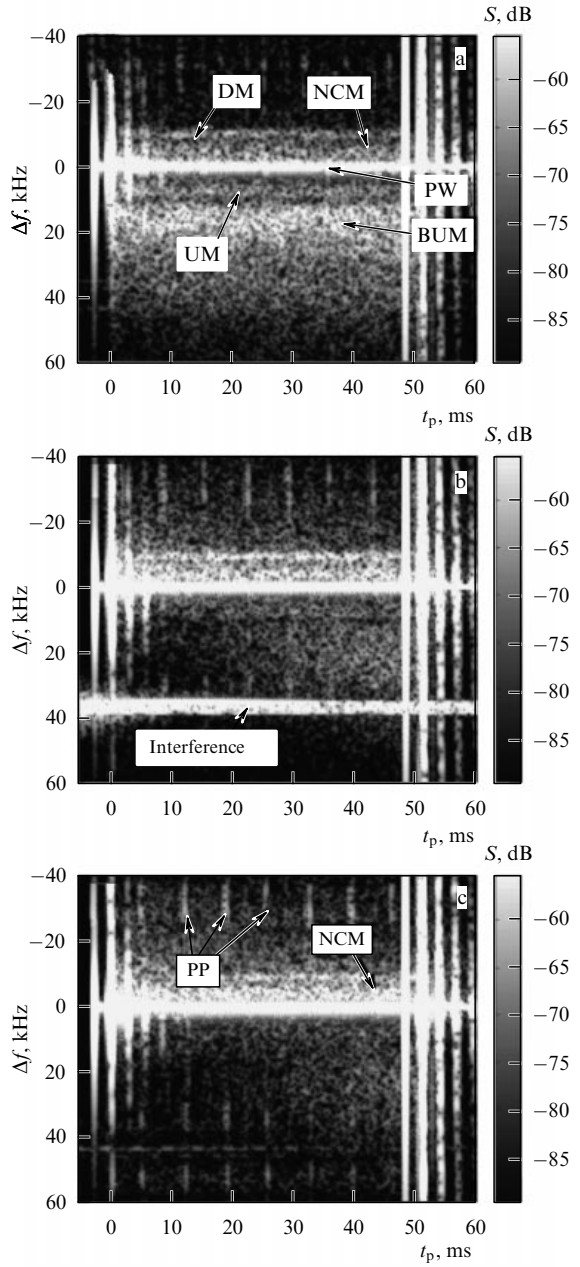

Figure 20. Spectrograms of the first (a), sixth (b), and tenth (c) diagnostic PW pulses after cessation of quasicontinuous heating (the first pulse emitted within 120 ms). The repetition period of diagnostic pulses is ∼ 1 s. Figure (a) shows SEE spectral components. Inscription 'PP' in figure (c) denotes PW parasitic pulses with a repetition frequency of about 150 Hz reflected from the ionosphere, which were used in this experiment as probing waves to evaluate AA. SEE intensity is expressed in dB relative to 1 mW; t_p is the time after arrival of the leading edge of the reflected diagnostic pulse. Sura facility, 24.09.98, $f_0 > 5f_{ce}$ [55].

The dynamics of diagnostic SEE in a pulse at various Δf in the case of additional heating at $f_{01} = 5650$ kHz ($f_{DW} = 4740$ kHz) is exemplified in Fig. 26. The character of SEE dynamics at the stage of emission development when the spectrum expands toward smaller detunings is similar to that at the PPI stage, as shown in Fig. 4. The same is true of the relaxation stage after switch-off of the diagnostic wave pulse. At the beginning, the flattening of the spectrum in a broad band of frequency shifts occurs, and for the most remote shifts not only in conjunction with a delay of intensity reduction but also with the strengthening of emission (for $\Delta f = 66$ kHz).

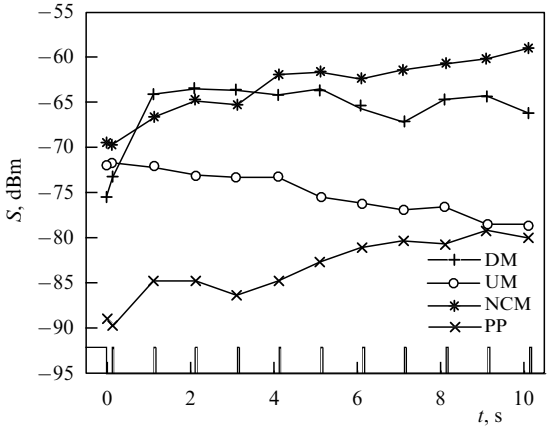

Figure 21. Dynamics of intensities of the DM, NCM, and UM features and of the reflected parasitic signal (PP) after PW transfer to the pulsed regime. Continuous PW emission and diagnostic pulses are shown schematically above the time-axis at the bottom [55].

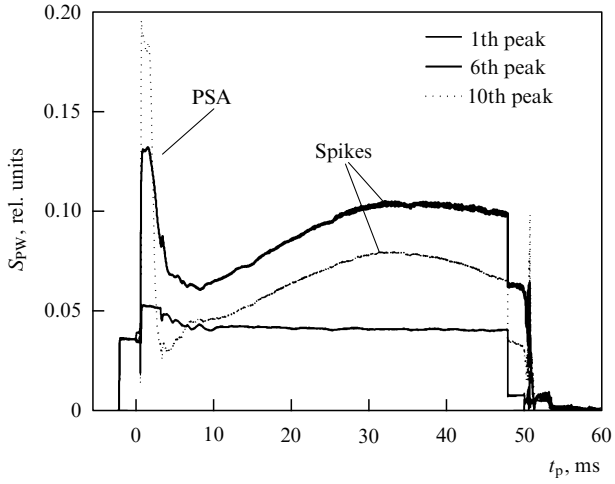

Figure 22. Intensity of the first, sixth, and tenth 50-ms diagnostic PW pulses with the repetition period of 1 s, reflected from the ionosphere. The figure shows PSA effects and quasiperiodic oscillations of the signal (spikes) [55].

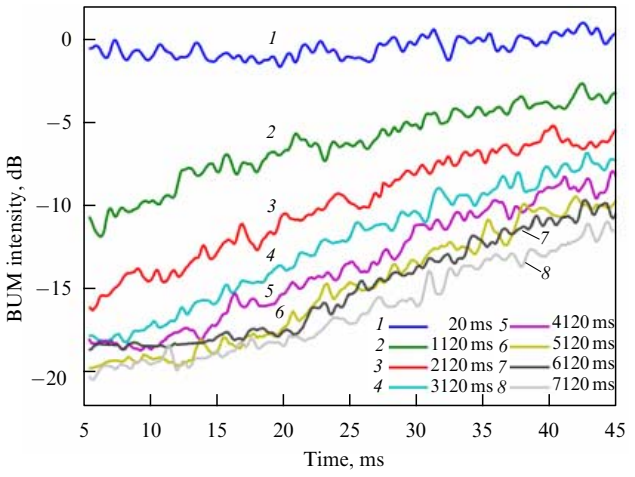

Figure 23. (Color online.) Dynamics of integral normalized BUM intensity during 50-ms diagnostic pulses with the repetition period of 1 s after switch-off of the quasicontinuous pumping. Time of the onset of pulse emission after PW switch-off is shown in the figure. Sura facility, 24.09.98, $f_0 > 5f_{ce}$. The data are averaged over sessions with different Δf_{BUM}. The delay time τ_{del} of BUM generation increases with pulse number. BUM generation stopped for $\tau_{del} > 20$ ms [54].

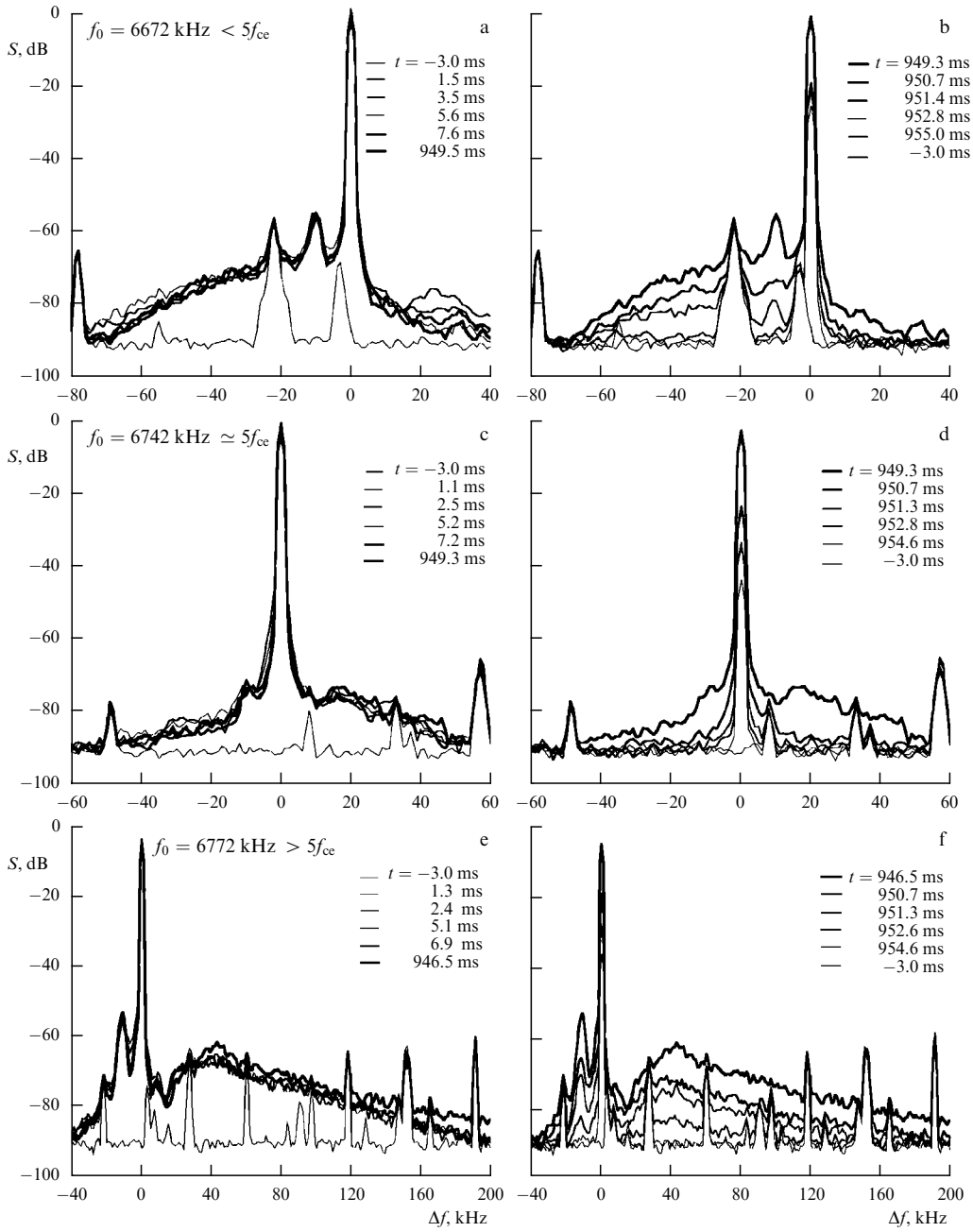

Figure 24. SEE spectra dynamics for quasicontinuous heating. Pulse duration $\tau_p = 950$ ms, and repetition period 1 s at the stages of SEE development after a 50-ms pause (a, c, e) and relaxation (b, d, f). Averaged over 23 pulses: $f_0 = 6672$ kHz $< 5f_{ce}$ (a, b); $f_0 = 6742$ kHz $\simeq 5f_{ce}$ (c, d), and $f_0 = 6772$ kHz $> 5f_{ce}$ (e, f). Sura facility, 26.09.1998 [51].

Such dynamics is a striking manifestation of downward PlW energy transfer along the frequency spectrum; it was described for the first time in Refs [94, 164].

Figure 27 presents results of the measurement of SEE relaxation decrements and diagnostic SEE in the range of 4380–6450 kHz encompassing the region of the fourth harmonic of electron gyrofrequency, $4f_{ce} \sim 5400$ kHz. Evidently, there is a maximum of SEE relaxation decrement at $f_0 \sim f_{DW} \sim 4f_{ce}$. Calculation of frequency ω dependence of PlW relaxation rates for the conditions of this experiment showed that such dependence must take place at altitudes somewhat below the UHR altitude, i.e., as $\omega > \omega_{UH}$, for plasma waves with $k_\perp \rho_e \sim 0.1-0.15$ s and the wave vector directed at the angle $\theta \sim 60^\circ - 70^\circ$ to the magnetic field [93]. This suggests the important role of 'oblique' waves in upper-hybrid turbulence and SEE generation.

5. Electron acceleration, optical airglow, and additional ionization

5.1 Theoretical notion

PW-excited plasma waves are known to accelerate electrons to energies $\mathcal{E}$ up to tens of electron-volts (60 eV according to papers [48, 59]). The appearance of accelerated electrons gives rise to a number of observable effects in the F region of

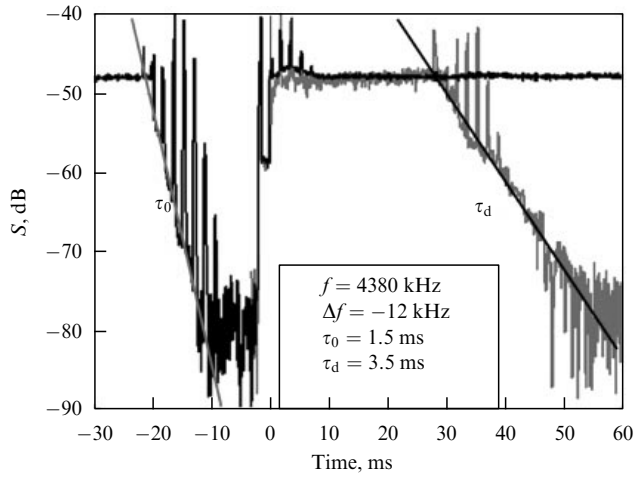

Figure 25. An example of SEE evolution in the case of quasicontinuous heating (black oscillogram) and diagnostic pulse pumping (gray oscillogram) [93].

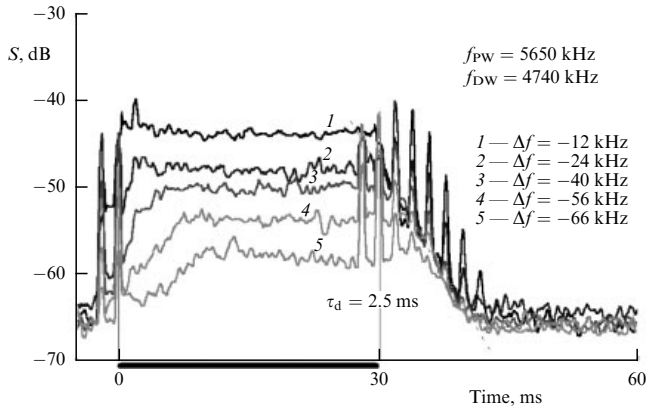

Figure 26. Dynamics of SEE generated by a diagnostic wave with frequency $f_{DW} = 4740$ kHz at various detunings Δf in the case of intense striations created by a PW with $f_0 = 5650$ MHz. Sura facility, 25.09.2003. $P_{DW} = 15$ MW, averaged over 30 pulses. Delays of SEE development and relaxation at larger Δf related to PlW transfer along the spectrum are quite apparent [66].

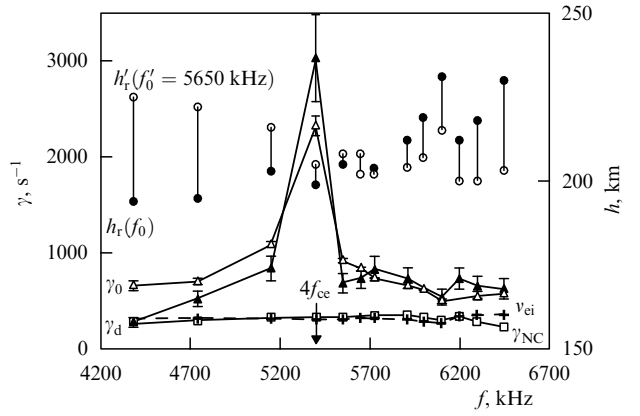

Figure 27. Dependences of damping rates of SEE upper-hybrid components (γ_0) (△), diagnostic SEE (γ_d) (▲), and Langmuir component of diagnostic SEE (γ_{NC}) (□) on the PW frequency ($f = f_0$) and diagnostic probing frequency ($f = f_{DW}$) at different altitudes h in the disturbed region. White dots (○) correspond to the altitudes at which pump waves are reflected for $f_0 = 5650$ kHz, black dots (●) denote altitudes for other frequencies. Also presented are calculated frequencies of ν_{ei}(+) electron–ion collisions. Sura facility, 24.09.2003, 10:00-14:45 UTC [66, 93].

ionosphere, such as enhanced optical airglow and additional ionization of the ionospheric plasma. Accelerated electrons probably contribute to SEE generation [148, 165] and emission in the microwave range [166].

The first models of the formation of suprathermal particles upon irradiation of the ionosphere with high-power radio waves were based on the one-dimensional quasilinear theory of electron acceleration by plasma waves excited during PPI development in the vicinity of the PW reflection point [167]. A condition for efficient acceleration is known to be Cherenkov's condition $\omega = \mathbf{kv}$, where $\mathbf{v}$ is the electron velocity. From this condition it follows that the effective interaction between electrons and plasma turbulence occurs for $v > V_{Ph}$ ($V_{Ph} = \omega/k$ is the phase velocity of plasma waves).

There is a large 'starting' population of such electrons (photoelectrons) in the ionosphere at daytime. The formation of an ultrathermal tail of the electron distribution function near the reflection point, where strong Langmuir turbulence is excited at the initial stage of pumping effect, is a result of random gain and loss of small portions of energy $\Delta\mathcal{E} \sim e|E_1|/k$ during rapid (compared with the wave period $1/\omega$) intersection of collapsing ($\sim 1/k$ in size), cavitons [168, 169]. According to Refs [74, 170, 171], such a process can be modelled with the Fokker–Planck equation for the one-dimensional tail of the averaged distribution function $f(v)$:

$$\frac{\partial f}{\partial t} + v_z \frac{\partial f}{\partial z} = \frac{\omega_{pe}^2}{m_e N_e} \frac{\partial}{\partial v} \frac{W_{k=\omega/v}}{v} \frac{\partial f}{\partial v}\,, \tag{31}$$

where W_k is the spectral energy density of Langmuir waves. However, electrons with energies $\mathcal{E} > m_e V_{Ph}^2/2$ rather quickly (for fractions of a millisecond) intersect the PPI excitation region; this time is too short to gain enough energy as a result of acceleration. In such a case, the lifetime τ_a of an electron needs to be increased in the plasma turbulence region, e.g., through its multiple intersection by electrons undergoing elastic collisions with heavy particles, first and foremost neutral ones, outside it. Such a mechanism was considered in Refs [172–174], where the authors derived and analyzed the diffusion equation for $F(v, z)$, i.e., evolution of the isotropic part of the distribution function beyond the borders of the accelerating layer under its influence (here, v is the electron speed):

$$\frac{\partial F}{\partial t} - \frac{\partial}{\partial z}\left(D_c \frac{\partial F}{\partial z}\right) = S_0(F)\,, \quad D_c = \frac{v^2}{3\nu^g}\,, \tag{32}$$

where ν^g is the collision frequency of fast electrons with neutral particles, S_0 is the collision integral averaged over pitch angles, and D_c is the diffusion coefficient. Additional ionization by accelerated electrons was calculated in Refs [173, 175] for the region of size $L_\mathcal{E}$ adjacent to the PW reflection point ($L_\mathcal{E}$ is the scale of energy losses by fast electrons in inelastic collisions, $L_\mathcal{E} \gg L$, L is the longitudinal (along z-axis) dimension of the PlW localization region).

The lifetime τ_a also increases under the effect of turbulent electron trapping in the acceleration region related to their scattering from plasma waves nonunidimensionally distributed in the wave vector space [176, 177]. Such nonunidimensionality develops when there is a high enough turbulence level due to nonlinear PlW transfer along the spectrum [62, 117]. Then electron diffusion in the velocity space proceeds not only in energies but also in pitch angles, and the spreading of electrons along z-axis in the PlW localization region

becomes diffusive [176–178]:

$$\frac{\partial F}{\partial t} = \frac{\partial}{\partial z} D_1 \frac{\partial F}{\partial z} + \frac{1}{v^2} \frac{\partial}{\partial v} v^2 D_2 \frac{\partial F}{\partial v} + q(v,z)\,, \tag{33}$$

$$D_1 = \frac{v^5 m_e N_e}{6\omega W V_{Ph}}\,, \quad D_2 = \frac{2\omega W V_{Ph}^3}{v^3 m_e N_e}\,, \tag{34}$$

$F(v)$ is the isotropic part of the distribution function, $q(v,z)$ is the source of fast particles that can be related to both their input across the border of the plasma turbulence region and their production inside this region, e.g., as a result of photoionization, and W is the integral PlW energy density. It is easy to estimate from Eqn (32) the characteristic energy $\mathcal{E}^*$ that electrons must acquire during acceleration, and the lifetime τ_a of electrons with such energy in the layer having characteristic thickness L. Indeed, the lifetime of an electron having velocity v can be estimated as L^2/D_1, and its energy $\mathcal{E}$ at the exit from the layer as $m_e D_2 \tau$. Therefore, one has

$$\mathcal{E}^* \sim m_e \left(\omega L V_{Ph}^2 \frac{W}{m_e N_e}\right)^{2/5}, \quad \tau_a \sim \frac{L}{V_{Ph}}\,. \tag{35}$$

The effective velocity of a particle crossing the layer with nonunidimensional plasma turbulence equals the phase velocity of plasma waves V_{Ph}. In Sura experiments, $\mathcal{E}^* \sim 25-30$ eV or higher than excitation potentials for optical airglow and ionization potentials of the main neutral components of atomic oxygen ($I_O = 13.6$ eV) and molecular nitrogen ($I_{N_2} = 15.6$ eV). The PW power of the EISCAT and HAARP transmitters is greater than that of Sura radio facility; therefore, both the characteristic energy $\mathcal{E}^*$ of accelerated electrons and the acceleration region size must increase. It was shown that both mechanisms, turbulent trapping together with acceleration (33) in the layer with turbulence and diffusion (32) in collisions with heavy particles outside this layer, are needed to interpret the available experimental data.

Electron acceleration during HF pumping of the ionosphere near electron gyroharmonics $f_0 \sim sf_{ce}$ was considered in Refs [148, 174]. It was shown in paper [148] that a high enough efficiency of acceleration by plasma waves in the UHR region leads to the formation of the distribution function of suprathermal electrons with marked transverse anisotropy. The relevant acceleration condition obeys the expression as follows:

$$\omega = s\omega_{ce} + k_{\|} v_{\|}\,. \tag{36}$$

Such waves turn out to be 'forced' in the direction $\perp \mathbf{B}_0$, as a result of collisionless cyclotron damping. The existence of such waves was demonstrated in experiment [93] (see Section 4.3.2).

An alternative mechanism of stochastic electron heating by transverse plasma waves in the AIT region has recently been suggested [179]. It is analogous to the mechanism alluded to in work [180] for interpreting the heating in the runaway shock wave region. However, the validity of this interpretation remains to be confirmed.

5.2 Optical airglow of the ionosphere

Optical airglow of the night ionosphere induced by high-power radio waves was investigated in numerous studies (see, e.g., Refs [48, 59, 67, 181–191] and reference cited therein). The main measurements of optical airglow are performed in red ($\lambda = 630$ nm) and green ($\lambda = 557.7$ nm) lines of atomic oxygen related to emission by $O(^1D)$ and $O(^1S)$ atomic levels with excitation energies $\mathcal{E}_{ex} = 1.96$ and 4.17 eV, and lifetimes $\tilde{\tau} = 107$ s and 0.7 s, respectively. The airglow was also detected in the lines $\lambda = 844.6$ nm with $\mathcal{E}_{ex} = 10.99$ eV, and $\lambda = 427.8$ nm with $\mathcal{E}_{ex} > 19$ eV at $\tilde{\tau} \simeq 10^{-6} - 10^{-5}$ s. Airglow in the blue line of the molecular nitrogen ion $N_2^+(B_2\Sigma_u^+)$ with $\lambda = 427.8$ nm is of special interest, because it is an indicator of additional ionization of nitrogen molecules under the action of pumping.

Night-sky airglow portraits are recorded by wide-angle digital photo and video cameras with long enough pumping times. Comparing glow intensity in different lines with the results of numerical simulations of photochemical processes responsible for the airglow excitation allows us to estimate the distribution function of accelerated electrons [48] and

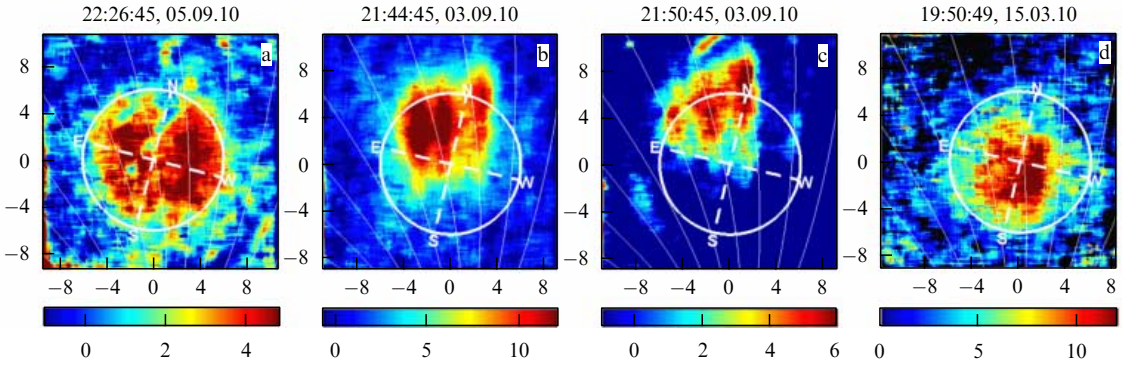

Figure 28. (Color online.) Series of optical images recorded on 03-05.09.2010 (a–c) and 15.03.2010 (d) in the night sky at the end of 2-min quasi-continuous vertical radio emissions by the Sura facility for different ionospheric conditions. Time (UTC + 4 h (figures a–c) and UTC + 3 h (figure d) and dates are shown at the top of each figure. Angular dimensions of the images in degrees are plotted on the axes. The altitude of reflection of the pump wave at frequencies $f_0 = 4375$ kHz (a) and $f_0 = 4300$ kHz (d) was 250 km and 280 km, respectively. Sura operating frequency was close to the ionospheric critical frequency f_{OF_2}, and PW UHR region was located much lower (around 255 km). Images in figures b and c were obtained at $f_0 = 4375$ kHz as the reflection altitude increased from 265 to 280 km for 6 min. Here, the artificial airglow region is displaced $3^\circ - 6^\circ$ northward with respect to the center of the directional pattern of the facility (the higher the PW reflection altitude, the greater the displacement). It has the form of optical glow bands extended along the projection of the magnetic field $\mathbf{B}_0$. Their angular transverse dimension is $0.5^\circ - 2^\circ$, and the distance between them is $1^\circ - 3^\circ$. The white circumference shows the boundaries of the antenna pattern; thin white lines denote the direction of projection of magnetic lines of a field $\mathbf{B}_0$ onto the image plane at the altitude of 250 km [188].

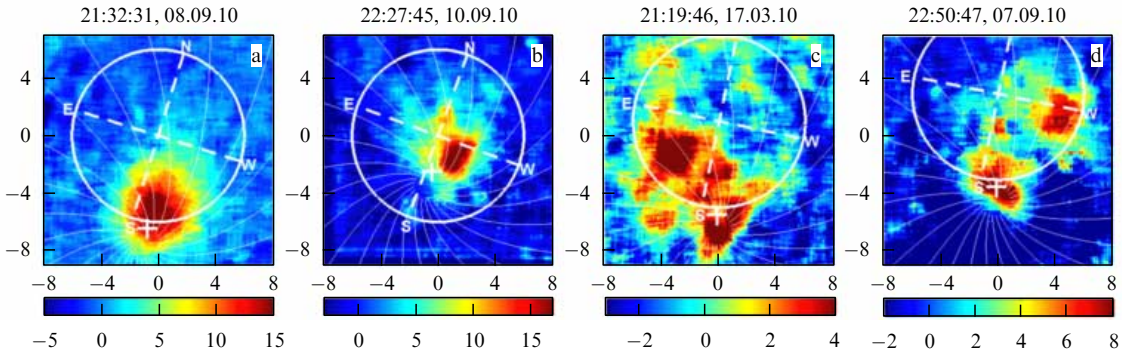

Figure 29. (Color online.) Examples of optical images obtained in 2010 at the end of 2-min quasicontinuous vertical radio emissions by the Sura facility with the directional pattern sloping 12° (a, c, d) and 16° (b) southward. PW frequencies f_0 are 4740 kHz (a), 4375 kHz (b, d), and 4300 kHz (c). Moscow summer time (UTC + 4 h) and dates are shown at the top of each figure. The cross corresponds to the line of sight directed toward the magnetic zenith [188].

determine the causes behind the appearance of energetic particles (ohmic heating or acceleration at the distribution function tail) [182, 187, 189, 191]. Registration of the airglow makes it possible to study the large-scale structure of the disturbed ionosphere, including magnetically oriented plasma structures [184, 188], location of the glowing region with respect to the area 'illuminated' by powerful radio emission, regular drift motion, and irregular movements of enhanced airglow areas, etc. There are numerous publications concerning investigations into the influence of powerful HF radio emission on optical airglow. The most comprehensive review of this literature can be found in the study by Kosch et al. [59].

A series of night-sky portraits in the red line from atomic oxygen O(^{1}D), recorded at the Sura heating facility in September 2010, is presented in Figs 28 and 29 [188]. Thin white lines in the figures correspond to projections of geomagnetic field lines onto the camera's field of view at an altitude of 250 km. Figure 28 (vertical pumping) illustrates the temporal northward displacement of the glowing spot with time, related to the increase in the PW reflection altitude to $\sim$ 280 km and the precipitation of energetic electrons along the geomagnetic field **B** from the acceleration region to denser atmospheric layers up to altitudes of about 250 km, where the airglow is excited, and to the formation of magnetically oriented structures with the transverse scales on the order of 1–2 km in the disturbed region. Earlier Sura experiments dating to 1995 and 2004 demonstrated the eastward motion of the glowing spot during its drift in the crossed electric and magnetic fields [186, 192]. The effect of the eastward–westward drift of the glowing spot and its northward extension was recorded earlier at the Arecibo Observatory [181]. The authors of Ref. [184] measured airglow in the green line at the HAARP facility and demonstrated the emergence of extended structures in the case of pumping into the magnetic zenith.

Figure 29 displays night-sky portraits recorded at the Sura facility with the directional pattern sloping southward in the plane of the geomagnetic meridian. It can be seen that in the majority of the pumping sessions the airglow spot occurred in the magnetic zenith (18.5°) regardless of the antenna inclination through either 12° or 16°. This means that the 'magnetic-zenith' effect revealed by the EISCAT and HAARP polar heating facilities ($\alpha_I = 12°$ and 14°, respectively) as the enhancement of various pumping-related effects, when the pump beam was directed along the magnetic field [190, 193–195], was manifested in the Sura experiments ($\alpha_I = 18.5°$) as the shift of the artificial airglow spot into the magnetic zenith at different slope angles of the directional pattern toward the south and rather low PW frequencies. Such a position of the glowing spot at different slope angles of the directional pattern toward the south (but not in case of vertical pumping) was also found upon the analysis of the data obtained in the 2000 EISCAT experiment [190].

When the directional pattern slopes southward during the post-sunset decrease in the ionospheric critical frequency f_{OF_2} to a value exceeding the Sura operating frequency by not more than 0.5 MHz, a 'change of sign' of the PW action on optical airglow of the ionosphere was documented: the generation of artificial airglow in the red line was replaced

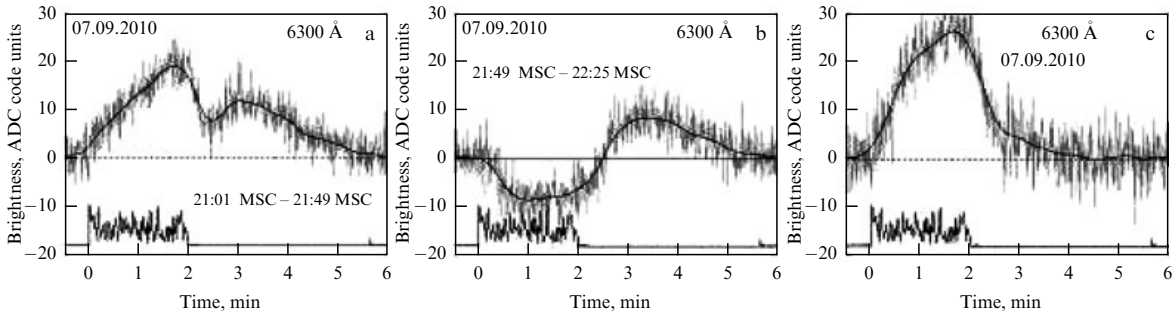

Figure 30. Dynamics of airglow brightness in the red line $\lambda = 630$ nm obtained by averaging (superposed epoch method) over several heating sessions. Bottom curves — signal of the facility. (a) Additive effect of electron heating and acceleration. (b) Heating effect alone. (c) Difference curve corresponding only to the effect of impact excitation by accelerated electrons [187].

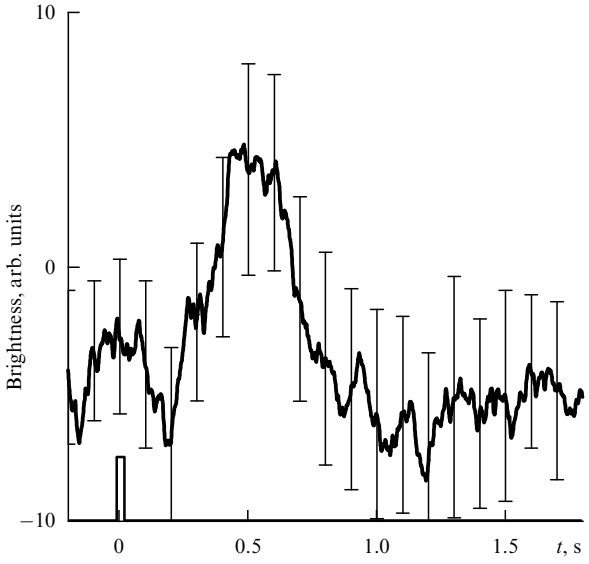

Figure 31. Photometer signal in the green line ($\lambda = 557.7$ nm) during pulsed emission by the Sura facility in 17:17:40–17:18:20 (UTC, 07.09.2910) averaged over 30 consecutive pulse repetition periods. Pulse duration $\tau_p = 30$ ms, repetition period 2 s. The rectangle on the abscissa indicates PW pulse emission time. The origin of the y-axis corresponds to the mean photometer signal value in the absence of stimulated optical airglow.

by suppression of background glow of the night sky. As a rule, switching off the Sura facility resulted in a decrease of airglow brightness followed by its temporary several percent increase over the stationary averaged background intensity. This additional post-airglow was noticeable even in those sessions where artificial airglow was observed in the 630-nm line (Fig. 30).

Such behavior of the airglow brightness can be accounted for based on the adequate consideration not only of electron acceleration but also of plasma heating by a powerful wave and temperature dependence of the dissociative recombination coefficient of electrons and molecular oxygen ions. The recombination is known to be responsible for the production of oxygen atoms in the excited state $O(^1D)$ [5]. The lowering of the background brightness under the pumping effect is related to a decrease in the recombination coefficient with increasing electron temperature: $\alpha_{eff} \propto T_e^{-1/2}$, while a small subsequent rise in brightness is due to the accumulation of molecular oxygen ions O_2^+ during pumping. This effect prevails when the efficiency of electron acceleration by plasma waves decreases for some reason or other and can be used for the diagnostics of aeronomic processes in the upper atmosphere.

More rapid measurements of airglow in the short-lived line $O(^1S)$ with the use of electrophotometers, supported by SEE measurements, showed that in the case of electron acceleration by short pulses ($\tau_p = 5$ ms) it is determined by Langmuir waves, whereas upper-hybrid waves play the key role after transition from prolonged continuous irradiation to a pulsed impact [183, 196]. An example of measuring luminescence by a photometer is presented in Fig. 31 [188].

5.3 Additional ionization and descending layers

The character of electron acceleration changes dramatically for $\mathcal{E}^* > I_\gamma$ ($\gamma = O, N_2$) [177]: the ionization source S_{en}^+ related to collisions of accelerated electrons with neutral particles appears on the right-hand side of Eqn (33)]197]; namely

$$S_{en}^+ = S_1 + S_2 - S_3 = N_n \frac{v}{\mathcal{E}} \left[\int_{\mathcal{E}+E_\gamma}^{2\mathcal{E}+E_\gamma} \mathcal{E}' I^+(\mathcal{E}', \mathcal{E}' - \mathcal{E} - I_\gamma) F(\mathcal{E}') \, d\mathcal{E}' + \int_{2\mathcal{E}+I_\gamma}^{\infty} \mathcal{E}' I^+(\mathcal{E}', \mathcal{E}) F(\mathcal{E}') \, d\mathcal{E}' - \mathcal{E}\sigma^+(\mathcal{E}) F(\mathcal{E}) \right]. \quad (37)$$

The first term (S_1) in formula (37) describes the appearance of electrons with energy $\mathcal{E}$ due to a change in the energy of electrons with energy $\mathcal{E}'$ (scattered electrons); the second term (S_2) characterizes the appearance of secondary electrons with energy $\mathcal{E}$, and the third one ($-S_3$) reflects a decrease in the number of electrons with energy $\mathcal{E}$ due to ionizing collisions. Here, $I^+(\mathcal{E}_1, \mathcal{E}_2)$ is the partial differential cross section of ionization by a primary electron with energy $\mathcal{E}_1$, resulting in the emission of an electron with energy $\mathcal{E}_2$, $\sigma^+(\mathcal{E}) = \int I^+(\mathcal{E}_1, \mathcal{E}_2) \, d\mathcal{E}_2$ is the partial cross section of ionization by an electron with energy $\mathcal{E}_1$. In each ionization event, the energy conservation law $\mathcal{E}_1 = \mathcal{E}_1' + \mathcal{E}_2 + I_\gamma$, where $\mathcal{E}_1'$ is the 'scattered' electron energy, is fulfilled. In other words, some of the secondary electrons, produced in the plasma, enter the region of energies $\mathcal{E} > \mathcal{E}_{Ph} = m_e V_{Ph}^2/2$, are once again accelerated by plasma waves up to energies $\mathcal{E} \sim \mathcal{E}^* > I_\gamma$, and can many times participate in the ionization process. The loss of fast particles from the characteristic energy interval of acceleration, $m_e V_{Ph}^2/2 = \mathcal{E}_{Ph} < \mathcal{E} < \mathcal{E}^*$, is largely attributable to their escape from the acceleration region and secondary electrons entering into the energy region of $\mathcal{E} < \mathcal{E}_{Ph}$. This means that additional ionization leads to a marked rise in suprathermal particle concentration N_a in the plasma turbulence region. The exponential growth of N_a begins after the threshold level $W_{ion,th}$ of PlW energy density or turbulence region size L is reached [177]. The threshold of such instability is given by the approximate equality

$$\nu_{ion} \tau_a \sim 1, \quad (38)$$

where $\nu_{ion} = \sqrt{2\mathcal{E}^*/m_e}\, \sigma^+(\mathcal{E}^*) N_n$ is the frequency of ionizing collisions between electrons with energy $\mathcal{E}^*$, and N_n is the neutral particle concentration. Stabilization of the instability at the $N_a/N_e \sim (\nu_e/\omega)(\mathcal{E}^*/\mathcal{E}_{Ph})$ level is due to saturation of the energy density of plasma waves at the threshold level attributable to enhanced Landau damping on suprathermal particles. Secondary electrons entering the energy region $\mathcal{E} < \mathcal{E}_{Ph}$ in the process of ionization increase background plasma concentration, with the additional concentration $N_{add}/N_e \sim [\nu_{ion}(\mathcal{E}^*)]/\beta(\mathcal{E}_{Ph}/I_\gamma)$ (β^{-1} is the electron lifetime) amounting to $\sim 25-50\%$ of the total at large enough values of $L \sim 5-10$ km.

Additional ionospheric ionization was detected in experiment by multifrequency Doppler sounding of the disturbed region [24, 28, 198, 199]. It was shown that a powerful radio wave can sometimes cause a 1–1.5 Hz positive Doppler shift in the frequency of probe radio waves reflected from the ionosphere. Such an effect cannot be produced by ionization–recombination unbalance in the lower ionosphere due to heating [200] and appears by virtue of ionization of the main neutral components in collisions with accelerated electrons having energies in excess of ionization potentials of atomic oxygen (I_O) and molecular nitrogen (I_{N_2}).

This method was applied in a series of Sura experiments carried out in 1999–2001 at pump frequencies close to the

electron gyroharmonics: $f_0 \sim sf_{ce}$ ($s = 4, 5, 6$). In most cases, very apparent positive Doppler shifts of the probe wave frequencies ($f_D \sim 0.2-1.4$ Hz) were recorded, in contrast to the 'silence period' of a powerful radio wave. Negative f_D values were observed in a small number of pumping sessions, when f_D values for $f_0 > sf_{ce}$ were much higher than for $f_0 < sf_{ce}$. The experimental f_0/sf_{ce} ratio was retrieved from SEE spectra. (Positive f_D values correspond to a rise in N_e with time along the probe wave propagation pathway.) The rise in N_e due to ionization–recombination disbalance in the lower ionosphere must not depend on the ratio f_0/sf_{ce} [200], which means that the above experiments demonstrated additional ionization of the F-layer ionosphere by accelerated electrons, especially strong for $f_0 > sf_{ce}$. Notice that Refs [48, 201] report a higher intensity of stimulated optical airglow for $f_0 > sf_{ce}$ ($s = 2, 4$) than in the inverse case, while Ref. [132] gives evidence of enhanced intensity of small-scale irregularities for $f_0 > 4f_{ce}$. At the same time, positive f_D values were observed in Ref. [199] for $f_0 < sf_{ce}$, and negative values for $f_0 > 4f_{ce}$, which suggests a decrease in N_e and the forcing of plasma out of the PW UHR region (see also Section 6).

The HAARP experiments of 2008–2011 undertaken after bringing the facility to full power revealed artificial ionization layers descending within 40 km under the initially undisturbed layer. The first observations of artificially ionized plasma layers were made in experiments at the HAARP heating facility [37, 202] with the use of an incoherent scattering radar, an ionosonde, and all-sky cameras mounted at the heating facility to measure changes of the airglow brightness in the green (557.7 nm) and blue (427.8 nm) lines and 100 km away from it for measurement in the green line. Figure 32 demonstrates the results obtained by optical measurements and an ionosonde during a session 4 min in duration. It follows from the vertical airglow profile that the brightest region of green airglow in the middle of the top images descends in the course of time from 200 to 150 km (Fig. 32c).

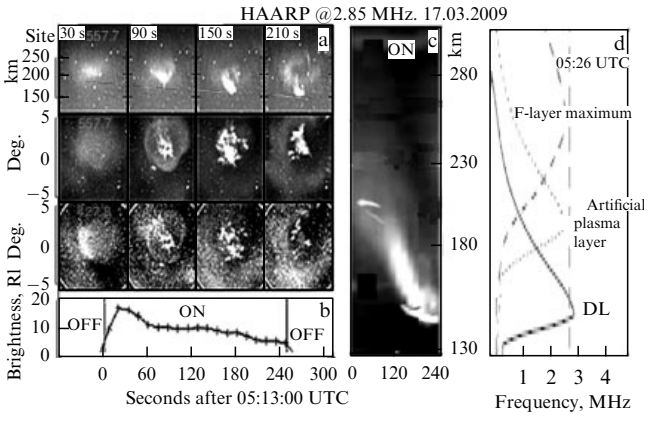

Figure 32. (a) Artificial ionospheric airglow portraits recorded by a remote camera (top row, green line, $\lambda = 557.7$ nm, altitude indicated) and a camera placed on the facility parallel to a magnetic field in green (2nd row) and blue, $\lambda = 427.8$ nm, (3rd row) lines. (b) Mean blue line intensity in the middle of portraits in the 3rd row during a pulse emitted at 05:13:00 (UTC). (c) Time dependences of the height profile of green luminescence obtained by a remote camera. (d) Height profiles of ionization obtained by an ionosonde at 05:26 UTC. F-layer maxima and two layers of artificial plasma: one near the lower edge of the F-layer maximum, the other descending 50 km along the magnetic field (DL) [37]. Reproduced with permission of the American Geophysical Union (AGU).

Images obtained with a camera mounted on the heating facility demonstrate that emission areas in the green and blue lines change in a similar manner. Since blue line emission reflects ionization of nitrogen molecules, it can be concluded that a new freshly ionized plasma forms in the descending region. This conclusion agrees with the results of ionosonde measurements. Also, the speed of descent from ~ 190 km till the stop at the altitude of ~ 150 km is roughly constant and equals $v_{obs} \approx 300$ m s^{-1}. Descending radar scattering and green glowing regions had been observed in the earlier EISCAT experiments [162, 203, 204], but only data reported in Ref. [37] provided definitive evidence of descending layers of artificial ionization.

Thus far, such descending layers have been registered in a wide range of pump wave frequencies from 2.85 to 7.1 MHz [38, 74, 143] by measuring the virtual altitude of reflection of diagnostic waves with $f_{DW} = f_0$, the pulses of which were emitted during pauses in quasicontinuous pumping, by SEE measurements, and by sounding AIT regions with the MUIR radar (HAARP and the EISCAT radar (EISCAT). Also, sweeping of f_0 around sf_{ce} was also employed to study descending artificial layers. Figures 33–35 demonstrate, respectively, the time dependence of SEE spectra for $f_0 =$ 5850 kHz ($\simeq 4f_{ce} + 70$ kHz), time-dependent changes in the amplitude of the pulsed ($\tau_p = 100$ μs) signal at $f_0 = 5820$ kHz reflected (scattered) from the ionosphere at different virtual

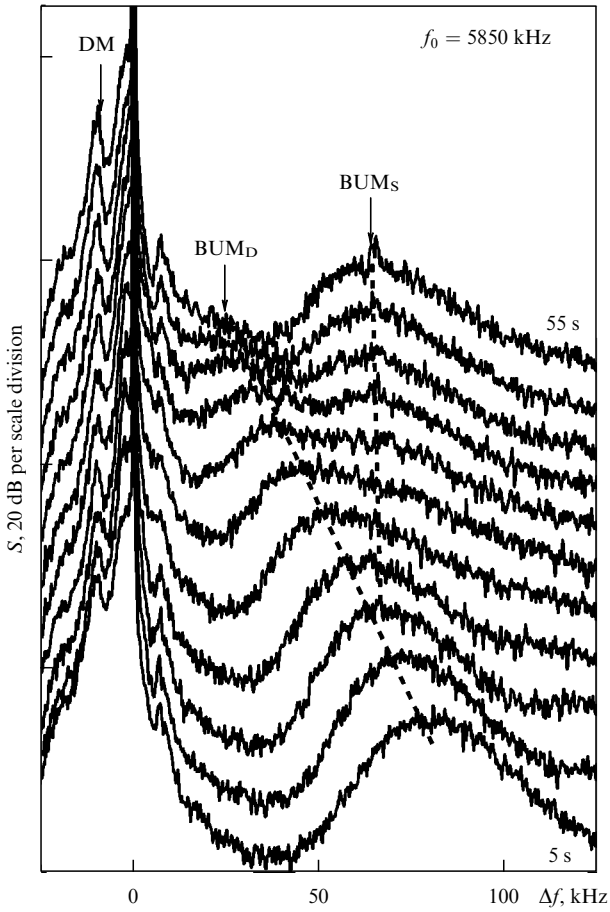

Figure 33. SEE spectra at $f_0 = 5850$ kHz. HAARP facility, 28.03.11. 15:50:50–15:50:30 AST with a 5-s interval beginning from the 5th second of heating. Consecutive spectra are upshifted by 5 dB along the ordinate axis. Dashed lines denote peak positions of BUM$_S$ and BUM$_D$ features [38].

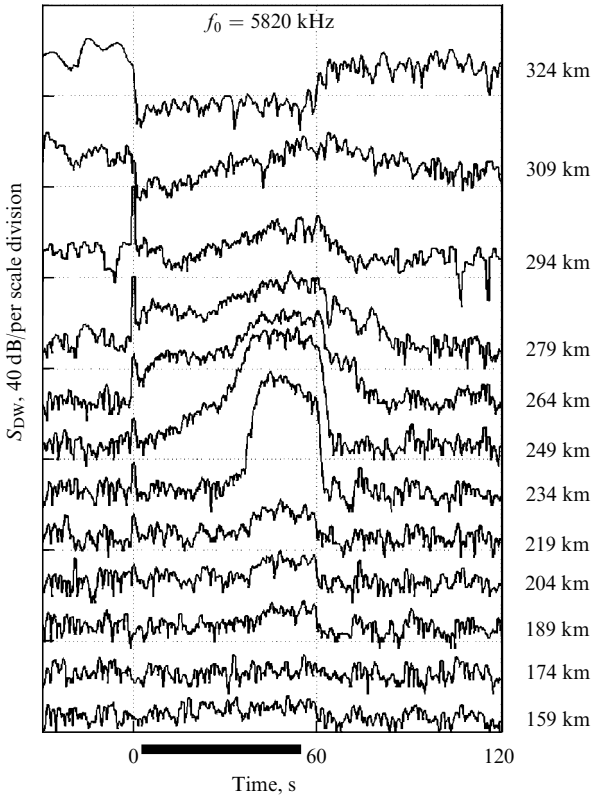

Figure 34. Depicted are intensities of the diagnostic signal reflected from the ionosphere depending on time for different virtual reflection altitudes (right) at $f_0 = 5820$ kHz. 15:45:00–15:47:30 AST. The lines are shifted by 20 dB. Bold line at the bottom shows time of quasicontinuous emission by the HAARP facility. A significant enhancement (up to 50 dB) of the signal reflected from 234 and 249 km (65–75 km below the initial virtual reflection altitude) is quite apparent within $\approx 35-40$ s after PW turn-on [143].

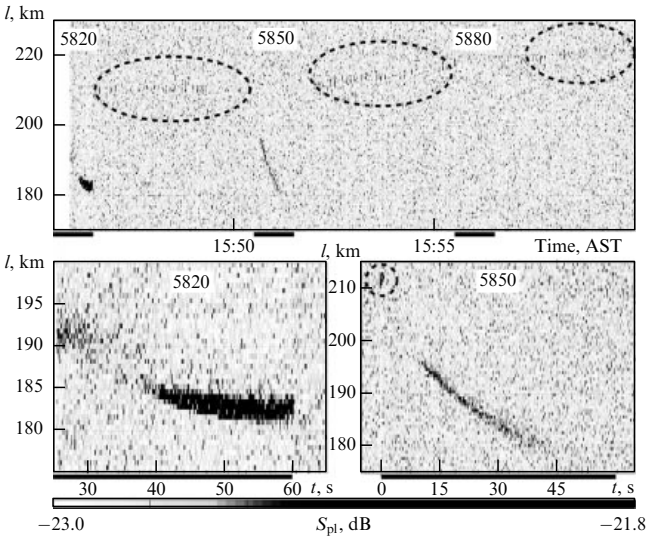

Figure 35. Depicted are intensities S_{pl} of MUIR plasma line signal depending on time and distance $l = h/\sin\alpha_l$ in the case of PW emission into the magnetic zenith at frequencies 5820, 5850, and 5880 kHz. HAARP facility, 28.03.2011, 15:45:30–16:00:00 AST. Bold lines at the bottom of each panel denote time of quasicontinuous emission. Dotted circles encompass regions of enhanced plasma line in the case of pulsed PW emission ($\tau_p = 20$ ms, $T = 1$ s). Lower figures — magnified images obtained after quasicontinuous PW emissions on 15:45:30–15:46:30 AST ($f_0 = 5820$ kHz) and 15:50:30–15:51:30 AST ($f_0 = 5850$ kHz). The radar was turned on at approximately 15:45:55 AST, 28.03.2011 [38, 143].

altitudes, and the plasma line signal intensity of the MUIR radar, depending on time and distance [38, 143].

It was shown that 10–15 s after PW switch-on, the BUM component splits into a 'traditional' BUM_S having a fixed position in the spectrum at $\Delta f_{BUM_S} \simeq 50$ kHz, and a 'drifting' BUM_D with a peak approaching the PW frequency at a rate of $r_f = |d\Delta f_{BUM_D}/dt| \approx 1.2$ kHz s^{-1}. According to formula (23) and the IGRF geomagnetic field model, this corresponds to the speed of descent of the BUM generation region, $v_{BUM} \approx 450-500$ m s^{-1}. Simultaneously, distance l to the region of plasma line generation (MUIR radar signal) decreases with approximately the same speed; the virtual altitude h_{diagn} at which the leading edge of diagnostic pulses is reflected also decreases, giving direct evidence of an increase in plasma density due to the appearance of the additional ionization layer. Generation of the drifting component BUM_D, as well as a decrease in the altitudes at which diagnostic pulses are reflected and the plasma line signal is generated, stops when the PW frequency f_0 becomes equal to $4f_{ce}(h_d)$ due to the strengthening of the magnetic field as the Earth is approached, i.e., at the double resonance altitude.

In the case of fast sweeping of the PW frequency f_0 (with speed $r_{f_0} = 5$ kHz s^{-1} $> r_f$) around $4f_{ce}$ in a range of $5930 \rightarrow 5730 \rightarrow 5930$ kHz (Fig. 36 [143]), the dynamic BUM_D feature corresponding to the additional ionization layer was generated fort $f_0 > 4f_{ce}$. The double resonance frequency $f_d = 4f_{ce}(h_d)$ in the background ionosphere, determined from the disappearance of the DM in the SEE spectrum, was $f_d = 5757$ kHz ($h_d \approx 205$ km), and the artificial ionization layer existed for $5800 < f_0 < 5900$ kHz by $\Delta h \simeq |(\Delta f_{BUM_S} - \Delta f_{BUM_D})(4df_{ce}/dh)^{-1}| \simeq 8-10$ km below the undisturbed 'main' layer. Shift Δh for $\Delta f_{BUM_S} >$ 30 kHz proved smaller than in the case of fixed frequency pumping, because the frequency drift velocity of the BUM

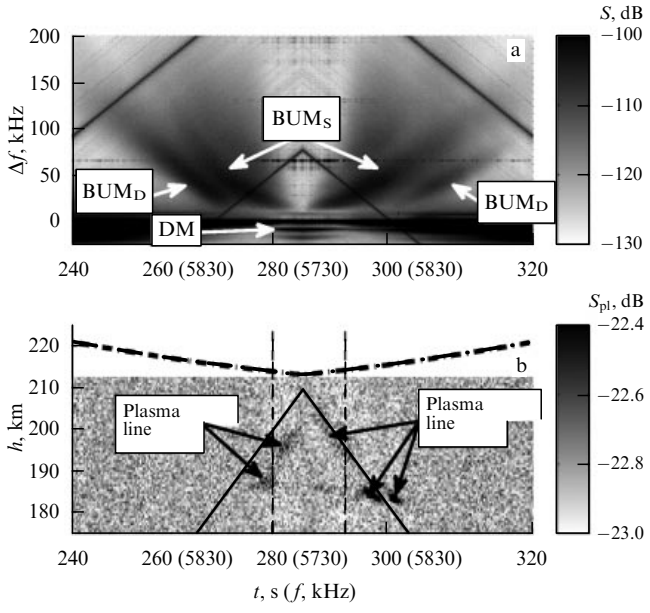

Figure 36. SEE spectrogram (a) and intensity of MUIR plasma line signal (b) depending on time and altitude h in the case of a fast PW frequency f_0 sweeping. 16:04:00–16:04:20 AST, 28.03.2011. Vertical dotted lines — double resonance frequency f_d. Dash-dotted line — plasma resonance ($f_0 = f_{pe}$) altitude in the background ionosphere. Solid black line in figure (b) — altitude of the 4th electron cyclotron resonance $f_0 = 4f_{ce}$; f_0 values are marked in parentheses.

peak (BUM_S and BUM_D) in the SEE spectrum in the thus designed experiment was determined by the PW frequency retuning rate r_{f_0}, much higher than the drift speed r_f at $f_0 = \text{const}$, and the artificial layer simply did not have enough time to reach h_d altitudes.

In the absence of BUM_D ($5730 < f_0 \lesssim 5800$ kHz), a plasma line signal could be recorded; the distance l to the region of its generation 'keeps watch' over l_{ce}, where $f_0(t) = 4f_{ce}(l_{ce}(t))$, $\Delta l = l - l_{ce} = \text{const}$ under changes of f_0 but takes different values as f_0 increases or decreases during sweeping. Similar effect, i.e., 'tracking' the altitude of multiple cyclotron resonance at $s = 2, f_0 \approx 2f_{ce}$ by the artificial ionization layer, was revealed in experiment [202] during a stepwise increase in f_0 by 5 kHz each 18 or 36 s within a range of 2.85–2.95 MHz. In certain sessions, the plasma frequency f_{pe} in the background ionosphere fell below f_0 and $[f_0^2 - f_{ce}^2]^{1/2}$, whereas it was never lower than $[f_0^2 - f_{ce}^2]^{1/2}$ in the artificial layer; in other words, PW upper-hybrid resonance invariably took place.

A few specific features of artificial layers at $f_0 \sim 4f_{ce}$ are worthy of note: (1) as f_0 passes through the double resonance frequency f_d of background plasma, the plasma line signal corresponding to the scattering from *Langmuir* waves disappears (Fig. 36), which suggests that the injection of energy into the plasma probably via the upper-hybrid mode sensitive to the f_0/f_d ratio [see formula (17) and the accompanying text]; (2) artificial layers emerge only if the directional pattern is oriented toward the magnetic zenith [38] but can be observed at $f_0 \sim 2f_{ce}$ even in the case of vertical pumping [202]; (3) descending layers can be seen only if the initial altitudes of PW–ionosphere interaction is $h \lesssim 200$ – 210 km, but are absent for $h \gtrsim 230$ km, and (4) under the 'cold start' conditions in the absence of striations, the initial distance l of plasma line generation region corresponds to the Langmuir resonance region $f_0 = f_{pe}$; the signal is recorded in the same region during transition from continuous pumping to an application of diagnostic pulses after the disappearance of the artificial plasma layer and striation relaxation.

Let us describe in brief the qualitative model of a descending layer in the form of the ionization wave front created by superthermal electrons accelerated by plasma turbulence [205].

Excitation of turbulence by a radio wave and acceleration of ionospheric electrons take place in a resonance region with plasma density N_e, which we denote by N_c. It is the plasma resonance region where $f_{pe} \approx f_0$ for Langmuir turbulence, and the region a few kilometers below with $f_0 \approx f_{UH}$ in the case of upper-hybrid turbulence. Let us assume that electrons are accelerated in the region of energies $\mathcal{E}_{min} \leqslant \mathcal{E} \lesssim \mathcal{E}_{max}$ and $\mathcal{E}_{max} \gg I_\gamma$ ($\mathcal{E}_{min} \approx \mathcal{E}_0$, $\mathcal{E}_{max} \sim \mathcal{E}^*$). Since electron motion is strongly influenced by a magnetic field, they escape the acceleration region along the magnetic field lines. Outside the acceleration region, they collide with neutral particles, and create a 'tongue' of freshly ionized plasma.

Let us denote the characteristic longitudinal ($\| \mathbf{B}_0$) size of the ionization area below the acceleration region by $L_\|$, and the time needed to reach plasma density N_c by τ_{ion}. The rate of ionization q_a is found from the equation

$$q_a = N_a \left\langle \nu_{ion}(\mathcal{E}) \right\rangle , \tag{39}$$

where $\nu_{ion}(\mathcal{E})$ is the ionization frequency, and $\langle ... \rangle$ stands for averaging over the distribution of accelerated electrons with density N_a.

At each temporal step t_i, ionization occurs near the plasma resonance altitude $h_c(t_i)$, where $N_e(h_c) = N_c$. The density altitude profile below h_c can be represented as

$$N_e(x, t_i) = N_c \, \Psi(x) , \tag{40}$$

where $x = z/L_\|$, $z = (h_c - h)/\cos\alpha_I$ is the distance along $\mathbf{B}_0$, α_I is the tilt angle of the geomagnetic field with respect to the vertical ($\sim 14^\circ$ for HAARP). Obviously, we have $z > 0$.

The monotonic function $\Psi(x)$ must satisfy self-explanatory conditions $\Psi(0) \geqslant 1$ and $\Psi(x) \to 0$ as $x \gg 1$, because background plasma density far from resonance is small: $N_0 \ll N_c$. The concrete form of $\Psi(x)$ is immaterial for qualitative estimates. Since the ratio $\delta_e(\mathcal{E})$ of inelastic collision frequencies (ν_{il}) to elastic ones (ν_{el}) turns out low, accelerated electrons undergo rapid isotropization in elastic collisions and $L_\| \simeq \langle l_{ion}(\delta_e/2)^{1/2} \rangle$, where $l_{ion} = v/\nu_{ion}$ is the ionization length.

Assuming that the ionization rate markedly exceeds recombination and diffusion losses, we obtain

$$N_e(x_i, t_{i+1}) = \int_{t_i}^{t_{i+1}} q_a(x_i, t') \, dt' \approx q_a(z_i) \, \Delta t_i . \tag{41}$$

Evidently, as soon as plasma density in a certain layer $x_i \leqslant 1$ amounts to N_c, a radio wave will excite turbulence in this layer, i.e., $h_c(t_{i+1}) \approx h_c(t_i) - xL_\|$. This condition and Eqns (39)–(41) determine ionization time, $\tau_{ion}^{-1} \approx q_a/N_c$, and ionization wave (front) velocity:

$$v_d = \left| \frac{dh_c}{dt} \right| \approx L_\| \tau_{ion}^{-1} \approx \left\langle v \sqrt{\frac{\delta_e}{2}} \right\rangle \frac{N_a}{N_c} . \tag{42}$$

Because $\langle \delta_e^{1/2} v \rangle \approx 1.5 \times 10^6$ m s^{-1}, it follows from formula (42) that v_d is equal to $v_{obs} \approx 300$ m s^{-1} at a small enough density of accelerated electrons, $N_a = N_a^{(d)} \approx 6 \times 10^{-4} N_c$.

It is worthwhile to note that front velocity (42) is unrelated to neutral gas density N_n, i.e., v_d does not vary with altitude if the same turbulence (therefore, the same distribution of accelerated electrons) is generated at each step. If this condition is violated, the descent speed changes even if the source remains unaltered. Specifically, a decrease in the longitudinal dimension of the turbulence region (acceleration) determined by ionization length $l_{ion} \sim N_n^{-1}$ needs to be considered at small enough altitudes. An equally important factor is inelastic losses limiting the maximum energy $\mathcal{E}_{max}$ at altitudes < 160 km [205]. At the same time, ionization efficiency must decrease essentially with increasing altitude of the resonance region, because the frequency of ionizing collisions $\propto N_n$ decreases with altitude h.

6. Modification of electron concentration profile in the vicinity of pump wave plasma resonances

It was shown in Section 5.3 that PW-induced changes to electron concentration N_e in the F-region ionosphere can be related first to ionization–recombination disbalance in the lower ionosphere due to electron heating (dissociative recombination coefficient $\alpha \propto T_e^{-1/2}$), which causes a rise in N_e and, as a result, defocusing lens formation for radio waves [200]. Second, N_e can grow under the effect of main neutral component ionization in collisions with electrons accelerated by HF plasma turbulence [24] (see Section 5.3). Third, electron heating by plasma waves and HF pressure of a

plasma wave in the upper (F-region) ionosphere result in the extrusion of the plasma from the PlW localization region [206–208], i.e., the region between the PW reflection altitude h_r with $f_0 \simeq f_{pe}$ and the region slightly below the PW UHR, where $f_0 = f_{UH} = (f_{pe} + f_{ce})^{1/2}$. This causes a noticeable decrease in N_e especially in the PW UHR region [27, 199, 209].

Modification of the electron number density profile $N_e(h)$ in the disturbed ionospheric region is explored by means of multifrequency Doppler sounding (MDS) [210] by a set of probing radio waves with different frequencies. Analyzing phase characteristics of probing signals reflected from the disturbed region allows the $N_e(h)$ profile to be retrieved. The altitude resolution of the restored density profile directly depends on the frequency shift between 'neighboring' probing waves, while their frequency range determines the altitude range in the retrieved profile. In the first MDS experiments [27, 198, 199, 209], their number did not exceed eight.

The modified MDS method [66] employed since 2006 permits significantly increasing the resolution of the retrieved profile and obtaining a deeper insight into the dynamics of its modification by using emission of the Sura facility not only for pumping but also for sounding in specially combined regimes of pumping and sounding (see Introduction, diagnostic schedule 3). In this case, sounding radiation is a sequence of short radio pulses (20–200 μs). Registration of a radio pulse reflected from the ionosphere by modern broadband receivers makes it possible to distinguish spectral components in a waveband up to 1 MHz against the background noises. These spectral components play the role of probing waves. The use of regularization algorithms allows us to adequately take account of geomagnetic field effects for the solution of the inverse problem. As a result, the method permits reaching the following parameters of the retrieved $N_e(h, t)$ profile: altitude resolution ~ 50 m, altitude range 30 km, and time resolution 100–200 ms.

In the Sura experiments of 2008 and 2010 [29, 211], plasma expulsion (a decrease in $N_e(h)$) from the plasma resonance regions during PW irradiation was revealed. In 2014, analogous experiments were conducted at the HAARP facility using a PW power an order of magnitude higher [95]. Their results are presented in Figs 37 and 38. It follows from Fig. 37 that plasma begins to be expelled from the PW reflection region ~ 1 s after PW turn-on. More pronounced expulsion starts to proceed within the next 2–3 s from the PW

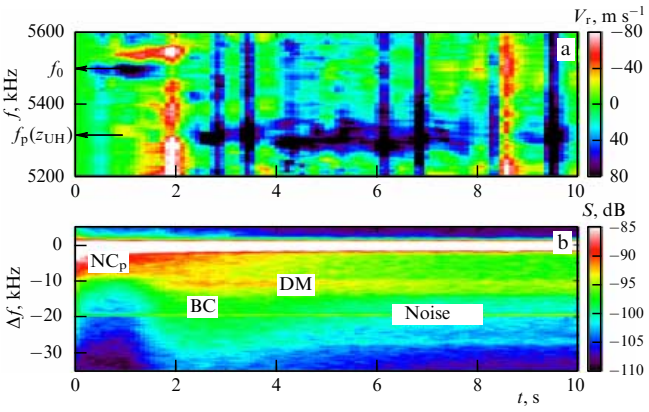

Figure 37. (Color online.) Time and frequency dependences of the velocity V_r of probing wave reflection point (a) for a heating session started at the moment $t = 0$; $V_r > 0$ corresponds to downward motion. (b) SEE spectrogram for the same session. The narrow continuum, downshifted maximum, and broad continuum spectral features are distinguished [95].

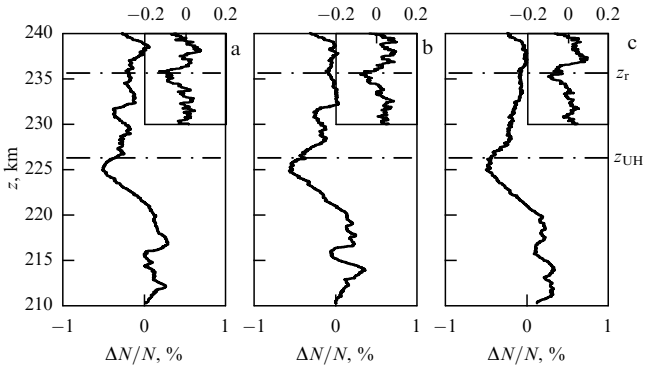

Figure 38. Altitude dependences of relative variations of electron number density $[N(t) - N(0)]/N(0)$ within 2.4 s (inserts to figures a-c) and 30 s (a–c) after the heating switch-on; z_r and z_{UH} correspond to the altitudes of reflection and UHR of the PW, respectively [95].

UHR region. The speed of the vertical motion of the probing wave reflection level amounts to ± 100 m s^{-1}. The resulting reduction in the electron density in the UHR regions reached 0.5–0.7% during 30-s heating (Fig. 38). The plasma is forced back into the UHR region 15–30 s after cessation of heating. It follows from Fig. 37b that the beginning of plasma expulsion from the PW reflection region coincides with the appearance of the NC$_p$ feature in SEE spectra, whereas the DM and BC features emerge simultaneously with the onset of the plasma expulsion from the PW UHR region, while the NC$_p$ component is suppressed (overshoot effect). This means that the expulsion of the plasma from the PW reflection region and NC$_p$ generation are related to PPI excitation at the early stage of pumping, whereas slower processes in the UHR region (thermal parametric and resonant instabilities) leading to the striation formation and the generation of the BC and DM features shield the reflection point, and pump energy input occurs in the UHR region.

7. Conclusions

The present review is focused on the analysis of results of research dealing with phenomena in the ionosphere that result from its pumping by powerful HF radio waves with O-polarization in the plasma resonance region.

The review includes data obtained for the most part with the direct involvement of the authors. The diagnostic schemes of pumping described in the review were developed elsewhere to investigate the dynamic characteristics of AIT by measuring PW and SEE signals reflected from the ionosphere at the initial and intermediate stages of low duty cycle PW pulse irradiation, to study thermal parametric (upper-hybrid) turbulence in the regime of alternating quasicontinuous and pulsed PW radiation (by measuring SEE), to characterize the dependence of SEE properties on the relationship between PW frequency and electron gyroharmonics in the absence of striations and at the high stationary level of the striation intensity (by sweeping f_0 in the vicinity of sf_{ce}), to detect descending artificial ionization layers with the use of ionosondes and optical airglow of the ionosphere (at $f_0 \sim 2f_{ce}$), SEE, probing waves, and the MUIR radar (at $f_0 \sim 4f_{ce}$), to determine the position and structure of the stimulated ionospheric airglow spot, to elucidate brightness dynamics of the airglow upon pumping, and to observe plasma expulsion from plasma resonance regions. We

confined ourselves to a concise exposition of theoretical models of AIT used to interpret experimental data.

Unfortunately, the results of research concerning the dependence of SEE generation efficiency on the difference $(f_0 - f_{DW})$ between the frequencies of the pump wave and diagnostic pulsed wave with low average power that allow the study of the altitude structure of the disturbed ionospheric region starting from its center, where the PW energy inputs to the plasma near the UHR level, to the periphery, where diagnostic SEE is generated in the vicinity of diagnostic wave UHR have to be left beyond the scope of this publication. The same is true of the data on SEE generated by short diagnostic pulses having a duration of $\tau_p \ll \tau_1, \tau_{prop}$ (τ_{prop} is the time of diagnostic pulse propagation up to the reflection point and back). They will be reported in separate articles [30, 212]. We did not give due attention to the analysis of the magnetic zenith effect, with the exception of Section 5, where results of the Sura experiments on stimulated ionospheric airglow and those of the HAARP heating facility on descending artificially ionized layers are presented. This issue is addressed in more detail in review [3], where references to the relevant literature can be found. Such problems as transillumination of the disturbed ionosphere by satellite radio signals, detection of upward ionospheric ion flows and artificial density ducts in the upper ionosphere revealed from the satellite measurements, and amplification of effects by X-polarized pumping waves with frequencies close to critical ones are not discussed either.

The list of these matters in itself illustrates the abundance and diversity of the processes in the ionospheric plasma resonance region responsible for the development of artificial ionospheric turbulence and emphasizes the necessity of using the ionosphere as a natural laboratory for the investigation of linear and nonlinear phenomena in the collisional magnetized plasma and effects of its exposure to high-power high-frequency electromagnetic radiation. Various aspects of such a use were considered in reviews [3, 64, 213].

It should be emphasized that the physical picture of processes proceeding in the disturbed ionospheric region is far from complete. Only part of the experimental data obtained with the HAARP facility in 2009–2014 have been analyzed and published. The physical nature of effects produced by the action of a high-power ($\sim$ 500 MW) PW with X-polarization and the frequency close to a critical one, is still unclear, and the causes behind the association between areas of PW energy input into the plasma and the altitude of multiple cyclotron resonance, as well as many other issues, remain to be elucidated. Despite considerable progress in numerical simulations of the processes in the PW-modified ionosphere, their results are yet far from direct comparison with experimental data. On the other hand, concepts in the framework of the weak turbulence approximation providing a basis for the development of efficient diagnostic schemes are beyond the scope of the theory applicability.

It is interesting to note that during the long period of AIT studies (around 45 years), new reports on previously unknown effects associated with AIT excitation appeared roughly at a rate of one every 10 years and every time caused a surge of interest on the part of researchers. It is probably a result of 'interference' of technical progress (enhancement of pumping power and extension of the diagnostic potential, in the first place with the advent of modern radio receiving and optical instruments) with solar cycles (the most interesting findings have coincided with periods of near-maximum solar activity). For example, the first experiments in the early 1970s demonstrated the generation of different-scaled striations, the early 1980s brought about the observation of SEE generation, the strong dependence of most AIT parameters on the proximity of PW frequency f_0 to electron gyroharmonics sf_{ce} was reported in the late 1980s – early 1990s, the magnetic zenith effect, i.e., the marked enhancement of AIT under the effect of PW irradiation along the magnetic field, was discovered in the early 2000s, and the appearance of artificial ionization layers in the ionosphere and unusually strong effects of X-polarization were documented on the cusp between the 2000s and the 2010s.

Acknowledgments

The work in Sections 1, 2.1, 4.3, and 5.3 of this review was conducted under the State Assignment No. 3.1252.2914/k with the support from RFBR grant No. 16-02-00798 and the Air Force Office of Scientific Research. The work expounded in Sections 2.2, 3, 4.1, 4.2, 5.1, 5.2, and 7 was supported by RSF grant No. 14-12-00706, and in Section 6 by RFBR grant No. 16-32-60176.

References

1. Ginzburg V L, Gurevich A V *Sov. Phys. Usp.* **3** 115 (1960); *Usp. Fiz. Nauk* **70** 201 (1960)
2. Gurevich A V *Nonlinear Phenomena in the Ionosphere* (Physics and Chemistry in Space, Vol. 10) (Berlin: Springer-Verlag, 1978); Gurevich A V, Shvartsburg A B *Nelineinaya Teoriya Rasprostraneniya Radiovoln v Ionosfere* (Non-Linear Theory of Radiowave Propagation in the Ionosphere) (Moscow: Nauka, 1973)
3. Gurevich A V *Phys. Usp.* **50** 1091 (2007); *Usp. Fiz. Nauk* **177** 1145 (2007)
4. Mityakov N A, in *Pervyi v Strane Radiofizicheskii Institut: Ot Sozdaniya do Nashikh Dnei* (The First Radiophysical Institute in the Country: from Foundation to Nowadays) (Nizhny Novgorod: Radiophysical Research Institute, 2016) p. 124
5. Utlaut W F, Cohen R *Science* **174** 245 (1971)
6. Wong A Y, Taylor R J *Phys. Rev. Lett.* **27** 644 (1971)
7. Minkoff J, Kugelman P, Weissman I *Radio Sci.* **9** 941 (1974)
8. Fialer P A *Radio Sci.* **9** 923 (1974)
9. Bowhill S À *Radio Sci.* **9** 975 (1974)
10. Erukhimov L M et al., in *Teplovye Nelineinye Yavleniya v Plazme* (Thermal Nonlinear Phenomena in Plasma) (Exec. Ed. V Yu Trakhtengerts) (Gorky: IPF AN SSSR, 1979) p. 7
11. Getmantsev G G et al. *JETP Lett.* **20** 101 (1974); *Pis'ma Zh. Eksp. Teor. Fiz.* **20** 229 (1974)
12. Belikovich V V et al. *JETP Lett.* **22** 243 (1975); *Pis'ma Zh. Eksp. Teor. Fiz.* **22** 497 (1975)
13. Kotik D S, Trakhtengerts V Yu *JETP Lett.* **21** 51 (1975); *Pis'ma Zh. Eksp. Teor. Fiz.* **21** 114 (1975)
14. Perkins F W *Radio Sci.* **9** 1065 (1974)
15. Vas'kov V V, Gurevich A V *Sov. Phys. JETP* **42** 91 (1975); *Zh. Eksp. Teor. Fiz.* **69** 176 (1975)
16. Grach S M, Trakhtengerts V Yu *Radiophys. Quantum Electron.* **18** 951 (1975); *Izv. Vyssh. Ucheb. Zaved. Radiofiz.* **18** 1288 (1975)
17. Ginzburg V L *The Propagation of Electromagnetic Waves in Plasmas* (Oxford: Pergamon Press, 1970); Translated from Russian: *Rasprostranenie Elektromagnitnykh Voln v Plazme* (Moscow: Nauka, 1967)
18. Silin V P *Parametricheskoe Vozdeistvie Izlucheniya Bol'shoi Moshchnosti na Plazmu* (Parametric Effects of High-Power Radiation on the Plasma) (Moscow: Nauka, 1973)
19. Vas'kov V V, Gurevich A V *Radiophys. Quantum Electron.* **16** 138 (1973); *Izv. Vyssh. Ucheb. Zaved. Radiofiz.* **16** 188 (1973)
20. Perkins F W, Valeo C R, Oberman E J *J. Geophys. Res.* **79** 1478 (1974)
21. Mityakov N A, Rapoport V O, Trakhtengerts V Yu *Geomagn. Aeronom.* **14** 36 (1974)

22. Mityakov N A, Rapoport V O, Trakhtengerts V Yu *Radiophys. Quantum Electron.* **18** 18 (1975); *Izv. Vyssh. Ucheb. Zaved. Radiofiz.* **18** 27 (1975)
23. Fejer J A *Rev. Geophys. Space Phys.* **17** 135 (1979)
24. Vas'kov V V et al. *JETP Lett.* **34** 558 (1981); *Pis'ma Zh. Eksp. Teor. Fiz.* **34** 582 (1981)
25. Erukhimov L M et al. *Radiophys. Quantum Electron.* **30** 156 (1987); *Izv. Vyssh. Ucheb. Zaved. Radiofiz.* **30** 208 (1987)
26. Nasyrov A M *Rasseyanie Radiovoln Anizotropnymi Ionosfernymi Neodnorodnostyami* (Scattering of Radiowaves by Anisotropic Ionospheric Irregularities) (Kazan: Izd. Kazan. Univ., 1991)
27. Vas'kov V V et al. *JETP Lett.* **43** 663 (1986); *Pis'ma Zh. Eksp. Teor. Fiz.* **43** 512 (1986)
28. Vas'kov V V et al. "Issledovanie effektov iskusstvennoi ionizatsii ionosfery v pole moshchnykh radiovoln" ("Investigations into effects of artificial ionospheric ionization in the field of powerful radiowaves"), Preprint No. 5 (469) (Moscow: IZMIRAN, 1984) p. 5
29. Shindin A, Sergeev E, Grach S *Radio Sci.* **47** RS0N04 (2012)
30. Sergeev E N, Grach S M *Radiophys. Quantum Electron.* **60** (2) (2017) in press; *Izv. Vyssh. Ucheb. Zaved. Radiofiz.* **60** (2) (2017) in press
31. Milikh G et al. *Geophys. Res. Lett.* **35** L22102 (2008)
32. Tereshchenko E D et al. *Radiophys. Quantum Electron.* **51** 842 (2008); *Izv. Vyssh. Ucheb. Zaved. Radiofiz.* **51** 934 (2008)
33. Frolov V L et al. *Radiophys. Quantum Electron.* **53** 379 (2010); *Izv. Vyssh. Ucheb. Zaved. Radiofiz.* **53** 421 (2010)
34. Ryabov A V et al. *Radiophys. Quantum Electron.* **54** 441 (2011); *Izv. Vyssh. Ucheb. Zaved. Radiofiz.* **54** 485 (2011)
35. Thidé B, Kopka H, Stubbe P *Phys. Rev. Lett.* **49** 1561 (1982)
36. Leyser T B *Space Sci. Rev.* **98** 223 (2001)
37. Pedersen T et al. *Geophys. Res. Lett.* **37** L02106 (2010)
38. Sergeev E et al. *Phys. Rev. Lett.* **110** 065002 (2013)
39. Milikh G N et al. *Geophys. Res. Lett.* **35** L17104 (2008)
40. Frolov V L et al. *JETP Lett.* **88** 790 (2008); *Pis'ma Zh. Eksp. Teor. Fiz.* **88** 908 (1988)
41. Milikh G N et al. *Geophys. Res. Lett.* **37** L18102 (2010)
42. Blagoveshchenskaya N F et al. *J. Atmos. Sol. Terr. Phys.* **105 – 106** 231 (2013)
43. Blagoveshchenskaya N F et al. *J. Geophys. Res. Space Phys.* **119** 10483 (2014)
44. Blagoveshchenskaya N F et al. *J. Atmos. Sol. Terr. Phys.* **135** 50 (2015)
45. Frolov V L et al. *J. Atm. Sol. Terr. Phys.* **59** 2317 (1997)
46. Mityakov N A, Grach S M, Mityakov S N *Vozmushchenie Ionosfery Moshchnymi Radiovolnami* (Disturbance of Ionosphere by Powerful Radiowaves) (Results of Science and Technology, Ser. Geomagnetism and High Layers of the Atmosphere, Vol. 9) (Moscow: VINITI, 1989)
47. Frolov V L et al. *Phys. Usp.* **50** 315 (2007); *Usp. Fiz. Nauk* **177** 330 (2007)
48. Gustavsson B et al. *Ann. Geophys.* **23** 1747 (2005)
49. Erukhimov L M, Metelev S A, Razumov D V *Radiophys. Quantum Electron.* **31** 928 (1988); *Izv. Vyssh. Ucheb. Zaved. Radiofiz.* **31** 1301 (1988)
50. Carozzi T D et al. *J. Geophys. Res.* **107** (A9) 1253 (2002)
51. Sergeev E N et al. *Radiophys. Quantum Electron.* **45** 193 (2002); *Izv. Vyssh. Ucheb. Zaved. Radiofiz.* **45** 214 (2002)
52. Thidé B et al. *Phys. Rev. Lett.* **95** 255002 (2005)
53. Norin L et al. *J. Geophys. Res.* **112** A09303 (2007)
54. Norin L et al. *J. Geophys. Res.* **113** A09314 (2008)
55. Kotov P V *Adv. Space Res.* **40** 377 (2007)
56. Norin L et al. *Phys. Rev. Lett.* **102** 065003 (2009)
57. Bernhardt P A et al. *Phys. Rev. Lett.* **104** 165004 (2010)
58. Grach S M et al. *Radiophys. Quantum Electron.* **51** 499 (2008); *Izv. Vyssh. Ucheb. Zaved. Radiofiz.* **51** 553 (2008)
59. Kosch M J et al. *Adv. Space Res.* **40** 365 (2007)
60. Gurevich A V, Shlyuger I S *Radiophys. Quantum Electron.* **18** 913 (1975); *Izv. Vyssh. Ucheb. Zaved. Radiofiz.* **18** 1237 (1975)
61. Vas'kov V V, Gurevich A V, in *Teplovye Nelineinye Yavleniya v Plazme* (Thermal Nonlinear Phenomena in Plasma) (Exec. Ed. V Yu Trakhtengerts) (Gorky: IPF AN SSSR, 1979) p. 81
62. Grach S M et al., in *Teplovye Nelineinye Yavleniya v Plazme* (Thermal Nonlinear Phenomena in Plasma) (Exec. Ed. V Yu Trakhtengerts) (Gorky: IPF AN SSSR, 1979) p. 46
63. Robinson T R *Phys. Rep.* **179** 79 (1989)
64. Stubbe P, Hagfors T *Surv. Geophys.* **18** 57 (1997)
65. Belikovich V V et al. *Radiophys. Quantum Electron.* **50** 497 (2007); *Izv. Vyssh. Ucheb. Zaved. Radiofiz.* **50** 545 (2007)
66. Sergeev E N et al. *Radiophys. Quantum Electron.* **50** 593 (2007); *Izv. Vyssh. Ucheb. Zaved. Radiofiz.* **50** 649 (2007)
67. Djuth F T, DuBois D F *Earth, Moon, Planets* **116** 19 (2015)
68. Gaponov A V, Miller M A *Sov. Phys. JETP* **7** 168 (1958); *Zh. Eksp. Teor. Fiz.* **34** 242 (1958)
69. Galeev A A, Sagdeev R Z, in *Review of Plasma Physics* Vol. 7 (Ed. M A Leontovich) (New York: Consultants Bureau, 1979); Translated from Russian: *Voprosy Teorii Plazmy* Iss. 7 (Ed. M A Leontovich) (Moscow: Atomizdat, 1973) p. 3
70. Al'ber Ya I et al. *Sov. Phys. JETP* **39** 275 (1974); *Zh. Eksp. Teor. Fiz.* **66** 574 (1974)
71. Lundborg B, Thidé B *Radio Sci.* **20** 947 (1985)
72. Lundborg B, Thidé B *Radio Sci.* **21** 486 (1986)
73. Eliasson B *Mod. Phys. Lett. B* **27** 1330005 (2013)
74. Mishin E et al. *J. Geophys. Res. Space Phys.* **121** 3497 (2016)
75. Shapiro V D, Shevchenko V I, in *Basic Plasma Physics* Vol. 2 (Eds A A Galeev, R N Sudan) (Amsterdam: North-Holland, 1984); *Osnovy Fiziki Plazmy* (Eds A A Galeev, R Sudan) Vol. 2 (Moscow: Energoatomizdat, 1984) p. 119
76. Sheerin J P et al. *J. Atm. Terr. Phys.* **44** 1043 (l982)
77. Galeev A A, Sagdeev R Z, in *Basic Plasma Physics* Vol. 1 (Eds A A Galeev, R N Sudan) (Amsterdam: North-Holland, 1983); *Osnovy Fiziki Plazmy* Vol. 1 (Eds A A Galeeva, R Sudana) (Moscow: Energoatomizdat, 1983) p. 590
78. Zakharov V E, in *Basic Plasma Physics* Vol. 2 (Eds A A Galeev, R N Sudan) (Amsterdam: North-Holland, 1984); *Osnovy Fiziki Plazmy* Vol. 2 (Eds A A Galeev, R Sudan) (Moscow: Energoatomizdat, 1984)
79. Hanssen A et al. *J. Geophys. Res.* **97** 12073 (1992)
80. Vladimirov S V, Popel S I *Phys. Rev. E* **51** 2390 (1995)
81. DuBois D F et al. *Phys. Plasmas* **8** 791 (2001)
82. Mjølhus E, Helmersen E, DuBois D F *Nonlinear Proc. Geophys.* **10** 151 (2003)
83. Mjølhus E, Hanssen A, DuBois D F *J. Geophys. Res.* **100** 17527 (1995)
84. Eliasson B, Stenflo L *J. Plasma Phys.* **76** 369 (2010)
85. Frolov V L et al. *J. Geophys. Res.* **109** A07304 (2004)
86. Erukhimov L M et al. *Radiophys. Quantum Electron.* **25** 348 (1982); *Izv. Vyssh. Ucheb. Zaved. Radiofiz.* **25** 490 (1982)
87. Sergeev E N et al. *Radiophys. Quantum Electron.* **41** 206 (1998); *Izv. Vyssh. Ucheb. Zaved. Radiofiz.* **41** 313 (1998)
88. Sergeev E N, Grach S M, Kotov P V *Radiophys. Quantum Electron.* **47** 185 (2004); *Izv. Vyssh. Ucheb. Zaved. Radiofiz.* **47** 209 (2004)
89. Sergeev E N et al., in *Rasprostranenie Radiovoln. Trudy XXIV Vseros. Nauchn. Konf. RRV-24. Irkutsk, 29 Iyunya–5 Iyulya 2014 g.* (The Propagation of Radiowaves. Proc. of the XXIV All-Russian Scientific Conf. PRW-24, Irkutsk, Russia, June 29 – July 5, 2014) Vol. 3 (Irkutsk: ISZF SO RAN, 2014) p.71
90. Stubbe P, Kohl H, Rietveld M T *J. Geophys. Res.* **97** 6285 (1992)
91. Djuth F T et al. *J. Geophys. Res.* **109** A11307 (2004)
92. Kotov P V, Sergeev E N, Grach S M *Radiophys. Quantum Electron.* **51** 417 (2008); *Izv. Vyssh. Ucheb. Zaved. Radiofiz.* **51** 461 (2008)
93. Bareev D D et al. *Adv. Space Res.* **57** 802 (2016)
94. Sergeev E N et al. *Adv. Space Res.* **15** (12) 63 (1995)
95. Sergeev E N et al. *Radio Sci.* **51** 1118 (2016)
96. Kohl H et al. *Radio Sci.* **22** 655 (1987)
97. Bernhardt P A, Selcher S A, Kowtha S *Geophys. Res. Lett.* **38** L19107 (2011)
98. Bernhardt P A et al. *Ann. Geophys.* **27** 4409 (2009)
99. Dimant Ya S *Radiophys. Quantum Electron.* **20** 1259 (1977); *Izv. Vyssh. Ucheb. Zaved. Radiofiz.* **20** 1834 (1977)
100. Braginskii S I, in *Review of Plasma Physics* Vol. 1 (Ed. M A Leontovich) (New York: Consultants Bureau, 1965); Translated from Russian: *Voprosy Teorii Plazmy* Iss. 1 (Ed. M A Leontovich) (Moscow: Gosatomizdat, 1963) p. 57
101. Grach S M et al. *Sov. J. Plasma Phys.* **4** 737 (1978); *Fiz. Plazmy* **4** 1321 (1978)
102. Gurevich A V, Tsedilina E E *Sov. Phys. Usp.* **10** 214 (1967); *Usp. Fiz. Nauk* **91** 609 (1967)

103. Gershman B N *Dinamika Ionosfernoi Plazmy* (Dynamics of Ionospheric Plasma) (Moscow: Nauka, 1974)
104. Rozhanskii V A, Tsendin L D *Sov. J. Plasma Phys.* **3** 217 (1977); *Fiz. Plazmy* **5** 382 (1977)
105. Vas'kov V V, in *Vzaimodeistvie Radiovoln KV- i UKV-Diapazonov s Ionosfernoi Plazmoi* (The Interaction of HF and VHF Radiowaves with the Ionospheric Plasma) (Moscow: IZMIRAN, 1980) p. 4
106. Vas'kov V V, Gurevich A V *Geomagn. Aeronom.* **22** 565 (1982)
107. Vas'kov V V, Gurevich A V *Geomagn. Aeronom.* **23** 901 (1983)
108. Erukhimov L M, Myasnikov E N *Radiophys. Quantum Electron.* **41** 125 (1998); *Izv. Vyssh. Ucheb. Zaved. Radiofiz.* **41** 194 (1998)
109. Grach S M *Radiophys. Quantum Electron.* **22** 357 (1979); *Izv. Vyssh. Ucheb. Zaved. Radiofiz.* **22** 521 (1979)
110. Grach S M, Thidé B, Leyser T B *Radiophys. Quantum Electron.* **37** 392 (1994); *Izv. Vyssh. Ucheb. Zaved. Radiofiz.* **37** 617 (1994)
111. Leyser T B et al. *J. Geophys. Res. A* **99** 19555 (1994)
112. Norin L, Grach S M, Thidé B *Adv. Space Res.* **38** 2527 (2006)
113. Grach S M *Radiophys. Quantum Electron.* **28** 470 (1985); *Izv. Vyssh. Ucheb. Zaved. Radiofiz.* **28** 684 (1985)
114. Grach S M et al. *J. Atm. Sol. Terr. Phys.* **60** 1233 (1998)
115. Grach S M et al. *Radiophys. Quantum Electron.* **20** 1254 (1977); *Izv. Vyssh. Ucheb. Zaved. Radiofiz.* **20** 1827 (1977)
116. Grach S M et al. *Sov. J Plasma Phys.* **4** 742 (1978); *Fiz. Plazmy* **4** 1330 (1978)
117. Grach S M et al. *Physica D* **2** 102 (1981)
118. Litvak A G, Mironov G A *Sov. Phys. JETP* **51** 282 (1980); *Zh. Eksp. Teor. Fiz.* **76** 561 (1980)
119. Mjølhus E *J. Plasma Phys.* **58** 747 (1997)
120. Porkolab M, Goldman M N *Phys. Fluids* **18** 872 (1976)
121. Burinskaya T M *Sov. J. Plasma Phys.* **5** 819 (1979); *Fiz. Plazmy* **5** 819 (1979)
122. Gorshkov K A, Mironov V A, Sergeev A M "Svyazannye statsionarnye solitonnye obrazovaniya" ("Bound stationary soliton structures"), Preprint No. 49 (Gorky: IAP AS USSR, 1982)
123. Litvak A G, Sergeev A M, in *Vysokochastotnyi Nagrev Plazmy. Materialy Vsesoyuz. Soveshchaniya Gor'ky 21–25 Iyunya 1982 g.* (High-Frequency Plasma Heating. Proc. of the All-Union Meeting, Gorky, 21–25 June 1982) (Exec. Ed. A G Litvak) (Gorky: IAP AS USSR, 1983) p. 324
124. Istomin Ya N, Leyser T B *Phys. Plasmas* **4** 817 (1997)
125. Gurevich A V et al. *Phys. Lett. A* **231** 97 (1997)
126. Kelley M C et al. *J. Geophys. Res.* **100** (17) 367 (1995)
127. Franz T L, Kelley M C, Gurevich A V *Radio Sci.* **34** 465 (1999)
128. Avdeev V B et al. *Radiophys. Quantum Electron.* **37** 299 (1994); *Izv. Vyssh. Ucheb. Zaved. Radiofiz.* **37** 479 (1994)
129. Boiko G N, Erukhimov L M, Frolov V L *Geomagn. Aeronom.* **30** 998 (1990)
130. Gurevich A V et al. *Phys. Lett. A* **239** 385 (1998)
131. Sergeev E N et al. *Radiophys. Quantum Electron.* **42** 715 (1999); *Izv. Vyssh. Ucheb. Zaved. Radiofiz.* **42** 810 (1999)
132. Ponomarenko P V, Leyser T B, Thidé B *J. Geophys. Res. A* **5** 10081 (1999)
133. Blagoveshchenskaya N F et al. *Ann. Geophys.* **24** 2333 (2006)
134. Belikovich V V, Benediktov E A, Grach S M, Terina G I, in *XIII Vsesoyuz. Konf. po Rasprostraneniyu Radiovoln, Gor'ky, 1981 g. Tezisy Dokladov* (XIII All-Union. Conf. on the Propagation of Radiowaves, Gorky, 1981. Abstracts) Ch. 1 (Moscow: Nauka, 1981) p. 107
135. Terina G I *J. Atm. Terr. Phys.* **57** 273 (1995)
136. Leyser T B et al. *J. Geophys. Res. A* **98** (A10) 17597 (1993)
137. Sergeev E N, Frolov V L, Grach S M, Kotov P V *Adv. Space Res.* **38** 518 (2006)
138. Frolov V L et al. *Geophys. Res. Lett.* **28** 3103 (2001)
139. Grach S *J. Geophys. Res. Space Phys.* **120** 666 (2015)
140. Frolov V L et al. *Phys. Rev. Lett.* **81** 1630 (1998)
141. Shvarts M M, Grach S M *J. Atmos. Sol. Terr. Phys.* **59** 2421 (1997)
142. Sergeev E N et al. *Radiophys. Quantum Electron.* **42** 544 (1999); *Izv. Vyssh. Ucheb. Zaved. Radiofiz.* **42** 619 (1999)
143. Grach S M et al. *Dokl. Phys.* **59** 62 (2014); *Dokl. Ross. Akad. Nauk* **59** 526 (2014)
144. Vas'kov V V, Puchkov V A *Fiz. Plazmy* **16** 1359 (1990)
145. Goodman S, Thidé B, Erukhimov L M *Geophys. Res. Lett.* **20** 735 (1993)
146. Tripathi V K, Liu C S *J. Geophys. Res. A* **98** 1719 (1993)
147. Huang J, Kuo S P *J. Geophys. Res.* **99** 2173 (1994)
148. Grach S M *Radiophys. Quantum Electron.* **42** 572 (1999); *Izv. Vyssh. Ucheb. Zaved. Radiofiz.* **42** 651 (1999)
149. Zheleznyakov V V, Zlotnik E Ya *Solar Phys.* **43** 431 (1975)
150. Yoon P H et al. *J. Geophys. Res.* **101** 27015 (1996)
151. Istomin Ya N, Leyser T B *Phys. Plasmas* **5** 921 (1998)
152. Mjølhus E *J. Geophys. Res.* **103** 14711 (1998)
153. Stubbe P et al. *J. Geophys. Res.* **89** 7523 (1984)
154. Stubbe P, Kopka H *Phys. Rev. Lett.* **65** 183 (1990)
155. Frolov V L et al. *Radiophys. Quantum Electron.* **39** 241 (1996); *Izv. Vyssh. Ucheb. Zaved. Radiofiz.* **39** 241 (1996)
156. Fu H Y et al. *Ann. Geophys.* **33** 983 (2015)
157. Shindin A V, Grach S M, Sergeev E N, in *Vos'maya Ezhegodnaya Konf. "Fizika Plazmy v Solnechnoi Sisteme", IKI RAN, 4–8 Fevralya 2013 g.* (Eighth Annual Conf. "The Physics of Plasma in the Solar System", Space Research Institute RAS, 4–8 February 2013) (Moscow: Space Research Institute RAS, 2013) p. 87
158. Boiko G N et al. *Radiophys. Quantum Electron.* **28** 259 (1985); *Izv. Vyssh. Ucheb. Zaved. Radiofiz.* **28** 395 (1985)
159. Thidé B et al. *Radio Sci.* **18** 851 (1983)
160. Sergeev E N, Grach S M *Radiophys. Quantum Electron.* **57** 81 (2014); *Izv. Vyssh. Ucheb. Zaved. Radiofiz.* **57** 89 (2014)
161. Starodubtsev M V et al. *Radiophys. Quantum Electron.* **52** 796 (2009); *Izv. Vyssh. Ucheb. Zaved. Radiofiz.* **52** 881 (2009)
162. Ashrafi M et al. *J. Geophys. Res.* **112** A05314 (2007)
163. Gurevich A V, Zybin K P *Phys. Lett. A* **358** 159 (2006)
164. Sergeev E N, Boiko G N, Frolov V L *Radiophys. Quantum Electron.* **37** 495 (1994); *Izv. Vyssh. Ucheb. Zaved. Radiofiz.* **37** 763 (1994)
165. Ermakova E N, Trakhtengerts V Yu *Adv. Space Res.* **15** (12) 67 (1995)
166. Grach S M et al *Ann. Geophys.* **20** 1687 (2002)
167. Weinstock J *J. Geophys. Res.* **80** 4331 (1975)
168. Galeev A A et al. *Sov. Phys. JETP* **46** 711 (1977); *Zh. Eksp. Teor. Fiz.* **73** 1352 (1977)
169. Robinson P A *Rev. Mod. Phys.* **69** 507 (1997)
170. Eliasson B et al. *J. Geophys. Res.* **117** A10321 (2012)
171. Eliasson B et al. *J. Plasma Phys.* **81** 415810201 (2015)
172. Vas'kov V V, Gurevich A V, Dimant Ya S *Sov. Phys. JETP* **57** 310 (1983); *Zh. Eksp. Teor. Fiz.* **84** 536 (1983)
173. Gurevich A V et al. *J. Atm. Terr. Phys.* **47** 1057 (1985)
174. Dimant Ya S, Gurevich A V, Zybin K P *J. Atm. Terr. Phys.* **54** 425 (1992)
175. Vas'kov V V, Milikh G M *Geomagn. Aeronom.* **23** (2) 196 (1983)
176. Grach S M, Mityakov N A, Trakhtengerts V Yu *Radiophys. Quantum Electron.* **27** 766 (1984); *Izv. Vyssh. Ucheb. Zaved. Radiofiz.* **27** 1086 (1984)
177. Grach S M, Mityakov N A, Trakhtengerts V Yu *Fiz. Plazmy* **12** 693 (1986)
178. Bespalov P A, Trakhtengerts V Yu *Sov. Phys. JETP* **40** 480 (1975); *Zh. Eksp. Teor. Fiz.* **67** 969 (1974)
179. Najmi A et al. *Radio Sci.* **51** 704 (2016)
180. Balikhin M, Gedalin M, Petrukovich A *Phys. Rev. Lett.* **70** 1259 (1993)
181. Bernhardt P A, Tepley C A, Duncan L M *J. Geophys. Res.* **94** 9071 (1989)
182. Mantas G P, Carlson H C *J. Geophys. Res.* **101** 195 (1996)
183. Gumerov R I et al. *Radiophys. Quantum Electron.* **42** 463 (1999); *Izv. Vyssh. Ucheb. Zaved. Radiofiz.* **42** 524 (1999)
184. Djuth F T et al. *Phys. Rev. Lett.* **94** 125001 (2005)
185. Gustavsson B et al. *Phys. Rev. Lett.* **97** 195002 (2006)
186. Grach S M et al. *Ann. Geophys.* **25** 689 (2007)
187. Klimenko V V et al., in *Sborhik Dokladov XXIII Vseros. Konf. po Rasprostraneniyu Radiovoln, Ioshkar-Ola, 23–26 Maya 2011 g.* (Proc. of the XXIII All-Russian Conf. on the Propagation of Radiowaves, Yoshkar-Ola, 23–26 May 2011) Vol. 2, p. 239–242
188. Grach S M et al. *Radiophys. Quantum Electron.* **55** 33 (2012); *Izv. Vyssh. Ucheb. Zaved. Radiofiz.* **55** 36 (2012)
189. Sergienko T *Ann. Geophys.* **30** 885 (2012)
190. Kosch M J et al. *Earth, Planets, Space* **66** 159 (2014)
191. Klimenko V V et al. *Radiophys. Quantum Electron.* **60** (3) (2017) in press; *Izv. Vyssh. Ucheb. Zaved. Radiofiz.* **60** (3) (2017) in press
192. Bernhardt P A et al. *J. Geophys. Res.* **105** 657 (2000)

193. Kosch M J et al. *Geophys. Res. Lett.* **27** 2817 (2000)
194. Gurevich A V et al. *Phys. Lett. A* **305** 264 (2002)
195. Rietveld M T et al. *J. Geophys. Res. Space Phys.* **108** 1141 (2003)
196. Grach S M et al. *Adv. Space Res.* **34** 2422 (2004)
197. Krinberg I A *Kinetika Elektronov v Ionosfere i Plazmosfere Zemli* (Kinetics of Electrons in the Ionosphere and Plasmasphere of the Earth) (Moscow: Nauka, 1978)
198. Lobachevsky L et al. *J. Atmos. Terr. Phys.* **54** 75 (1992)
199. Grach S M et al. *Phys. Rev. Lett.* **78** 883 (1997)
200. Boiko G N et al. *Radiophys. Quantum Electron.* **28** 655 (1985); *Izv. Vyssh. Ucheb. Zaved. Radiofiz.* **28** 960 (1985)
201. Kosch M J et al. *Geophys. Res. Lett.* **29** 2112 (2002)
202. Pedersen T et al. *Ann. Geophys.* **29** 47 (2011)
203. Djuth F et al. *J. Geophys. Res.* **99** 333 (1994)
204. Dhillon R S, Robinson T R *Ann. Geophys.* **23** 75 (2005)
205. Mishin E, Pedersen T *Geophys. Res. Lett.* **38** L01105 (2011)
206. Dimant Ya S, in *Vzaimodeistvie Vysokochastonthykh Radiovoln s Ionosferoi* (Interaction of High-Frequency Radiowaves with the Ionosphere) (Exec. Ed. E E Tsedilin) (Moscow: IZMIRAN, 1989) p. 19
207. Vas'kov V V, Dimant Ya S *Geomagn. Aeronom.* **29** 417 (1989)
208. Grach S M, Mityakov N A, Shvarts M M *Geomagn. Aeronom.* **29** 500 (1989)
209. Berezin I V et al. *Geomagn. Aeronom.* **24** 874 (1991)
210. Kim V Yu, in *Entsiklopediya Nizkotemperaturnoi Plazmy. Ser. B. Spravochnye Prilozheniya, Bazy i Banki Dannykh. Ionosfernaya Plazma* Vol. 1–3, Ch. 2 (Ed. V E Fortov) (Moscow: Yanus-K, 2009) p. 425
211. Shindin A V, Sergeev E N, Grach S M *Vestn. Nizhegorodskogo Univ. im. N I Lobachevskogo* (6) 48 (2010)
212. Sergeev E N et al. *Radiophys. Quantum Electron.* **59** (11) (2016) (in press); *Izv. Vyssh. Ucheb. Zaved. Radiofiz.* **59** 977 (2016)
213. Genkin G M, Erukhimov L M *Phys. Rep.* **186** 97 (1990)